CHARLES UNIVERSITY

Faculty of Science

Department of Physical Geography and Geoecology

MATĚJ ROMAN

CORRELATION OF ABIOTIC PROXIES IN HOLOCENE LACUSTRINE SEDIMENTS OF THE PERI-ATLANTIC ARCTIC

KORELACE ABIOTICKÝCH PROXY V HOLOCENNÍCH JEZERNÍCH SEDIMENTECH PERI-ATLANTSKÉ ARKTIDY

Master's thesis

Study programme: Geography

Study branch: Physical geography and geoecology

Supervisor: Assoc. Prof. Mgr. Daniel Nývlt, PhD.

Praha 2017

Statement:

I hereby state that I have completed this thesis by myself and that I have properly cited all literature and other information sources I have used. Neither this thesis nor its parts have been submitted to achieve any other academic title(s).

Prohlášení:

Prohlašuji, že jsem závěrečnou práci zpracoval samostatně a že jsem uvedl všechny použité informační zdroje a literaturu. Tato práce ani její podstatná část nebyla předložena k získání jiného nebo stejného akademického titulu.

In Prague, 12th August 2017
V Praze, dne 12. srpna 2017

Matěj Roman

Matěj Roman

Zadání diplomové práce

Název práce

Korelace abiotických proxy v holocenních jezerních sedimentech peri-Atlantské Arktidy

Cíle práce

Diplomová práce naváže na bakalářskou práci studenta a bude založena na korelaci vybraných abiotických proxy parametrů v holocenních jezerních sedimentech západního Grónska, centrálního Svalbardu a severovýchodního Norska, na interpretaci klimatických a environmentálních změn a zjištění klíčových řídících faktorů ovlivňujících tyto změny v různých částech peri-Atlantské Arktidy.

Použité pracovní metody, zájmové území, datové zdroje

Metodická část práce bude vycházet z detailního popisu litologie (facie a zrnitost) ve vztahu k vybraným abiotickým proxy, jako jsou magnetické parametry (magnetická susceptibilita i frekvenčně závislá magnetická susceptibilita), prvkové složení (rentgen-fluorescenční stanovení vybraných prvků), podíly organického a anorganického uhlíku a síry. Časový vývoj sedimentace bude založen na modelování časově-hloubkového vývoje s použitím stáří založeném na radioizotopech uhlíku, olova a cesia. Vybrané parametry budou korelovány vhodnými statistickými metodami včetně stanovení klíčových řídících faktorů ovlivňujících zjištěné změny v jezerních záznamech. K dispozici k tomuto studiu jsou jádra jezerních sedimentů z následujících jezer: jezera nad zálivem Kobbefjorden při západním pobřeží Grónska, jezero Garmaksla nad zálivem Billefjorden v centrálním Svalbardu a jezera v povodí řeky Pasvik v severovýchodním Norsku na poloostrově Kola, které byly odvrtány studentem a školitelem v letech 2013 a 2014.

Datum zadání: 11. 12. 2014

Jméno studenta: Matěj Roman
Podpis studenta: Matěj Roman

Jméno vedoucího práce: Mgr. Daniel Nývlt, PhD.
Podpis vedoucího práce: Daniel Nývlt

Acknowledgements:

My greatest and foremost thanks go to Daniel Nývlt, who incited my interest in geosciences and gave me almost limitless amount of career and research opportunities to pursue my dreams (especially in very cold regions). This thesis would look quite different but for him.

Neither could this thesis be written without help of many people in the field and in the lab. I acknowledge the support of everyone from the Centre of Polar Ecology, especially Prof. Josef Elster, for getting me to Petuniabukta and (unfortunately) back again, twice. Namely I have to mention great leaders of our hydro-limno group, Katka Kopalová, Jeník Kavan, and also Saša Bernardová. This work is but a small instalment to a large undertaking – enormous amount of work was already done by Eveline Pinseel, Bára Chattová and Dan Vondrák. Since so many people participated in the retrieval of sedimentary cores, I have to acknowledge their help in the field: Jakub Žárský, Lucie Krajcarová, Eliška Bohdalková, Petr Holík and Kuba Ondruch (from the 1st field trip), and Lenka Ondráčková, Eva Hejduková, Michal Růžek, Petra Polická and Martin Lulák (the 2nd campaign).

My sincere gratitude belongs to Paul Eric Aspholm for help with coring in northern Norway, invaluable local knowledge and warm reception at Svanhovd station. Jiří Lehejček and Martin Lexa were a great company and help during the whole field trip.

I would like to acknowledge Dr. Hana Grison, Assoc. Prof. Jaroslav Kadlec and Assoc. Prof. Lenka Lisá for their advice and help with lab measurements, Václav Tejnecký and his colleagues for geochemical manalysest on cores from Greenland, and Viktor Goliáš for short-lived radionuclide dating. I appreciate useful advice and comments I received from Anna Píšková, Linda Nedbalová and Zbyněk Engel. I thank everyone from the Department of Physical Geography and Geoecology and Department of Ecology of the Charles University for teaching me so much. Although the focus of our endeavour was nearer the other pole, I benefited enormously from working with Dr. Juan Manuel Lirio and Silvia H. Coria (from IAA), and Prof. David C.W. Sanderson (SUERC), for which I am genuinely grateful.

At last, I want to thank my schoolmates from GeKa, my family and, most importantly, Verča.

This work has been financially supported by GA UK (project No. 126715), INTERACT Transnational Access Project CLAHALSAR I and II funded by the European Union Seventh Framework Programme (grant agreement No. 262693). Participation on the field campaigns to James Ross Island and internship at SUERC was made possible by the generous travel scholarships of the 'Nadace Nadání Josefa, Marie a Zdeňky Hlávkových' Foundation and the Charles University Mobility Fund.

Abstract:

The peri-Atlantic Arctic, one of the most sensitive components of the Earth climate system, experienced pronounced climatic fluctuations during the Holocene. Several external forcings were considered responsible for these variations, including decline of insolation on the Northern Hemisphere, changes in distribution of land ice mass, explosive volcanism, or changes in atmospheric and oceanic circulation. In order to explore the driving mechanisms of the peri-Atlantic Arctic environmental variability, three sites located in different parts of the region were selected for palaeoenvironmental reconstructions with focus on extracting the climatic information. With this intention, sedimentary cores from i) Lake Garmaksla, Central Svalbard, ii) Jarfjorden, northeastern Norway, and iii) Kobbefjord area, southwestern Greenland, were retrieved and subjected to multi-proxy investigation. The absolute chronostratigraphic framework was established by comprehensive radiocarbon (^{14}C) and short-lived radioisotopes (^{210}Pb, ^{137}Cs) dating. Further analyses include measurements of magnetic susceptibility, grain size distribution, element composition by means of X-ray fluorescence (XRF), and elements bound to organic matter, i.e. organic carbon, nitrogen, sulphur and biogenic silica. The relationships between the acquired proxy data were investigated within individual sedimentary cores, between the cores from the same region, and finally, with other available reconstructions from the region of interest. Furthermore, stratigraphic sequences were correlated in order to improve precision of the age-depth models. Exploratory statistics and factor analysis were applied to extract relevant palaeoenvironmental information.

The presented palaeoreconstructions cover the Middle and Late Holocene in case of Garmaksla Lake and Jarfjorden records. These sequences were found to contain valuable information on the climatic development of the Neoglacial period. Garmaksla Lake sensitively reacted especially to variations in sea ice extent and continentality. In case of Jarfjorden lakes, the sedimentary records reveal episodes of increased erosion and reduction of vegetation cover, induced by either natural or anthropogenic influence, and evidence of pollution in the last 70 years. Infilled lakes from southwestern Greenland document the lake ontogeny and transition to peat bog that was nonetheless modulated by climate, especially shifts of the North Atlantic Oscillation in the past ~800 years. The synthesis of palaeoreconstructions from the entire peri-Atlantic Arctic pinpoints the importance of understanding the interconnected factors of climatic variability on the Holocene time scale, since it provides clues on the future climate development of the region.

Key words: palaeolimnology, Holocene, Arctic, proxy data, lake sediments

Abstrakt:

Peri-Atlantská Arktida je jednou z nejcitlivějších součástí klimatického systému Země a zaznamenala významné klimatické výkyvy během holocénu. Tyto fluktuace byly vysvětlovány řadou vnějších vlivů, včetně poklesu insolace na severní polokouli, změn v rozložení pevninských ledovců, vulkanismu či změn atmosférické a oceánické cirkulace. Pro lepší pochopení řídících mechanismů, které ovlivňují přírodní variabilitu v peri-Atlantské Arktidě, tři navzájem vzdálené lokality byly vybrány k paleoenvironmentální studii se zřetelem na získání klimatické informace. Za tímto účelem byla odvrtána tři sedimentární jádra z lokalit i) jezero Garmaksla, v centrálním Svalbardu, ii) záliv Jarfjordem, severovýchodní Norsko, iii) oblast Kobbefjord, jihovýchodní Grónsko. Tyto sedimentární sekvence byly podrobeny vybraným abiotickým analýzám. Absolutní chronostratigrafie byla určena pomocí datování ^{14}C a izotopy s krátkým poločasem rozpadu ^{210}Pb a ^{137}Cs. Další analýzy zahrnovaly měření magnetické susceptibility, zrnitostního složení, prvkového složení pomocí rentgen-fluorescenční spektrometrie a organogenních prvků uhlíku, dusíku, síry a biogenního křemíku. Vztahy mezi jednotlivými proxy v rámci jednoho jádra, v rámci zájmové oblasti a konečně s ostatními rekonstrukcemi v regionu byly zjištěny pomocí explorační statistiky a faktorové analýzy. Stratigrafické sekvence byly také navzájem korelovány za účelem zpřesnění časově-hloubkových modelů a získání užitečné paleoenvironmentální informace.

Předkládané rekonstrukce v případě jezera Garmaksla a jezer z oblasti Jarfjord časově pokrývají střední a pozdní holocén. Tyto jezerní archivy obsahují záznam o klimatickém vývoji během neoglaciálu. Jezero Garmaksla citlivě reagovalo zejména na změny v rozsahu mořského zámrzu a kontinentality. Jarfjordská jezera zachycují období zvýšené eroze a úbytku vegetačního krytu, vyvolaná přírodními výkyvy nebo lidskými zásahy; posledních 70 let byla postižena znečištěním. Zazemněná jezera z oblasti Kobbefjord v jihozápadním Grónsku dokumentují postupný vývoj jezerního ekosystému a přechod v rašeliniště, jež ale bylo ovlivňováno klimatickými výkyvy, zejména Severoatlantskou oscilací, v posledních 800 letech. Syntéza paleorekonstrukcí z celé peri-Atlantské Aktidy naznačuje, že pro pochopení zákonitostí řídících klimatickou variabilitu současnou i budoucí je nutné pochopit holocenní vývoj těchto změn.

Klíčová slova: paleolimnologie, holocén, Arktida, proxy data, jezerní sedimenty

Table of contents

I. Introduction

The North Atlantic Ocean and adjacent peri-Atlantic Arctic are considered to be the key regions of the Earth climate system for its influence and feedbacks have played a paramount role in the past and current climate changes (Kaufmann et al. 2009, Miller et al. 2010a). Several important mechanisms of the Earth system such as Arctic Amplification (AA), Atlantic Meridional Overturning Circulation (AMOC) or North Atlantic Oscillation (NAO) are taking place here (Lowe and Walker 2014, Bradley 2015). This region experienced marked environmental changes during the Quaternary and often sudden switches of oceanic and atmospheric circulation as well as extent of glaciation (Broecker and Denton 1990, Miller et al. 2010, White et al. 2010). These mechanisms have on the millennial time-scales significantly modulated or even governed the glacial–interglacial cycles, primarily paced by orbital forcing (Ruddiman and McIntyre 1981, Heinrich 1988, Bond et al. 1993, Alley 1998, Clark et al. 2002, Hald et al. 2007). Similarly, attention must be paid to more contemporary consequences of how these systems operate in rapidly warming world and the polar regions in particular, as the abrupt reorganizations of climate systems can bear serious implication for the human society and natural ecosystems (Alley 2003, IPCC 2013, Hansen et al. 2016). However, successful modelling and predicting the future behaviour of atmospheric and oceanic circulation, sea-level rise or continental ice sheets requires detailed, chronologically well constrained evidence of their state in the past.

I.1 Aims of this thesis

Available lacustrine sedimentary records originating from this area will be subjected to multi-proxy analysis in order to elucidate a palaeoenvironmental signal, documenting a common influence of the North Atlantic climate on the lake catchments, lake bodies and respective ecosystems. This will be fulfilled by assessing the mechanisms that control the response of individual proxies in each region and lake, and further by establishing the stratigraphical framework of these proxy records, enabling comparison with other documented palaeoreconstructions.

II. Literature review: Physical and geochemical proxy data in lacustrine sediments and their application in palaeoenvironmental reconstructions

Lakes represent an excellent environment for preservation of information on past conditions both in the lake and the surrounding (Cohen 2003). However, we can only read these natural archives, if we master the language. If we elaborate on this analogue of comparison lakes to books, then lacustrine sediments represent a fragmentary book collection with many pages missing, written in incomprehensible language, and dealing with a single theme viewed at from different angles (Barker 2009). In more scientific terms, we can access these natural archives by applying various physical, geochemical and biological analyses, although most often are these methods synthesized to provide an integrated multi-proxy insight into the past environmental changes. Importantly, proxy data do not (by definition) directly record environmental variables of interest, such as mean temperatures or precipitation, they can, however, provide a fairly accurate estimate of former environments relative to the present day, thus allowing inference of past climatic, hydrologic or other conditions (Lowe and Walker 2014). A brief introduction to proxy data used in this thesis follows. Firstly, however, basic principles and development of radiometric dating, techniques used for establishing absolute chronology, are presented.

II.1 Radiometric dating

Natural radioactivity of certain unstable elements forms the basis for radiometric dating (Lowe and Walker 2014). Transformation from parent to daughter nuclides, involving atomic reorganization and energy emission in form of particle or electromagnetic radiation, is time-dependant and this is the basic premise. With decay constant (or half-life) known, we can measure the present content of given radionuclides in a sample (e.g. by accelerator mass spectrometry; AMS) and then compute the amount of time elapsed since a certain event, when the radiometric ‘clock’, i.e. decay of radioisotopes, presumably began (Walker 2005). In general, that means a time of initial isotopic state before the parent radioactive nuclides began to transform into daughter products (Hall 2009); more specifically, it may represent formation of rock or mineral, or fixation of atmospheric radiogenic carbon into biomass.

II.1.1 Radiocarbon dating.

Since the pioneering work of Willard Libby et al. (1949), radiocarbon dating has been the most employed method of age determination in Quaternary science and revolutionized also the fields of archaeology, anthropology or oceanography (Walker 2005). Radiocarbon, or ^{14}C, is a naturally occurring isotope of carbon, although extremely rare (forms only about 1 atom in 10^{10} of all carbon isotopes), that belongs to cosmogenic nuclides. Upon entering the Earth's atmosphere, bombarding neutrons of cosmic rays interact with atmospheric ^{14}N, producing radioactive ^{14}C incorporated into $^{14}CO_2$ (Walker 2005, Bradley 2015). Owing to weaker geomagnetic field, ^{14}C production is enhanced in higher latitudes, although global atmospheric circulation quickly redistributes ^{14}C all around the globe (Wolfe et al. 2004). Radiocarbon is thereafter assimilated in organic tissues by photosynthesis and respiration, maintaining isotopic equilibrium until an organism dies. No replacement of decaying ^{14}C is supplied afterwards, signifying that radiometric clocks were set (Lowe and Walker 2014).

The half-life of ^{14}C is determined as 5,730 ± 40 years (i.e. more accurate 'Cambridge' half-life recalculated from the original Libby's half-life of 5,568 ± 30 years; Godwin 1962 in Walker 2005), in other words, ^{14}C content is halved every 5,730 years (Fig. 2.1). The negative exponential decrease of ^{14}C content sets the theoretical upper limit of detection at ten half-lives (which translates into 57,300 years), for afterwards ^{14}C concentration in a sample is so low it cannot be reliably measured (Bradley 2015). Applicable range of radiocarbon dating thus lies in the last ~50 ka, i.e. the Holocene and the Late Pleistocene until mid MIS 3. The younger (more present) limit of ^{14}C dating is affected by anthropogenic changes of ^{14}C reservoir in the atmosphere, i.e. firstly, emitting old ^{14}C-depleted carbon by

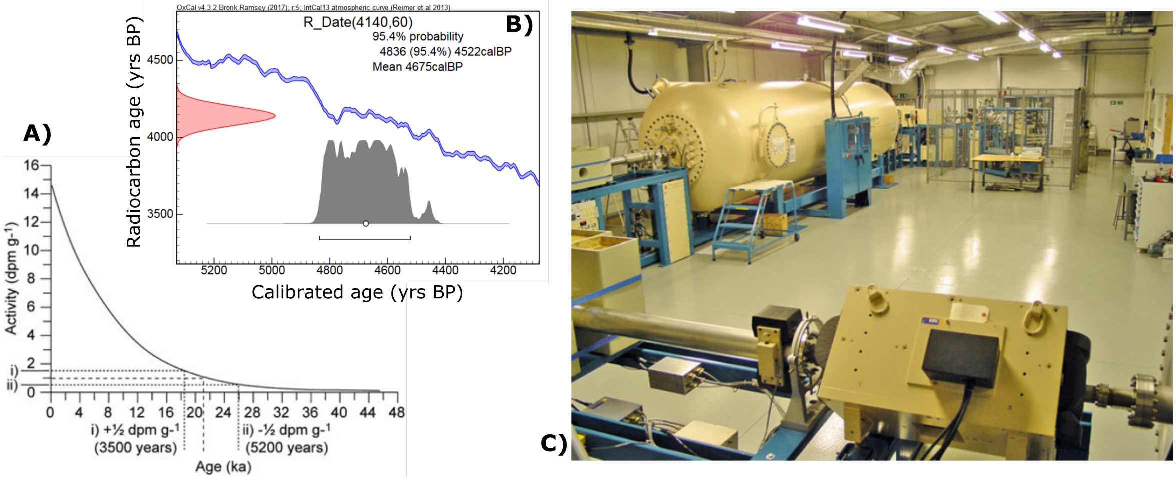

Figure 2.1 A) Radiocarbon decay curve, relating activity of ^{14}C (disintegrations per minute per gram) to sample age; the activity is halved every 5,730 yrs (from Lowe and Walker 2014). B) Example of calibration of ^{14}C age to calendar/tropical age based on calibration curve IntCal13 (Reimer et al. 2013) in OxCal 4.2 software (Bronk Ramsay 2009). C) Accelerator Mass Spectrometer facilities in the Scottish Universities Environmental Research Centre, East Kilbride, UK (from Lowe and Walker 2014, photo by Sheng Xu).

burning fossil fuels (Suess effect; Bradley 2015), and later by injecting large amounts of radioactive ^{14}C during thermonuclear explosions in the second half of the 20th century. ^{14}C concentration varied also naturally (de Vries 1958), as a result of secular variations in the shielding effect of the Sun and geomagnetic field, or through release and capture of old carbon in deep marine reservoirs (Bradley 2015). Since the fundamental premise of constant atmospheric ^{14}C concentration is thus hampered, to obtain true 'calendar' age it is necessary to calibrate radiocarbon dates against another independent dating methods (Lowe and Walker 2014). Radiocarbon curves, covering the last 50 ka and based on dendrochronology, speleothem and corals dating, or annual varves counting (Reimer et al. 2013), are thus used to convert ^{14}C ages into 'calendar' ages.

Dating can be performed on carbon found in various materials: organic macrofossils in lake and marine sediments, wood, peat, charcoal, bones, pigments etc. As organic material is rather scarce in Arctic lacustrine sediments, introduction of AMS instead of conventional measurement greatly facilitated the dating, for smaller amount of dated material (<1 mg) is necessary (Wolfe et al. 2004). It enables to avoid dating bulk samples, which are inherently prone to errors, and to replicate dating of even minute samples. In absence of any micro- or macrofossils, chemically extracted humic acids provide a preferable option over bulk samples (Abbott and Stafford 1996), although certain problems emanate from remobilisation and fluid percolation. In Arctic lake basins underlain by crystalline bedrock, $^{14}C/^{12}C$ isotopic ratio is not influenced by old, ^{14}C-depleted carbon leached from bedrock, so that dating of macrofossils of autochthonous aquatic organisms is viable (Wolfe et al. 2004). Owing to imperfect gas exchange between the atmosphere and lake, however, the reservoir effect, or a delayed response of $^{14}CO_2$ uptake into water, must be considered (Cohen 2003). Another obstruction is posed by incomplete mixing of water column in amictic (e.g. permanently frozen) and meromictic (with saline bottom layer) lakes, again leading to an erroneous initial isotopic ratio in assimilating aquatic organisms. If the lake basin or catchment is formed by carbonate rocks, further problems of hard-water effect (leaching of ^{14}C-depleted carbon) arise, causing increase in apparent age over the real age by the order of 10^2–10^3 years (Wolfe et al. 2004). In all these very common cases, dating of terrestrial organism macrofossils and pollen grains is highly recommended (e.g. Wyatt Oswald et al. 2005, Lohne et al. 2013, van der Bilt et al. 2015).

II.1.2 Short-lived radioisotope dating

Sediments younger than ~150 years can be dated by measurement of specific activity of short-lived radioisotopes of lead ^{210}Pb ($t_{1/2}$ = 22.2 years) and caesium ^{137}Cs ($t_{1/2}$ = 30.1 years; Appleby 2008). Lead is a part of ^{238}U decay chain and is produced from its parent radionuclides ^{226}Ra and ^{222}Rn. Gaseous radon evades from the ground into the atmosphere, where it quickly decays into ^{210}Pb (Fig. 2.2; Swarzenski 2015). Lead is removed from the atmosphere by wet or dry deposition after mean residence time of ~10 days and is carried into lakes, where it easily adsorbs to suspended particles and is incorporated into sediment (Szwarenski 2015). This type of lead is termed unsupported and in ideal case of constant sedimentation rate its concentration should exponentially decline with depth (Appleby 2008). However, the other type of lead, supported ^{210}Pb, is found in rocks or sediments, being in a radioactive equilibrium with its decay chain radionuclides, and its concentration remains stable throughout the profile (Walker 2005). Supported ^{210}Pb may be determined by estimation from its parent radioisotope ^{226}Ra activity. By detracting the supported ^{210}Pb from total ^{210}Pb content, exponential curve of excess ^{210}Pb can be used for dating (Szwarenski 2015).

This approach requires fulfilment of several assumptions, such as immobility of deposited lead, absence of post-depositional sediment reworking or stable sedimentation rates (Wolfe et al. 2004, Lowe and Walker 2014). As especially the last condition is seldom satisfied, instead of constant initial concentration of unsupported ^{210}Pb, constant rate of supply (CRS) model was developed to allow for changes in accumulation rate (Appleby and Oldfield 1978). The CRS model assumes constant ^{210}Pb fallout over the course of the interval studied, i.e. the last two centuries (Walker 2005). Spatial variations in ^{210}Pb fallout constitute a greater challenge in dating Arctic lake sediments, as permafrost impedes ^{222}Rn release into the atmosphere (Wolfe et al. 2004). Together with prolonged, often perennial, ice cover

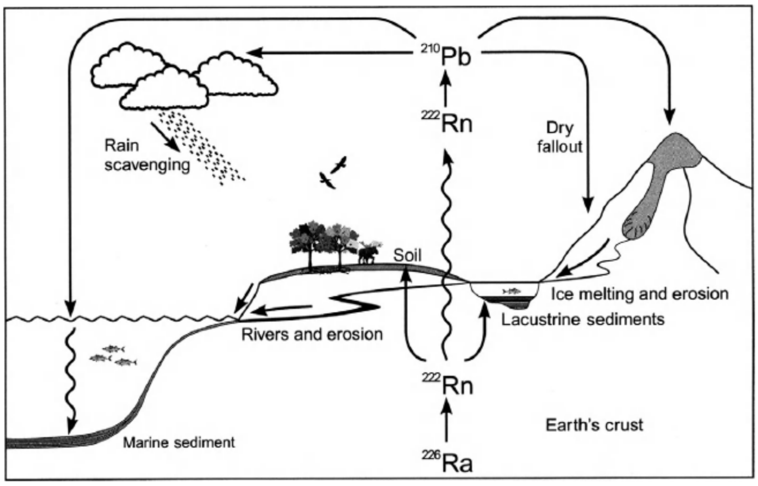

Figure 2.2 Conceptual model of ^{210}Pb global cycle. Following the evasion of gaseous radon from the ground, newly formed lead is quickly drawn down to the surface by wet and dry deposition, leading to incorporation of ^{210}Pb in the lake sediments. After Preiss et al. 1996 in Bradley 2015.

duration, preventing transfer of ^{210}Pb into sediments, this leads to low or even undetectable lead concentrations, complicating the accurate dating (Wolfe et al. 2004).

Radioisotope caesium ^{137}Cs forms in thermonuclear reactions and was introduced into the atmosphere in detectable quantities by nuclear bomb testing since early 1950s (Lowe and Walker 2014). Most lacustrine records show a distinct peak of ^{137}Cs that corresponds to a maximum of nuclear bomb testing before it was banned in AD 1963. In addition, many Northern Hemisphere sites, including the Arctic, display a secondary peak of Chernobyl nuclear accident in AD 1986 (Appleby 2008). Both these fallout radioisotopes, ^{210}Pb and ^{137}Cs, can be appropriately combined with other anthropogenic radionuclides, such as $^{239+240}$Pu and ^{241}Am, to achieve a more robust chronostratigraphy of the most recent sedimentary records (Walker 2005).

II.2 Magnetic susceptibility

Magnetic susceptibility is a physical parameter that represents how easily a material becomes magnetised (Thompson and Oldfield 1986). All substances exhibit some magnetic behaviour, because it is the nature of matter (Evans and Heller 2003). The motion of charged particles inside of an atom gives rise to magnetic field (H). Response of a material to a magnetic field of certain intensity that passes through it is denoted as magnetization (M; Maher and Thompson 1999). Volume magnetic susceptibility (κ) then relates all three parameters in an equation $\kappa = M/H$ (Evans and Heller 2003), which means κ is the ratio of induced magnetization to intensity of inducing magnetic field. κ is dimensionless, because both H and M are measured in ampere metres^{-1} ($A\cdot m^{-1}$). To obtain specific, or mass, magnetic susceptibility (χ), it is necessary to divide κ by density. Therefore, χ has units reciprocal to density ($m^3\cdot kg^{-1}$; Thompson and Oldfield 1986). Magnetic susceptibility can be illustratively used for classification of magnetically different types of materials, as will be shown further.

Diamagnetism occurs in all materials and results from sideways Lorentz force (torque) of electrons orbiting the nucleus under applied magnetic field (Evans and Heller 2003). The forces, however, cause the orbit to precess, which generates a magnetic moment in the opposite direction to the applied H (Thompson and Oldfield 1986). Diamagnetic materials therefore attain negative, although very low, χ values on the order of -10^{-8} $m^3\cdot kg^{-1}$ (Lanza and Meloni 2006). Numerous widespread minerals, including calcite, quartz or K-feldspar, and importantly also water, display diamagnetic behaviour (Thompson and Oldfield 1986).

Paramagnetism is induced by electrons spinning around their own axis, generating thus spin magnetic moment (Evans and Heller 2003). If these magnetic moments are oriented in such a way they do not cancel each other, such as in e.g. sodium, permanent magnetic moment is produced. Paramagnetic minerals comprise olivine, pyroxenes, biotite or clay minerals, and their χ values range on the order of 10^{-7}–10^{-6} $m^3 \cdot kg^{-1}$ (Lanza and Meloni 2006). Despite importance of paramagnetic minerals in environmental research, their quite low χ values often produce noise rather than signal (Evans and Heller 2003).

Ferromagnetic materials contain unfilled electron subshells with uneven number of electrons displaying oppositely oriented magnetic moments (Evans and Heller 2003). For example, each atom of iron possesses a net magnetic moment of 4 Bohr magnetons thanks to the electrons ratio of antiparallel directions 5:1. Tight crystal lattice then induces interactions between electron orbitals of individual atoms, causing thus alignment of magnetic moments that produces strong permanent magnetization. Intensity of magnetic moment, however, decreases with higher temperature until it is lost at Curie point, where the orbitals cease to overlap (Thompson and Oldfield 1986). Ferromagnetism is observed in elements iron, cobalt and nickel and their alloys (Sandgren and Snowball 2001). Various Fe oxides, hydroxides and sulphides exhibit specific subtypes of ferromagnetic behaviour, i.e. ferrimagnetism as in magnetite, maghaemite or pyrrhotite, and antiferrimagnetism in goethite or haematite (Thompson and Oldfield 1986). Of these magnetite (Fe_3O_4) is the strongest naturally occurring magnetic mineral, with χ reaching $5–7 \cdot 10^{-4}$ $m^3 \cdot kg^{-1}$ (Lanza and Meloni 2006). In ferrimagnetic materials, two types of magnetic moments of different magnitudes are arranged in antiparallel directions, producing net magnetization lower than ferromagnets. Antiferrimagnetism occurs if these oppositely directed magnetic moments have approximately equal magnetic moments (Thompson and Oldfield 1986).

Measurements of magnetic parameters in lacustrine sediments can reveal multiple physical and sedimentological properties of the constituent material. Magnetic susceptibility of the sediment reflects not only mineralogy, but concentration and grain size and shape of the minerals bearing magnetic signal as well (Cohen 2003). Since the pioneering study of Lough Neagh sediments in Northern Ireland by Thompson et al. (1975), magnetic susceptibility signal is believed to reflect mainly allochthonous input of detrital (minerogenic) material from the lake catchment, in the form of para-, ferro- or ferrimagnetic minerals. Basic environmental inference was drawn that increased erosion or hydrological activity in the catchment cause enhanced influx of magnetic grains into lake sediments

(Dearing 1999a). However, additional important sources of magnetic minerals must be considered.

Aeolian processes and atmospheric deposition of pollution particles and tephra complements the fluvial transport (Dearing 1999a). Magnetic signal derived from aeolian transport is evident e.g. in loess/palaeosol sequences of the Chinese Loess Plateau (An et al. 1991) or Holocene sediments of Lake Yoa in Chad (Francus et al. 2013). Areas downwind of industrialised and densely populated areas are prone to pollution by coal-fired fly-ash and heavy metal particles (also called magnetic spherules) that are detectable by elevated χ values of topsoils, vegetation and also sediments (Petrovský and Ellwood 1999; Oldfield et al. 2003). Authigenic sources of magnetic minerals within lakes include magnetotactic bacteria, which intracellularly produce magnetite functioning as their internal compass used for navigation (Paasche et al. 2004), and also diagenetic formation of iron sulphides, such as ferrimagnetic pyrrhotite and paramagnetic pyrite, generally produced in sediments of saline or anoxic waters (Thompson and Oldfield 1986). On the other hand, magnetic minerals may dissolute by post-depositional reductive diagenesis, occurring particularly in eutrophicated waters with anaerobic surficial sediments, which then confounds correlations with other proxies or with sediment cores from the same lake (Dearing 1999a). Autochthonous organic matter growing in the lakes exhibits diamagnetic behaviour and contributes thus to concealing magnetic signal.

Grain size of magnetic minerals effects χ substantially. So far only low-frequency magnetic susceptibility (henceforth denoted as χ_{lf}) was considered, typically measured in the range $0.4–1 \cdot 10^3$ Hz (e.g. Bartington MS2 system $f = 460$ Hz, Kappabridge MFK1-A at $f = 976$ Hz; Dearing 1999b). This parameter, however, cannot distinguish between ferrimagnetic grain sizes or mineral types (Dearing et al. 1996). Implementation of another measurement at higher frequency (χ_{hf}), on the order of tenfold increase over χ_{lf}, allows computation of frequency dependent magnetic susceptibility ($\chi_{fd} = 100 \cdot (\chi_{lf} – \chi_{hf}) / \chi_{lf}$). χ_{fd} enables detection of ultrafine (diameters <0.3 μm) ferro- and ferrimagnetic minerals exhibiting superparamagnetic (SP) behaviour (Dearing 1996, Sandgren and Snowball 2001). SP grains are presumably products of weathering, pedogenesis and metabolism of magnetosomes (Dearing 1999b).

Thanks to the plentiful environmental information sedimentary magnetism carries, as well as rapidity of measurement, and in spite of certain caveats, magnetic susceptibility represents an accessible and valuable proxy that finds its use in intrabasinal or regional correlations of sedimentary cores, in identification of detrital minerogenic input or pollution, and to support other proxy data (Cohen 2003).

II.3 Grain size distribution

Texture describes geometric aspects and relationships between the component particles of rock or sediment, and together with structure and composition represent the fundamental attributes of sedimentary deposit (Last 2001). Texture can be also defined as the microgeometry of sediment, dealing with individual grain characteristics, and these primary textural attributes include size, shape and fabric (or arrangement). Importance of texture resides above all in description and classification of sediment, but careful study of textural characteristics also helps to unravel: i) provenance and mechanisms of transport of the material, ii) past limnological conditions in the depositional basin, and finally iii) palaeoclimatic and palaeohydrological context (Last 2001). This subchapter will focus on grain size for its fundamental function in hydraulics, geomorphology and lake sedimentology (Håkanson and Janson 1983) as well as diagnostic significance for Quaternary stratigraphy (Lowe and Walker 2014).

Owing to irregularity of naturally occurring grains the concept of size alone becomes unambiguous, leading to institution of various measures of particle size (Last 2001). These miscellaneous definitions, including maximum calliper diameter, sieve diameter or equivalent spherical diameter, emanate largely from different techniques of grain size determination (Blott and Pye 2001). Direct calliper measurement and wet and dry sieving thus in practise express volumetric grain size, whereas settling rate methods depend on mass or density of particles (Last 2001). Different techniques are also suited for different grain sizes; sieving, for example, is impractical below the limit of 63 µm, while analytical size range of Coulter counter and laser diffractometer extends beyond fine clay fraction (<0.5 µm), although does not include gravel fraction. Consideration should be also given to practical details of grain size analysis, such as time duration and quantity of sample required for measurement. Sedimentation rate methods, although considered the most exact, thus demand more analytical time (Håkanson and Janson 1983). To conclude, despite a large array of available methods determination of the real grain size remains problematical, as modern analytical devices are often precise (i.e. providing consistent results), but at the same time inaccurate (measured value does not equal the true grain size; Last 2001).

Sedimentological grain size is traditionally considered in terms of statistical distribution (Last 2001). Broad range of grain sizes found (not only) in lake sediments presupposes the use of logarithmic or geometric scale in order to ascertain equal emphasis to be placed on finer part of the spectrum (Blott and Pye 2001). The most popular logarithmic Udden-Wentworth grade scale uses the size classes differing by a factor of two, and can be presented either in metric units, or logarithmically transformed into dimensionless units of ϕ (Krumbein 1934 in Last 2001). Standard statistical measures such as mean, median, mode, but also sorting, skewness or kurtosis, then can be applied to measured grain size distribution (Folk and Ward 1953). Basic textural classification defines sand, silt and clay as the most frequent constituents of lacustrine sediments (Last 2001). Sand fraction is composed by grains with diameters 2–0.063 mm. The boundary between silt and clay fractions is usually given as 2 μm (Friedman and Sanders 1978, Blott and Pye 2001), although classical sedimentological literature prefers the limit of 4 μm (Last 2001). Natural sediment is usually composed of various proportion of these three fractions, which can be illustratively visualised in the Shephard’s ternary diagram and classified as silty clay, sandy silt etc. (Håkanson and Janson 1983).

Environmental controls on particle size in lake sediments of the Arctic have been investigated by a number of experimental and sedimentological studies (Cockburn 2008, Lapointe 2012). Grain size distribution should primarily reflect the energy of depositional environment, although provenance can also play the role in large lake catchments (Mather 2011). Increased concentration of coarse fraction was nevertheless found to mirror short-lived inflow events, characterised by high discharges and suspended sediment yield (Cockburn and Lamoureux 2008). Besides entrainment and sedimentation processes, grain size further affects capacity of the material to bind pollutants and easily adsorptive particles thanks to the inverse relationship with specific surface of grains (i.e. smaller particle size means greater surface area; Håkanson and Janson 1983). Grain size variations may also result from lake level changes, coarser fraction being typical for more proximal parts of lake basins, while only fine fraction reaches the central and distal zones (Aebly and Fritz 2009, Francus et al. 2013). Furthermore, grain-size variability often displays clear affinities to climate oscillations, either at Quaternary or Holocene time scales (Lapointe et al. 2012, Francke et al. 2013, Francus et al. 2013). Grain size record of the past 2.6 Ma from Lake El’gygytgyn, Far East Russian Arctic, indicates coarser material was deposited during interglacials due to more intensive wind-driven current redistribution in longer ice-free periods and greater sediment supply from melting active layer (Francke et al. 2013). Similarly, high-energy facies in the Late Holocene varved sediments from Melville Island, the Canadian Arctic, form during intensive summer rainfall events and suggest an

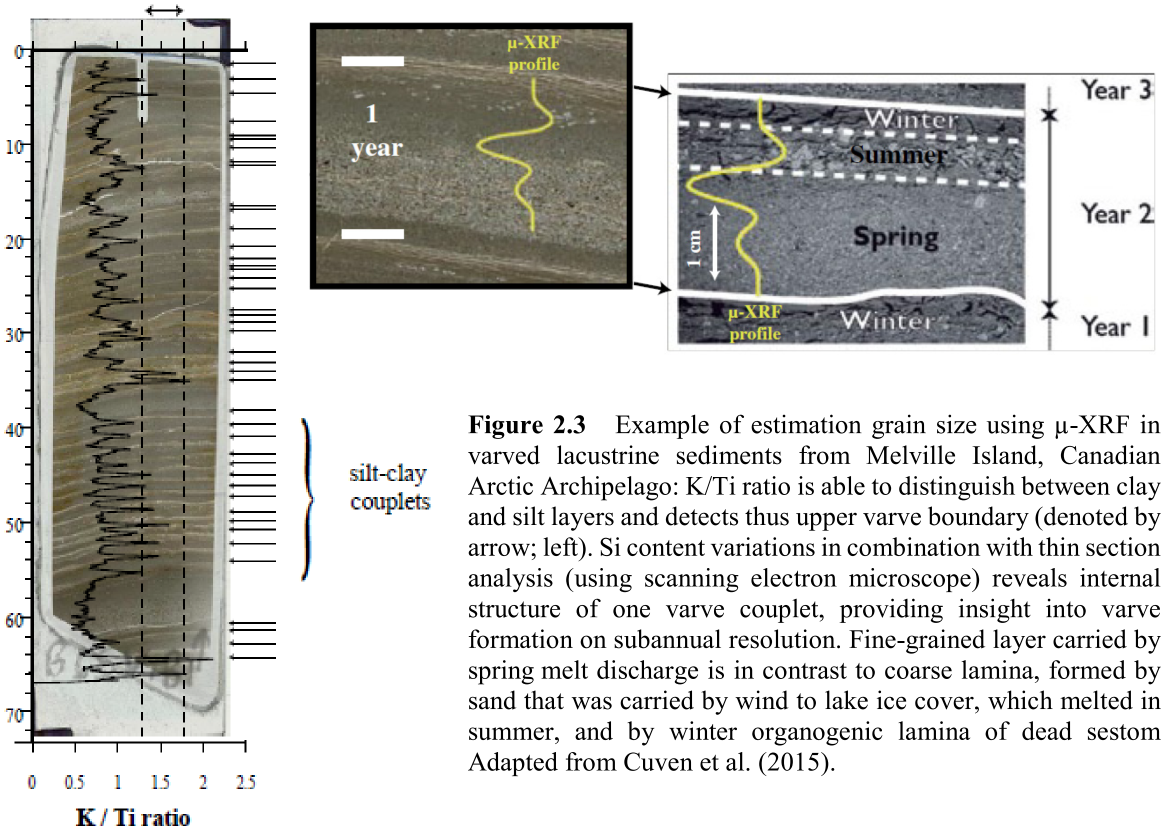

Figure 2.3 Example of estimation grain size using μ-XRF in varved lacustrine sediments from Melville Island, Canadian Arctic Archipelago: K/Ti ratio is able to distinguish between clay and silt layers and detects thus upper varve boundary (denoted by arrow; left). Si content variations in combination with thin section analysis (using scanning electron microscope) reveals internal structure of one varve couplet, providing insight into varve formation on subannual resolution. Fine-grained layer carried by spring melt discharge is in contrast to coarse lamina, formed by sand that was carried by wind to lake ice cover, which melted in summer, and by winter organogenic lamina of dead sestom Adapted from Cuven et al. (2015).

unprecedented increase in rainfall amount during the 20th century accompanying rapid warming (Lapointe et al. 2012). Other detailed studies revealed a relationship of grain size and varves formation, as both parameters exhibit a strong annual signal resulting from influx of clastic material during the spring snow melt and lake ice break-up (Fig. 2.3; Lamoureux 2004, Cuven 2011). Grain size parameters may also reveal (post-)depositional disturbances such as seismites and turbidites induced by earthquakes or storms and that often disrupt constructed age-depth models (Van Daele et al. 2014).

II.4 Geochemical composition

Organic and inorganic geochemical techniques, elemental determination in particular, have been successfully used in palaeolimnology mainly as a supporting tool to biological and other analyses (Boyle 2001), although recent development of high-resolution scanning approaches has unlocked the full potential of geochemical archives in lacustrine sediments (Davies et al. 2015). Determination of elemental composition helps characterizing detrital material (its mineralogy, provenance and alteration) as well as content and properties of organic matter. Two techniques of geochemical palaeolimnology applied in this thesis, X-ray fluorescence and organic geochemistry, followed by a summary of environmental inferences drawn from geochemical records, are presented below.

II.4.1 X-ray fluorescence spectrometry

Non-destructive analysis using X-ray fluorescence (XRF) spectrometry allows relatively fast and straightforward determination of elemental composition of the sediment (Rothwell and Croudace 2015). The analysis usually detects elements in the range from Al (proton number $Z = 13$) to U ($Z = 92$), in concentrations as small as several ppm under favourable conditions (Boyle 2001). The principle of XRF analysis is based on natural secondary fluorescence of the material after having been excited by X-rays (Rothwell and Croudace 2015). During this process, electrons are expelled from the inner atomic shells by incident X-ray radiation and are replaced by electrons from the outer shells. The energy difference is conserved by emission of electromagnetic radiation of certain wavelength that is characteristic for each element, and that is being detected (Rothwell and Croudace 2015).

Detection limits, accuracy and length of measurement depends on which of the two distinctive methods of X-ray detection is used: Wavelength-dispersive XRF instruments are equipped with very precise revolvable goniometers working as detectors (Rothwell and Croudace 2015). On the contrary, solid-state diodes of energy-dispersive XRF devices perform faster, allow continuous scanning of whole cores and slightly worse detection limits are still satisfactory for most elements of interest (Boyle 2001). Energy-dispersive XRF also enabled µXRF (also micro-XRF) analysis of uninterrupted sedimentary sequences with sub-millimetre resolution, otherwise unachievable with regular XRF devices (Davies et al. 2015). Micro-XRF has recently been applied, among others, in studies of varved records of Lake Suigetsu, Japan, where it can provide information on sub-annual scales (Marshall et al. 2012).

II.4.2 Organic geochemistry

In the Arctic regions, organic matter represents an important fraction of the lake sediments despite its low concentrations (Meyers and Teranes 2001). Oligotrophic lakes and barren landscapes contribute little organic matter for incorporation in sediments, but high preservation potential in cold conditions ascertains that very minor degree of decomposition takes place (Korhola and Weckström 2004). Nonetheless, often localised, post-burial diagenesis in oxic pore-water sediments must always be regarded as a possible setback. Organic matter mostly constitutes less than 5–10 % of total sediment mass, although locally in sediments of shallow lakes organic matter content may reach 70–80 %. Main sources of organic matter include terrestrial and aquatic plants, the former containing more carbon-rich lignin and cellulose than the latter (Meyers and Teranes 2001). Carbon is clearly the main element of interest when determining and describing the sedimentary organic matter, other elements found in organic matter, including nitrogen, sulphur, phosphorus, oxygen and hydrogen, are nonetheless similarly important.

Organic matter content can be estimated by weight loss on ignition (LOI), involving oxidation of carbon at 500–550 °C (Heiri et al. 2001). By further ignition at ~1000 °C carbonate content can be determined. Total organic carbon (TOC) equals only to half of LOI values, as carbon constitutes around 50 % of organic content (Meyers and Teranes 2001). TOC analysis, thanks to the more precise method of determination, is preferred over LOI, particularly in sediments with low organic matter content (Korhola and Weckström 2004). In the by-difference method, total carbon (TC) is detected by infrared radiation of CO_2 released by combustion at 850–1200 °C (Meyers and Teranes 2001, Nehyba et al. 2010). Inorganic carbon (TIC) is then distinguished from TOC by the fact that CO_2 derived from inorganic carbon exhibits phosphoric acid acidification. TOC can be obtained from the simple equation $TOC = TC - TIC$ (Meyers and Teranes 2001). Alternative direct-determination procedure requires the removal of inorganic (mainly carbonate) fraction first by chemical pre-treatment of the sample. Precision of the methods is comparable, unless very young sediments are studied (Meyers and Teranes 2001).

Nitrogen is an important constituent of organic matter, proteins in particular, and in lake sediments is almost entirely organogenic (Meyers and Lallier-Vergès 1999). The ratio of carbon to nitrogen then provides information on source of the organic matter. Aquatic organisms have generally lower C/N ratios (4–10), while cellulose-rich terrestrial plants exhibit C/N values >20. Provided that no significant post-burial degradation of either carbon or nitrogen occurs, C/N ratio reveals allochthonous or autochthonous source of the deposited organic matter (Meyers and Teranes 2001). Contribution of terrigenous material can thus be estimated, be it very young records revealing anthropogenic soil erosion (Massa et al. 2012), or much older Eemian record from Finnish palaeolake (Plikk et al. 2016). Alternatively, C/N ratio of bulk sediment is affected by changes of nutrient supply and overall water chemistry in isolation basins during transition from marine to freshwater phases, which was used to infer palaeosalinity and supplement biological proxies in relative sea-level reconstructions (Mackie et al. 2007). C/N ratio may be expressed as either weight or atomic ratio, and the option should be always reported (Meyers and Teranes 2001).

Sulphur usually strongly covary with carbon in oligotrophic lakes, as it forms a major part of seston, unless it reflects marine influence (Cohen 2003). Apart from S-bearing organic compounds, sulphur is also found in sulphates and sulphides, such as H_2S formed by reducing bacteria (using oxygen of sulphates for decomposition, i.e. oxygenation of organic matter). Subsequently, in anoxic conditions disulphide may react with Fe to form insoluble iron sulphide and iron minerals greigite and pyrite (Håkanson and Janson 1983).

II.4.3 Interpretation of some common elements and their ratios

Relative abundance and changes of elements and their ratios in sedimentary matter may reveal various processes within lakes, in their catchment or in wider region (Davies et al. 2015). Silicon is ubiquitous in sediments, as it forms (alumino-)silicates and is present in most minerals forming the Earth crust. Its presence therefore indicates detrital (lithogenic) input, quartz or sand fraction content (Cuven et al. 2010), although Si can be also biologically mediated, as some organisms, especially diatoms, use it to form silicate frustule (Brown 2015). This so called biogenic silica (BSi) reflects diatom palaeoproductivity, and correspondingly also the response of lake ecosystem to environmental changes (Boyle 2001). BSi can be measured directly by wet chemical method, but Si/Ti ratio was applied to estimate BSi as well (Brown 2015). Titanium is another lithogenic element indicating catchment erosion, but unlike Si, Ti is not bound to organic matter, making it suitable for normalising Si (in Si/Ti ratio) and inferring BSi content (Davies et al. 2015). Ti flux was found to reflect, depending on the environmental setting, either catchment runoff and corresponding past hydroclimatic regime (Balascio et al. 2011, Marshall et al. 2011), or aeolian activity (Olsen et al. 2013). In glacierised catchments, Ti concentrations serves as an indicator of glacial activity, especially if glacier advances over a certain threshold and begins to deposit glacially eroded material in a lake basin (Bakke et al. 2010, van der Bilt et al. 2015, Larsen et al. 2017). Care is, however, needed in regions with active volcanism, where Ti content may be affected by presence of tephra and volcanic pumices, precluding thus sometimes its use as a proxy for detrital input (Jouve et al. 2013).

Other major lithogenic elements indicating detrital input are Al, K, Fe, Rb and Zr (Davies et al. 2015). Aluminium is an immobile lithogenic element often accompanying Si in aluminosilicate rocks. Their ratio may reflect either chemical weathering in the catchment (Lopez et al. 2006), or sedimentary texture, as Al is primarily bound to clay and fine silt fraction, whereas Si to sand grains (Van Daele et al. 2014). Aluminium was also used for normalisation of heavy metals, since Al content should not be anthropogenically affected in industrially polluted sediments (Grygar et al. 2010). However, catchment and lake acidification may modify Al leaching from catchment and Al capture in sediments in a complex manner (Boyle 2001). Potassium is an alkali, relatively water-soluble element that, if suitably combined with less soluble Al, Ti or Rb, may reveal changes in catchment weathering regime (e.g. K/Ti ratio and Chemical Index of Alteration (CIA); Arnaud et al. 2012). Clays are generally enriched in K (Cuven et al. 2010, Kylander et al. 2011), enabling thus use of ratios such as Ti/K or Zr/K in grain size estimation (Fig. 1.3; Cuven et al. 2011, Marshall et al. 2011). Iron is ordinarily also bound to clay and fine silts, and both Fe and K are found in e.g. chlorites and micas (Cuven et al. 2010). Nevertheless, Fe does not simply represent a proxy for grain size or minerogenic input, because it is readily affected by reducing conditions during diagenesis (Mackereth 1966, Boyle 2001). Under anoxic conditions, unsoluble Fe^{III+} undergoes a transition to soluble Fe^{II+}, which is easily remobilised. This property, however, is used to investigate past redox conditions, usually together with manganese as Fe/Mn ratio, as Mn is slightly more affected by reduction than Fe (Boyle 2001). Past redox state can point to periods of enhanced water stratification or increased organic decay causing bottom-water anoxia (Davies et al. 2015). At last, Zr and Rb are both hard, resistant minerals, although Zr is bound to coarser fraction than Rb, representing thus a proxy for grain size (Zr/Rb ratio; Kylander et al. 2011). Presence of both Rb and Zr may be indicative of tephra (Damaschke et al. 2013).

Numerous other applications of XRF-detected elements are demonstrated in the body of literature (Davies et al. 2015). Calcium and strontium are often associated with detrital input in glacial or volcanic settings (Balascio et al. 2011, Shala et al. 2014), but in drier and carbonate environments they relate to authigenic or biogenic production of carbonates, and therefore to past changes in biological productivity or lake level lowering (Kylander et al. 2011, Olsen et al 2013). Aluminium, together with Mn, Cu, Ni and Zn, contain information on acidification of lake or its catchment (Boyle et al. 2001). Another anthropogenic impact, atmospheric or mining pollution, may be recorded in lacustrine sediments as an increase in content of Cd, Cu, Pb, Zn and Hg (Boyle 2001, Guyard et al. 2007). Organic matter content and past productivity can be estimated by Br concentration (Kalugin et al. 2007). Moreover, Br and B were found to measure palaeosalinity and oceanic influence, especially in coastal and low-lying lakes (Boyle 2001, Unkel et al. 2010). More common elements P, Na and Cl are, owing to their highly soluble nature, much less suitable for this type of reconstructions, even though they all play a dominant role in bioproductivity and salinity, respectively (Boyle 2001).

III. Settings

Three coring sites were selected for palaeoenvironmental reconstruction, all of them directly influenced by the oceanic circulation of the North Atlantic and local atmospheric patterns (Fig. 3.1). Svalbard represents the High Arctic, the northernmost region where the warming effect of the ocean currents can be recognised, specifically the West Spitsbergen Current, extending from the Norwegian Atlantic Current and North Atlantic Drift (Rudels 2009). The northeastern tip of Norway adjacent to Russian border and Kola Peninsula was chosen as the more southerly locality, enabling comparison of the High and Low Arctic. The final vertex of the triangle lies on the western brink of the area influenced by the North Atlantic, that is on the southwestern coast of Greenland, close to the capital Nuuk. The importance of the North Atlantic lies also in formation of oceanic deep water where saline Atlantic waters submerge, propelling thus the global thermohaline circulation (Rudels 2009). Physiographic description of these localities and the cored lakes is given below.

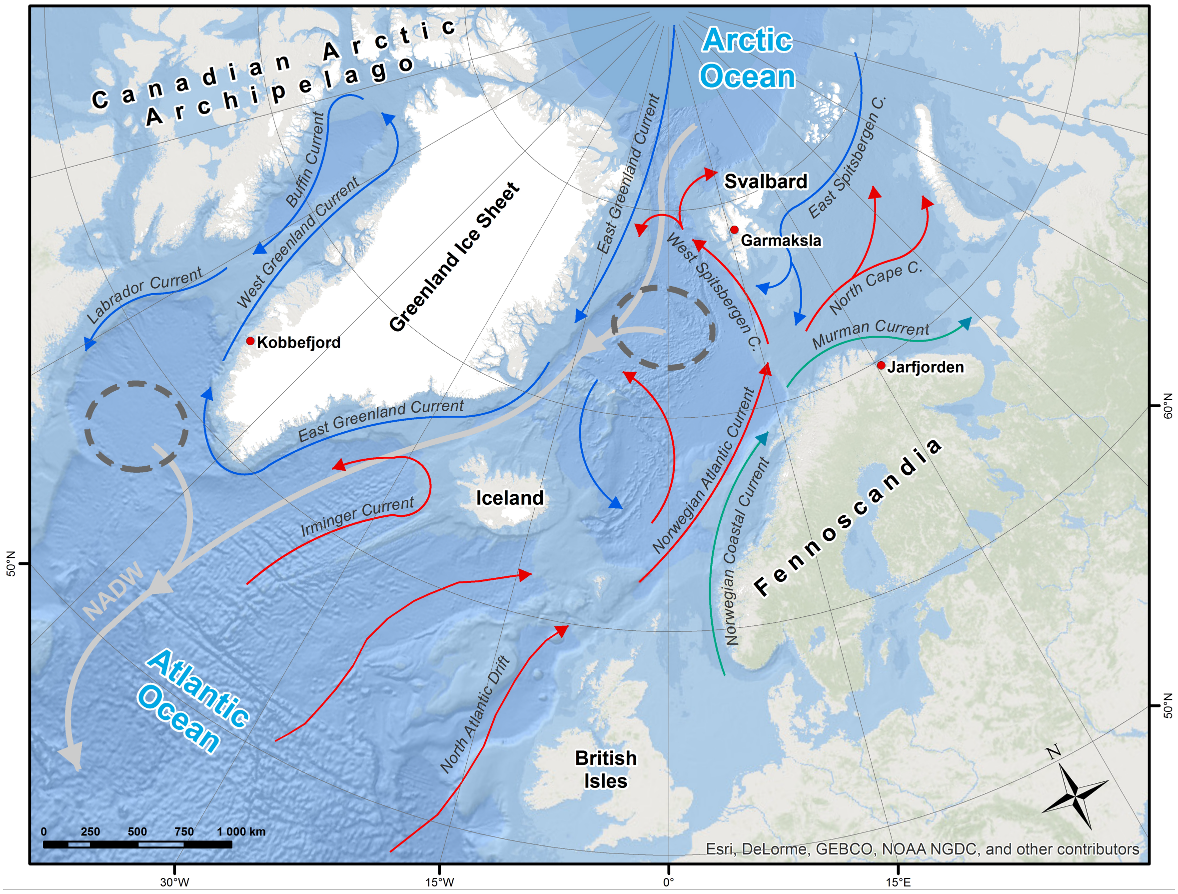

Esri, DeLorme, GEBCO, NOAA NGDC, and other contributors

Figure 3.1 General map of the area of interest with selected oceanographic and topographic features. Three research localities are denoted by red points. Warm and cold surface ocean currents are depicted as red and blue arrows, respectively. Cyan arrows represent transformed, low-salinity coastal currents. Thick grey arrow schematically illustrates an intermediate-depth flow of North Atlantic Deep Water (NADW), together with its main areas of formation, i.e. sinking of more saline water (dashed line circles).

III.1 Lake Garmaksla, central Svalbard

Garmaksla is located near the western margin of the Billefjorden Bay (continuation of the Isfjorden) on the island of West Spitsbergen, Svalbard. The Svalbard Archipelago is situated in the High Arctic, between 74°20’ and 80°50’N and 10–33°E, ~900 km north of mainland Norway and 1300 km south of the North Pole (Hisdal 1998). Svalbard lies on the edge of the Eurasian continental shelf and separates the Atlantic and Arctic Ocean. The land area is 61,200 km^2 and presently glaciers cover ~60 % of Svalbard (Hagen 1993).

Palaeogeographic history of Svalbard is closely related to evolution of Fennoscandia and Greenland, as all these regions were a part of Laurentia as early as Precambrian, when they were located in the Southern Hemisphere. As Laurentia and associated terranes drifted northwards, they experienced phases of orogeny (Caledonian, Variscan) as well as sedimentation (especially in Mesozoic) and volcanism (Hisdal 1998). Relatively late opening of the North Atlantic Ocean (in Paleogene) caused the considered provinces to move away from each other and contributed to reorganisation of the global circulation; oceanic currents were able to transport excess heat and moisture from the tropics to higher latitudes, up to 80°N. Simultaneously with global cooling, abundant supply of moisture instigated extensive glaciations of the Northern Hemisphere, which drove the Earth further into a repeating cycle of Quaternary ice ages (Zachos et al. 2001, Bradley 2015). In the Late Weichselian, Svalbard was covered by the Barents-Kara ice sheet several hundred metres thick (Ingólfsson and Landvik 2013); its retreat caused subsequent glacio-isostatic uplift

Figure 3.2 Lake Garmaksla overlooking the Billefjorden Bay. Deep central part of the lake with grown algae, scarp slope and patterned ground are well visible. In the background are the summit of Pyramiden and Nordenskiöldbreen tidewater glacier.

reaching ~90 m in central Svalbard and formation of marine terraces up to 65 m a.s.l. (Luláak et al. 2017). Billefjorden Bay was occupied by grounded ice stream before 11.2 ka BP, but retreated into its present form, tidewater glacier Nordenskiöldbreen, that remained more or less stable throughout the Holocene (Baeten et al. 2010).

Polar tundra climate dominates the archipelago, according to Köppen-Geiger classification (ET; Kottek et al. 2006). However, the climate is remarkably mild given the latitude, owing to the warming effect of the oceanic currents. Average seasonal air temperature at Longyearbyen Airport weather station reaches 5.2°C in summer (JJA) and –11.7 °C in winter (DJF) for the period AD 1981–2010 (Førland et al. 2011). Even in winter, nonetheless, air temperature may surpass 0°C during advection of warm maritime air masses (Hisdal 1998). Climate in the fjord head of Billefjorden is more continental, mean annual air temperature reaches –6 °C, and winters are colder (around –15 °C; Gibas et al. 2005, Láska et al. 2012). Annual precipitation (both rain and snow) totals are highly variable, but in general do not exceed 500 mm, in central Spitsbergen even less, around 200 mm. Snow cover is usually present from September to May-June. Thanks to the warm West Spitsbergen Current, practically no sea ice forms in the area west of Svalbard (Aagaard et al. 1987). However, seasonal sea-ice cover develops in inner fjords and is usually present, in case of Billefjorden, from December to May (Láska et al. 2012), although may break up earlier, which was the case in recent years.

III.1.1 Lake, basin, catchment and geomorphological setting

Lake Garmaksla is situated ~320 m a.s.l., 8 km south of Pyramiden settlement and 2 km east of Jotunfonna ice cap. The lake is named after the nearby mountain Garmaksla (379 m a.s.l.). The lake is ~250 m long and ~110 m wide, and its primary orientation follows the Billefjorden Fault Zone (BFZ) that runs in north-south direction through central Svalbard (Dallmann et al. 2004; Fig. 3.3B). The lake basin probably formed as a result of deep-seated gravitational slope deformation (*sensu* Soldati 2004 or Hungr et al. 2014) along the fault plane of BFZ. Subsidence of the rock block induced bulging in the lower part of the slope (visible in the digital elevation model of Norsk Polar Institut), while twin ridge with a trench in between was formed in the upper part of the slope. Water-filled depression is located right next to the fault scarp (Fig. 3.3C). The lake drainage basin covers an area of 0.15 km^2 and is underlain dominantly by calcareous sandstones of Wordiekammen formation, belonging to Dickson Land Subgroup of Carboniferous to Early Permian age (Dallmann et al. 2004).

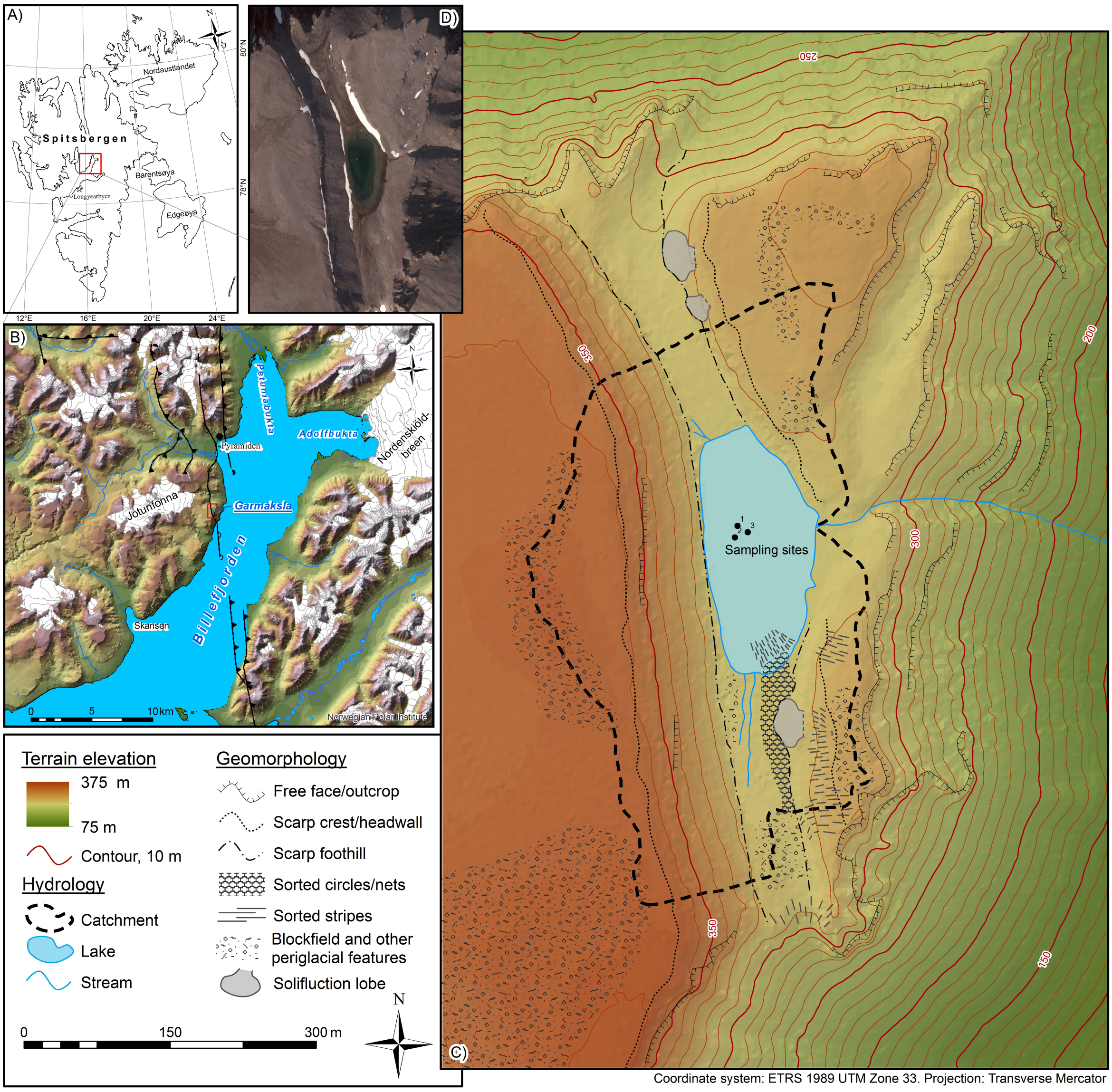

Coordinate system: ETRS 1989 UTM Zone 33. Projection: Transverse Mercator

Figure 3.3 Lake Garmaksla lies in central Svalbard (A), close to the Billefjorden Bay, where the main fault divides the geologically distinctive western and eastern parts of Svalbard (B). Catchment and geomorphic landforms of Garmaksla are depicted in C), and orthophotograph of the lake catchment in D). Data source: Norsk Polarinstitutt.

Devonian to Carboniferous sedimentary rocks of Wood Bay and Ebbadalen formations, respectively, are found lower beneath the lake catchment. Occasional findings of redeposited heterogenous pebble-sized clasts around the lake basin, consisting of Devonian (Old Red) and Carboniferous sandstones, siltstones (marls) and migmatites, probably originate in outcrops of Early Carboniferous conglomerates of Hørbyebreen and Mumien formations, Billefjorden Subgroup (M. Hanáček, personal communication).

A number of periglacial features are present in the lake catchment, including blockfields, frost-riven cliffs and solifluction lobes (Fig. 9.1 in Appendix). In low-lying water-saturated plain adjacent to the lake, abundant sorted circles (diameter >1 m), nets, polygons and stripes are found. Abundance of these periglacial landforms indicates a long-term evolution of local relief that was not subjected to glaciation at least since the late Holocene, considering the time necessary for development of such well-developed periglacial features under the local conditions (Uxa et al. 2017). Moreover, maximum Holocene glacier advances in this region occurred during LIA (Svendsen and Mangerud 1997, van der Bilt et al. 2015, Miller et al. 2017), but since there is no evidence of such late glaciation in the studied catchment, the area was presumably unglaciated throughout the Holocene. Permafrost at this relatively high-altitude locality may reach depth of 500 m (Humlum et al. 2003). Average active layer thickness in the catchment is unknown, but should range from 0.4 to 2.5 m (Gibas et al. 2005). Ground surface in the catchment is covered by weathered regolith that only on few vegetated patches displays signs of pedogenesis; the soils on Svalbard can be generally classified as leptic cryosols (Jones et al. 2009).

Garmaksla is a high-altitude, ultra-oligotrophic, monomictic lake. Its maximum depth was determined by bathymetric sonar profiling to be 5 m and sediment thickness of ~1 m estimated by probing. Lake surface are is 2.28 ha. Three cores G13/1, G13/2 and G13/3 were recovered from the depocenter of the lake. The lake is covered by ice for major part of the year. The ice cover usually forms in late August or September and thaws in June or July, although during cold years may persist to August (J. Kavan, personal communication). Lake water is slightly alkaline (pH 8.5–9.2), conductivity reaches 167 $\mu S \cdot cm^{-1}$ (Pinseel 2014) and dissolved oxygen content 12.7 $mg \cdot l^{-1}$ (Čepová 2013). Diatoms and aquatic mosses are the main primary producers of the lake. Dominant present diatom species include *Achnanthidium spp*, *Rossithidium petersenii*, *Cymbella* spp., *Denticula* spp., *Navicula* spp. and *Nitzschia* spp. (Pinseel 2014). Zoobenthos is represented by water larvae of chironomids, e.g. *Micropsectra radialis* and *Procladius* spp. (D. Vondrák, unpublished data). Zooplankton includes a rotifer species (*Polyarthra dolichoptera*) and two crustaceans, namely copepod *Cyclops abyssorum* and cladoceran *Chydorus sphaericus* (D. Vondrák, unpublished data).

III.2 Jarfjorden, NE Norway

Sedimentary cores were recovered from five lakes in the Jarfjorden area (administratively belonging to Sør-Varanger municipality, Finnmark county, Norway), located 20–30 km east from Kirkenes in the vicinity of the Norwegian-Russian border. The local bedrock comprises Archaean and Proterozoic crystalline rocks, chiefly gneisses and granites (Corner et al. 1999). Jarfjord migmatitic gneisses represent some of the oldest rocks of the Baltic Shield, their age being estimated to 2.7–2.9 Ga. These are supplemented by late to post-kinematic

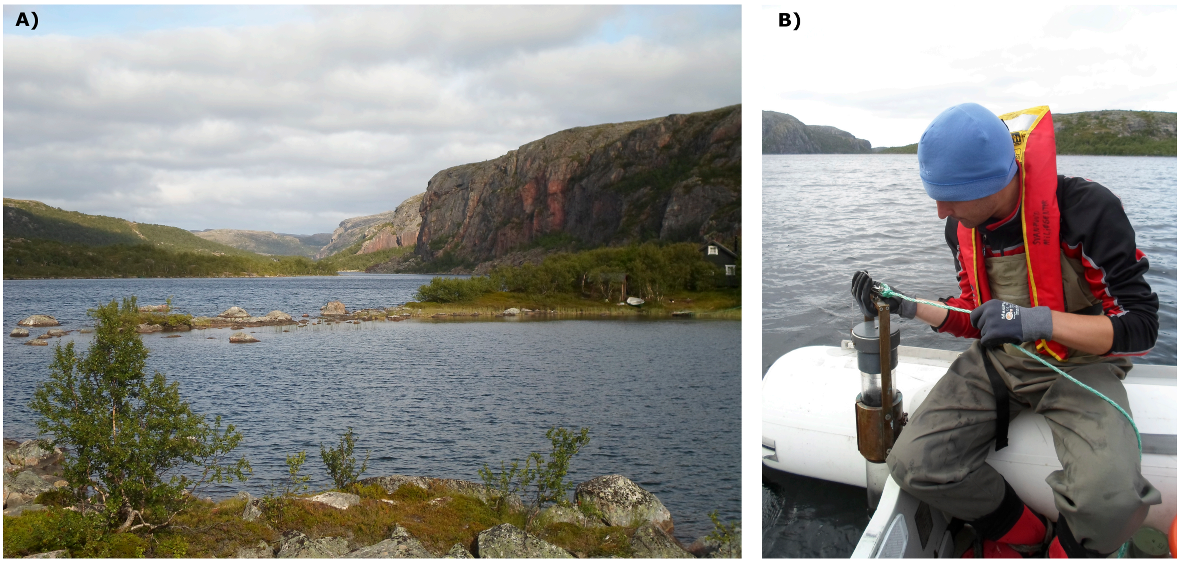

Figure 3.4 View over Vintervollvatnet towards Longvatnet that stretch along the linear scarp with a prominent free face on the right-hand side of the picture (A); the more protected, south-oriented slope of the north bank is covered with birch and juniper. Lowering of the Russian gravity corer into waters of Holmvatnet from the rubber boat (B).

granitic to monzonitic intrusions nearby the drilled lakes catchments (Berthelsen et Marker 1986). Highly undulating relief, providing ideal conditions for formation of numerous lakes, was sculpted by the overriding Fennoscandian Ice Sheet during multiple Quaternary glaciations (Stokes et al. 2014). The final, Late Weichselian retreat in nearby Varangerfjorden occurred rapidly around 14–15 ka BP (Stokes et al. 2014) and the Jarfjorden area might have been deglaciated by 13–14 ka BP (Stroeven et al. 2016. During the Younger Dryas stadial (YD) a transient readvance formed a terminal moraine passing through the Jarfjorden area (Corner et al. 1999, Møller et al. 2002, Stroeven et al. 2016). Other glacial landforms include De Geer moraine ridges and ice-contact glacifluvial sediments (Corner et al. 1999, Stroeven et al. 2016). Deglaciation of the area was completed by the beginning of the Holocene, ensuing in regional glacio-isostatic rebound of ~90 m (Corner et al. 1999). Permafrost is present in the Jarfjorden area only sporadically at higher altitudes and is expected to degrade in the near future (Farbrot et al. 2013).

According to the criteria of Köppen-Geiger classification, the region experiences the fully humid, boreal climate with cool summers (Dfc; Kottek et al. 2006). MAAT in Kirkenes reaches 0.2 °C (Myking et al. 2009), while it decreases to –2.5 °C towards inland and upland areas in the south due to higher altitude, greater continentality and diminished oceanic influence (Hofgaards et al. 2012). Annual precipitation amounts to 350–500 mm in the region and the snow cover is present since December to May (Myking et al. 2009). Mean temperature of only two summer months exceeds 10°C isotherm, also regarded as northern treeline and the southern limit of the Arctic. South of this 10°C isotherm, forests of Scots pine (*Pinus Sylvestris* L.*)* dominate, while northwards downy birch (*Betula pubescens* Ehrh.) prevails (Hofgaards et al. 2012). Regional flora also includes common juniper (*Juniperus communis*), cloudberry (*Rubus chamaemorus*), European blueberry (*Vaccinium myrtilus*), and species typical for mires (*Eriophorum*, *Carex*, *Sphagnum*). The most iconic fauna species are represented by reindeer (*Rangifer tarandus*), elk (*Alces Alces*) and brown bear (*Ursus arctos arctos*).

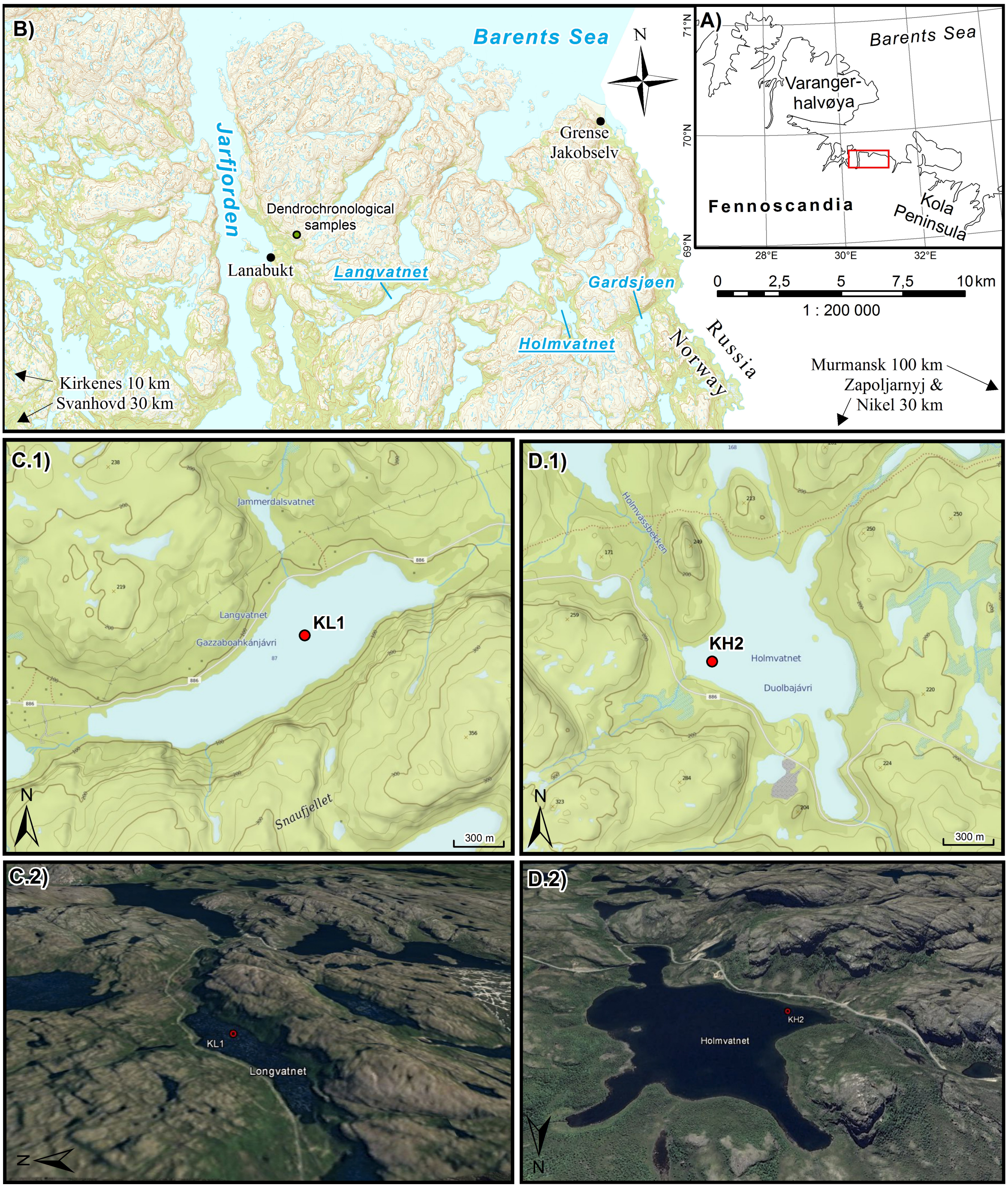

Figure 3.5 Location of the studied area Jarfjorden within Kola Peninsula region (A) and of cored lakes Langvatnet (C.1) and Holmvatnet (C.2) with denoted positions of cores KL1 and KH2. Dendrochronological samples were taken close to the settlement Lanabukt (B). Aerial views of the studied lakes in C.2 and D.2 illustrate to what degree the landscape was glacially scoured and the importance of tectonic and structural control on linear glacial erosion. Data sources: Kartverket (Norwegian Mapping Authority) and Google Earth.

Sedimentary sequences from two oligotrophic, dimictic lakes, Langvatnet and Holmvatnet, are thoroughly described in this thesis. Langvatnet (also known as Langvann (in Bøyum 1970) or Gazzaboahkánjávri in Saami language) lies at 87 m a.s.l., covers an area of 0.68 km^2 and its maximum depth reaches 34.5 m (Bøyum, 1970). The lake is elongated in WSW-ENE direction (2.25 km long to 0.6 km wide) and is drained via multiple lakes into Jarfjorden. Its catchment covers 18 km^2 and circumference is 16.5 km long. Transparency of the green-coloured water column measured by the Secchie disk amounts to 11 m, which is an average value for local lakes with intermediate organic matter content (Bøyum 1970). Langvatnet was markedly thermally stratified (thermocline occurred in 5–8 m depth), had a neutral to slightly acidic active reaction (pH decreases with depth from 6.9 to 6.5) and low specific conductivity (on the 27th July 1966 after Bøyum 1970). Sea spray and partly precipitation are the primary sources of major ions. The epilimnion was rich in oxygen, whereas hypolimnetic water was oxygen-deficient (Bøyum 1970). Holmvatnet, the second investigated lake in this locality also known as Duolbajávri, is situated 7 km east of Langvatnet at elevation of 158 m a.s.l. The lake is nearly 2 km long, 0.85 km wide, and covers an area of 0.8 km^2. Catchment area is estimated at 13.5 km^2 with perimeter 24 km. Maximal and coring depths are unknown, nor is there any previous literature dealing with this lake. The core was recovered in the deepest part of the western embayment close to the lake outflow. Apart from these two lakes, sediment cores were also taken from Lake Gardsjøen further east (cores KG1 and KG3; 69°42'21"N 30°50'43"E), unnamed lake next to the road No. 886 (core KP1; 69°42'22"N 30°48'8"E) and an infilled peat bog next to Lake Forste Hogfjellvatn (core KS1; 69°43'55"N 30°48'41"E; Fig. 9.3). Moreover, during this field campaign, also dendrochronogical samples of *Juniperus communis* were collected close to the settlement of Lanabukt (Lexa 2015).

III.3 Kobbefjord, Greenland

Final coring site presented in this study in the Kobbefjord Bay area (or Kangerluarsunnguaq), southwestern Greenland (64°10´N; 51°19´E), 20 km east from the capital Nuuk. The local bedrock is formed by supracrustal rocks (amphibolites and gneissic metasediments), orthogneisses, gneisses, post-tectonic granite complexes and intermediate and mafic intrusions (Escher and Pulvertaft 1995). In LGM the whole island was covered all the way to the continental shelf (20–40 km offshore) by the Greenland Ice Sheet (GrIS), which retreated inland and exposed the study area by the beginning of the Holocene (Funder et al. 2011). Area just outside of Nuuk was deglaciated by 10.7 ± 0.6 ka BP (Larsen et al.

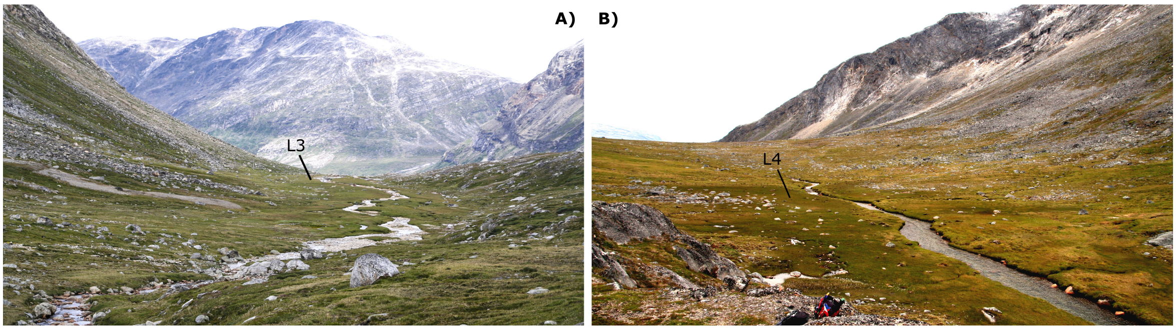

Figure 3.6 Kobbefjord sedimentary cores were retrieved from infilled lake basins on the left (core L3 in A) and the right (core L4 in B) side of the through-flowing stream. Photos by Jiří Lehejček.

2014, Winsor et al. 2015). The Little Ice Age ended by the beginning of the 20th century (Kjeldsen et al. 2015) and the local glaciers and ice caps continuously retreated since then (Weidick et al. 2012).

Relatively mild, low Arctic climate of the Kobbefjord bay is mediated by influence of the West Greenland Current (WGC) of the North Atlantic origin (Fig. 3.7; Seidenkrantz et al. 2007). According to Koppen-Geiger classification, the area belongs to polar tundra climate (ET, Kottek et al. 2006). Mean annual precipitation in the nearby capital Nuuk reaches 777 mm, with mean annual temperature of –1.3 °C, and mean summer (JJA) temperature of 5.8 °C (Nuuk 4250 meteorological station; period 1981–2010; Cappelen 2013). Just 17 km towards inland, Kobbefjord experiences more continental climate, with the coldest month being February (mean air temperature –7.8 °C) and the warmest July (6.9 °C; the mean for years 1958–2010; INTERACT 2012). Lake ice breaks up usually in May or June. On average, 25–50 % of the total precipitation falls as snow (Larsen et al. 2017). Shallow lithosols, followed by cambisols, are prevailing soil types in the area (Polická 2014). Flora comprises typical low Arctic species, such as copse, fen or dwarf-shrub heaths.

Two sediment-infilled lakes drained by the same river were cored in order to retrieve the lake sediments. The coring sites L3 and L4 are located at 195 and 215 m a.s.l., respectively, in the Naqinnera Silarleq (Yderdal) valley, a wide glacial trough connecting Kobbefjord and Ameralik fjord (Fig. 3.7D). The valley slopes are steep, with remnant hanging glaciers (rapidly melting since the 20th century; Larsen et al. 2017) and snowpacks feeding the streams. Glacially overdeepened basins in the cascade-like profile of the valley bottom functioned as sediment traps after the last deglaciation and were subsequently filled. The sediment-infilled lake areas are presently covered by dense moss cushions, which are cut by the stream flowing to the Kobbefjord bay. The lake basins catchments are characterized by relatively dry sand-silt soils and scattered boulders with sparse vegetation cover in flat parts of the catchments and gravel-boulder scree on valley sides of the trough. The total catchment area is 4.13 km^2, of which 2.22 km^2 pertains to the upper lake L4 sub-catchment. The cored locations represent the closing profiles of both lake sub-catchments.

Table 3.1 Summary of information on the cored lakes and locations

Locality	Lake	Geographical coordinates of coring site	Sedimentary core designation	Date of retrieval	Corer used	Uncompressed length (cm)	Compression factor	Sampling interval (cm)
Billefjorden, Svalbard								
	Garmaksla	78°36'11"N, 16°20'17"E	G13/1	27th July 2013	Uwitec	79	6.8%	1
			G13/2			66	4.8%	1
			G13/3			72	2.9%	1
Jarfjorden, NE Norway								
	Langvatnet	69°43'18"N, 30°35'11"E	KL1	10th August 2014	Russian	38	-	0.5
	Holmvatnet	69°42'43"N, 30°45'23"E	KH2	9th August 2014	gravity	40	4.2%	0.5
Kobbefjord, SW Greenland								
	Infilled lake 1	64°06'55"N, 51°23'10"W	GR13-L4	9th August 2013	Uwitec	61	14.2%	0.5
	Infilled lake 2	64°07'22"N, 51°23'25"W	GR13-L3			41	-	0.5

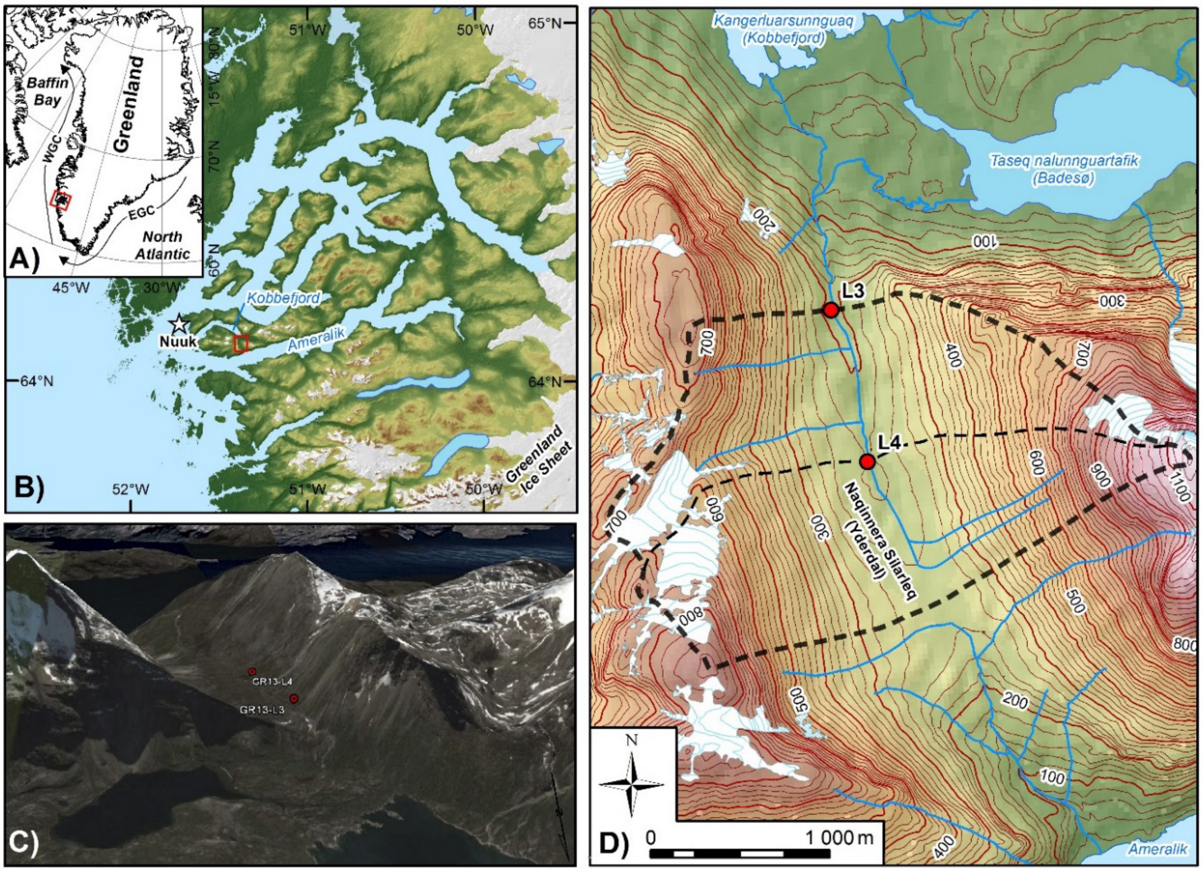

Figure 3.7 Location of the study area within Greenland is denoted by red square inset, with the warm West Greenland Current to the west (A). The Kobbefjord is set among numerous fjords and islands, Greenland Ice Sheet is further to the east (B). Location of coring sites L4 and L3 in the Naqinnera Silarleq valley from aerial view (C) and on topographical map (D), with delineation of their catchments (dotted line) and main physiographic features is shown. Data sources: Howat et al. 2014 (Greenland Ice Mapping Project DEM), Google Earth.

IV. Materials and methods

Sedimentary sequences obtained by gravity corer drilling were dated and subjected to physical and geochemical analyses. Non-destructive analyses were conducted first, i.e. measurement of magnetic susceptibility, elemental composition by X-ray fluorescence (XRF) and short-lived radioisotope dating. The following destructive analyses comprised measurements of grain size distribution, content of carbon, nitrogen and sulphur (CNS, TIC/TOC/TS) and radiocarbon dating.

IV.1 Retrieval of lake sediments

Material for analyses was retrieved using a modified Kayak gravity corer that was in majority of cases released down from a boat in the central part of a lake. The sampling site in Kobbefjord could have been reached on foot, the corer was thus pushed into the sediments manually. Mostly the gravity corer made by Uwitec (Mondsee, Austria) with a diameter of 60 mm was used, although at a few locations in northeastern Norway several cores were sampled using a slightly different, russian type of gravity corer with 80-mm diameter. The main advantage of a gravity corer compared to piston corer lies in preservation of water-sediment interface undamaged (Glew 1989); on the other hand, the corer needs not penetrate through the whole bulk of sediments and reach the bottom, which often leaves us guessing the overall sediment thickness. The sediment cores were sliced in 0.5/1-cm steps, either directly at the sampling location or later in the laboratory, and stored in plastic bags in the cold.

IV.2 Dating/Chronology

The uppermost 10 dried sediment samples of cores L3 and L4 were measured by gamma spectroscopy for the specific activity of isotopes ^{210}Pb, ^{137}Cs and ^{226}Ra in the Radiometry laboratory, Institute of Geochemistry, Mineralogy and Mineral Resources, Charles University in Prague. The rate of radioactive decay (in Bq/g) was then used for distinguishing the supported and unsupported ^{210}Pb, abundance of which was modelled assuming the constant rate of supply (CRS; Appleby and Oldfield 1978). Specific activity of ^{137}Cs was used for validation of the age-depth model by association of ^{137}Cs peaks with the nuclear bomb test maximum before 1963, and possibly Chernobyl nuclear accident in 1986 (Appleby 2008).

Selected terrestrial macrofossil remains or, in the absence thereof, bulk sediment samples were dated at Poznań Radiocarbon Laboratory by means of Accelerated Mass Spectrometry (AMS). The results were calibrated with the IntCal13 calibration curve for the Northern Hemisphere (Reimer et al. 2013) in the OxCal 4.2 software (Bronk Ramsey 2009). Age-depth modelling was performed in the R-code package *clam* (Blaauw 2010), using linear interpolation method and 10 000 iterations. Age and uncertainty envelope acquired by modelling for every integer centimetre was then recomputed for each mid-point of the sample depth. Accumulation rate was also calculated for every layer based on the relation of the sediment depth (corrected for compaction) and the modelled best age estimate of a corresponding layer.

IV.3 Magnetic susceptibility

Measurement of magnetic properties was performed on the Kappa Bridge MFK1-A instrument (AGICO, Ltd.) in the Institute of Geophysics of the Czech Academy of Sciences or in the Institute of Geology and Palaeontology of the Charles University, Prague. Mass-specific magnetic susceptibility (χ) was measured at frequency of 976 Hz with induced magnetic field 300 mA. Furthermore, high-frequency χ (χ_{F2} at 3,904 Hz, χ_{F3} at 15,616 Hz; with applied magnetic field of 200 mA for all three frequencies) was measured in the cores from Kobbefjord and northeastern Norway in order to calculate frequency-dependent magnetic susceptibility (χ_{FD}), as suggested by Dearing et al. (1996). χ_{FD} enables e.g. identifying superparamagnetic mineral grains found in very fine grain size fraction (~0.02 µm). Although low and high frequencies (χ_{F1} and χ_{F1}) do not correspond exactly to the those originally introduced by Dearing et al. (1996) (470 and 4700 Hz), they can be nonetheless considered comparable as they also differ by about one order of magnitude and lie in the similar frequency range. Samples were measured in their original wet condition (Kaplan et al. 2002). We thus avoided drying that can induce oxidation of some iron-bearing minerals and non-linearly change χ signal in the core (Kletetschka et al. 2015). It is necessary, however, to assume relatively constant water content throughout the cores and consider diamagnetic character of water altering the absolute χ values when comparing the cores.

IV.4 Grain size distribution

Particle-size distribution was measured in the Institute of Geology of the Czech Academy of Sciences using the Cilas 1190 particle-size analyser, which employs the method of laser diffraction and detects the grain diameters of 0.04–2500 µm. Chemical pretreatment of the samples comprised leaching in heated 10% KOH solution in order to eliminate flocculation. With the same purpose, ultrasonic dispersion was applied during the measurement itself (in addition to using distilled water and obscuration of ~5 %). Volumetric grain-size parameters (mean grain size (MGS), clay, silt and sand content, sand/silt ratio, mode, sorting, skewness, kurtosis, polymodality) were calculated from the raw grain-size data in the GRADISTAT software, v8.0 (Blott and Pye 2001), and are presented in graphical method (in µm) after Folk and Ward (1957).

IV.5 Geochemistry (XRF, organic geochemistry)

Total content of selected elements was determined by means of energy dispersive XRF using Olympus Delta Premium instrument (Innov-X, USA) in the Department of Geography, Masaryk University (cores from Garmaksla lake and NE Norway), and in the Department of Soil Science and Soil Protection, Czech University of Life Sciences in Prague (Kobbefjord cores). Each sample was measured three times for 90 s in Geochem/Vanad mode and the results averaged. Elemental ratios were preferred over element concentration in presenting the data as they partially circumvent the problems of variable water and organic content and surficial inhomogeneities of the samples (Boyle et al. 2015).

Dried sediment samples from Kobbefjord were homogenized and grounded by mill (Vibratory Micro Mill PULVERISETTE 0, Fritsch, Germany). Total carbon (TC), nitrogen (TN) and sulphur (TS) contents were determined in Kobbefjord cores by means of Elementary Analyzer Flash 2000 NCS (Thermo Scientific, UK) in the Department of Soil Science and Soil Protection, Czech University of Life Sciences in Prague. Complete conversion of inorganic sulphur was achieved by adding of 5 mg of vanadium pentoxide to each sample. In the same laboratory, element composition of Kobbefjord samples were measured using the method of inductively coupled plasma-optical emission spectrometry (iCAP 6500 Radial ICP, Thermo Scientific, UK) under standard conditions (Tejnecký et al. 2015) in order to estimate content of biogenic silica (BSi). In Garmaksla cores, total organic and inorganic carbon (TOC and TIC, respectively) and TS contents were determined in the Central Laboratory of the Czech Geological Survey (Brno) using Metalyt-CS-1000-S instrument (ELTRA GmbH, Germany). Total carbon (TC) content was determined by infrared detection of CO_2 released from the sample by combustion at 1,200 °C. Carbon dioxide exhibiting phosphoric acid acidification is then ascribed to TIC component, while TOC is computed by subtracting TIC from TC (Nehyba et al. 2011).

IV.6 Data analyses

Stratigraphic correlation of the cores from the same lake or locality was verified on selected proxies by visual wiggle matching and sequence slotting, i.e. mathematically optimal combination of two ordered stratigraphical sequences, in CPLSlot 2.4b software (Thompson et al. 2012). Relative order of depths obtained by stratigraphically constrained sequencing was afterward recalculated to ages and interpolated. Principal component analysis (PCA) of standardised physical and geochemical data and computing of correlation coefficients were performed in SPSS 23 (IBM software). Suitability of the data for PCA was validated by Kaiser-Meyer-Olkin and Bartlett's tests. Missing values were replaced by mean, or in case they made up more than one fourth of all cases, the corresponding variable was excluded from the factor analysis. Two primary components with the highest eigenvalues were extracted based on correlation matrix and rotated by Varimax method. Component scores were determined by regression. All presented correlations are significant at the 0.01 level unless stated otherwise. Not measured data or values below limit of detection were omitted from numerical analyses. All graphs were created in Grapher 11 (Golden Softw Results and interpretations

V. Results

V.1 Garmaksla Lake, central Svalbard

During field campaign in Billefjorden in 2013, three cores from Lake Garmaksla, designated G13/1, G13/2 and G13/3, were recovered from the depocenter, distant less than 5 m from each other. Results of visual description and measurements of physical and chemical parameters are presented in the following subchapters.

V.1.1 Lithostratigraphy and chronology

All three cores are composed mostly of dark, very organic gyttja that was distinctly laminated in the middle part. Laminae are formed by lighter, presumably less organic bands a few millimetres wide, that are intercalated between the gyttja matrix. Lamination is found in the upper 40, 47 and 38 cm in cores G13/1, G13/2, and G13/3, respectively, although in the topmost 5–8 cm laminae gradually disappear. Poorly decomposed, sandy gyttja of somewhat lighter colour forms the upper 5 cm of the cores. The lamination represents the basis for correlation of the three cores, enabling the comparison of individual proxies measured on different cores and providing therefore the common chronostratigraphic framework. The boundaries of lamination serve as tie points, by which the cores were linked together, but this was further supported by agreement of selected proxies (χ, TOC, TS, TC/TS), as will be shown further (see section VI.1.1 on age modelling). Radiocarbon dates from G13/1 and short-lived radioisotope dates from G2013/2 were thus linked together to form a composite age-depth model, which was subsequently applied on all three cores including G13/3, where no dating was performed. Throughout the cores, organic macro- and microfossils are to be found, including moss and lichen remains, cladocerans, chironomids and diatoms (Fig. 9.1 in Appendix).

The core G13/1 was 79 cm long (during cutting was compressed to 74 cm). Sediment can be characterised as silty gyttja, although the upper 10 cm contain numerous sand grains, whereas below 58 cm sedimentary matter appears more clayey. Lamination is found between 40 cm and 5 cm depth, with gradual transitions on both ends. Laminae have variable thickness on the order of few millimetres. The core G13/2 was originally 66 cm long (compressed to 63 cm). Sediment is formed again by silty gyttja, with progressive coarsening of the material upwards (supported by grain size analysis of this core, see V.1.2). The lowermost 8 cm are characterized as clayey silt, and the top 10 cm as sandy silt. Laminae

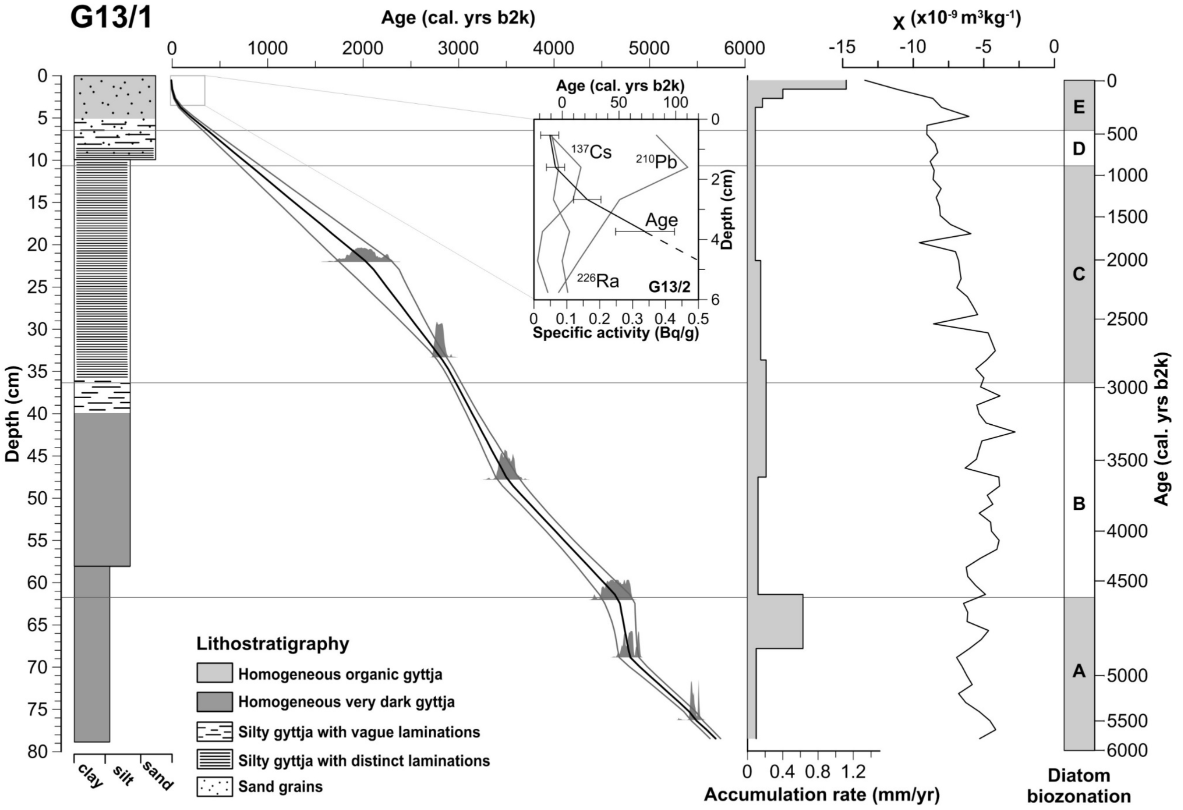

Figure 5.1 Lithological description of the core G13/1 (left); best estimate age-depth model (black line) with 2σ uncertainty envelope (grey lines) is based on six ^{14}C dates (shown as probability distribution curves of calibrated dates) from G13/1, and supplemented by short-lived radioisotope dating of the topmost six samples from G13/2 (inset); accumulation rate and magnetic susceptibility (χ; middle right); and diatom biozonation based on Pinseel 2014.

occur between 47 and 5 cm depth. The core G13/3 was 72 cm long (after compression 70 cm), with lamination present in depth 6–38 cm. Sedimentary matter can be characterised as silty gyttja.

Seven AMS ^{14}C dates in total, derived from terrestrial organic macroremains (mostly mosses), were acquired from the profile G13/1, and are presented in Table 5.1. The lowermost six dates are placed almost linearly in chronostratigraphic succession, with no age reversals, and allowed for construction of a reliable age-depth model (Fig. 5.1).

Table 5.1 Summary of the radicarbon dated samples from G13/1 from Lake Garmaksla.

Sample	Laboratory number	Depth (cm)	mg C	^{14}C yrs BP	cal. b2k (± 2 σ)	Min-Max age cal. b2k (± 2 σ)
G13/1-6	Poz-71854	6,9	0.3	100.75 ± 0.38 pMC	44 ± 1	43–45
G13/1-21	Poz-65688	22,4	0.1	2040 ± 120	2075 ± 290	1785–2364
G13/1-32	Poz-61448	34,2	>1	2725 ± 30	2866 ± 55	2811–2921
G13/1-45	Poz-65689	48,0	>1	3240 ± 60	3533 ± 126	3407–3658
G13/1-58	Poz-65691	61,9	0.3	4140 ± 60	4695 ± 191	4504–4885
G13/1-64	Poz-71855	68,9	>1	4185 ± 35	4763 ± 127	4636–4889
G13/1-72	Poz-61450	76,9	>1	4805 ± 35	5586 ± 66	5520–5562

However, one date (G13/1-6) from the depth 6.9 cm was excluded due to content of modern carbon. This depth would correspond to the age of 44 cal. yrs b2k according to ^{14}C dating in G13/1, but the equivalent layer appears much older in the core G13/2, which was dated by ^{210}Pb and ^{137}Cs. Peak of radiogenic activity of ^{137}Cs is located at ~1.7 cm (and should represent the maximum of nuclear weapon testing in AD 1963). Together with almost linear decrease of unsupported ^{210}Pb in the upper 6 cm, this allowed estimating the age at 3.5-cm depth, which should lie in the interval 47–99 yrs b2k (i.e. AD 1901–1953, with 2σ uncertainty; CRS model applied). According to this result, depth of 6.9 cm in G13/1 should be much older than the modern carbon date, and should rather correspond to ~400 yrs b2k, as implied from the age-depth model. In spite of this, dramatic changes in diatom assemblages take place at 11 and 6 cm in G13/1, and are well comparable with other records of post-LIA responses of biological communities to rapid warming (Pinseel 2014), suggesting thus younger age of the upper 10 cm in the master core.

Composite age-depth model produced in Clam software (curve fit = 13.91, linear interpolation method with 10,000 iterations; Blaauw 2010) suggests that G13/1 spans the last ~5,700 yrs. Throughout the sedimentary history, the accumulation rate reached only 0.1–0.2 $\text{mm}\cdot\text{yr}^{-1}$, even though it accelerated near the core's top (up to 1.1 $\text{mm}\cdot\text{yr}^{-1}$, caused by less sediment compaction?) and in depth 62–69 cm (0.6 $\text{mm}\cdot\text{yr}^{-1}$), where the two ^{14}C dates almost overlap. Whether this latter acceleration is caused by reworking of one of the dated macroremains via slumping or bioturbation, or whether it truly reflects the increased rate of accumulation, remains unresolved.

V.1.2 Physical proxies

Magnetic susceptibility is very weak in all three cores, exhibiting only negative values, which is indicative of largely diamagnetic material diluting the magnetic signal. All three cores, however, share a similar trend of slightly increasing χ values in the lower parts of the cores, followed by a decrease toward the tops. Maximum values are found in G13/3, where at one point a positive value is almost reached. On the other hand, the minima occur in the topmost few centimetres, with χ values around -10^{-8} $\text{m}^3\cdot\text{kg}^{-1}$. Such extremely low χ stems from high water and organic matter content in the measured sediments, and also because of primarily calcareous bedrock. Such environment provides few sources of titano-magnetites (which is supported by very negligible detection of Ti by XRF spectrometry), and carriers of magnetic signal in general (Thompson and Oldfield 1986).

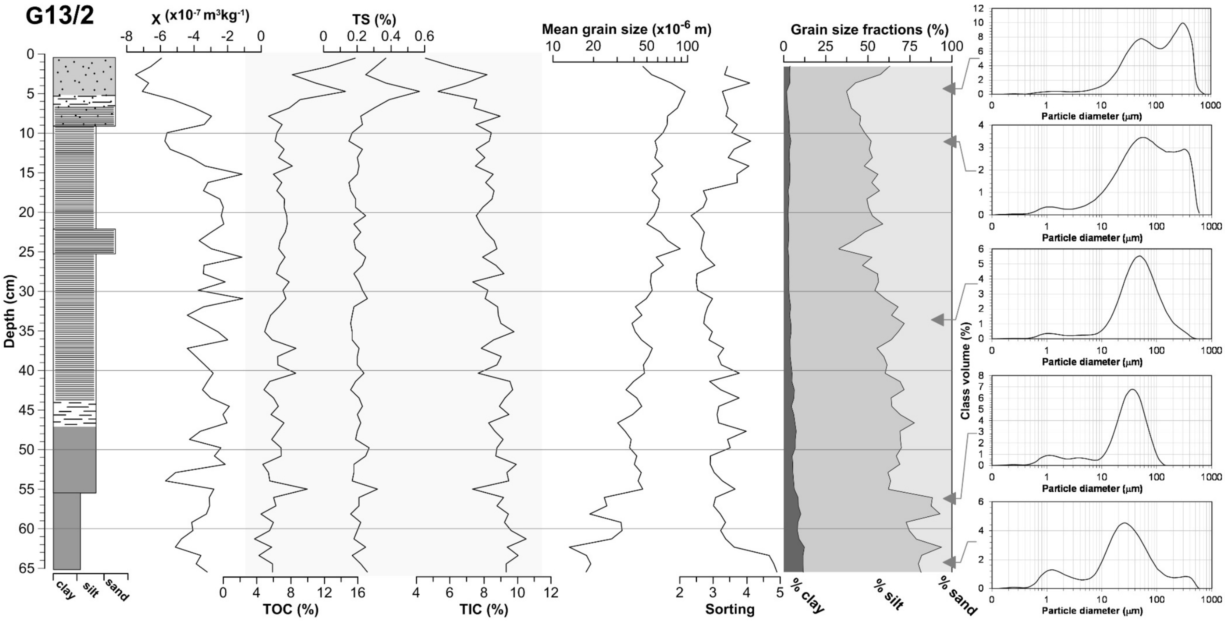

Figure 5.2 Lithostratigraphic description, magnetic susceptibility, organic geochemical proxies (TOC, TIC, TS), and grain size parameters of G13/2: mean grain size in µm, sorting (higher values indicate poorer sorting, i.e. wider range of grain sizes), proportion of grain size fractions and frequency curves of grain size distributions from five selected samples.

Grain size analysis was performed on subsamples from the core G13/2. Care should be taken when interpreting the topmost four measurements for which little material was available. Nevertheless, the grain size variations suggest a clear coarsening trend throughout the core with several fluctuations, most notably in the topmost 4 cm (Fig. 5.2). Sediment is characterized as sandy silt, although at two occasions (depths 25–22 cm and 9–3 cm) extends to silty sand. The mean grain size (MGS) is controlled primarily by the ratio of sand to silt, but content of clay plays an important role as well, and gradual decline of silt and clay cause a steady rise of MGS. Below 55 cm, where MGS drops to 13.2 µm, clay constitutes up to 12.4 % of sediment. On the other hand, MGS reaches the maximum of 96 µm at 5 cm. Distribution is mostly unimodal, although hints of bi- and trimodality appear in several samples, especially in those with excess of clay particles. Sediment is poorly sorted, the depths below 63 cm and above 15 cm particularly so. The whole particle-size profile is negatively skewed, expressing the excess of coarser fraction, and leptokurtic, i.e. with better sorted central portion of the distribution than at the tails. General trend of skewness and kurtosis, however, leads to more symmetrical and platykurtic distribution, respectively. While skewness and kurtosis depend chiefly on relative proportion of sand and silt (correlation coefficients in the range 0.65–0.76), sorting, conversely, reflects primarily the clay content ($r = 0.59$). Both sorting and polymodality point to input of material from multiple different sources.

V.1.3 Geochemical proxies

Measurement of TOC, TIC and TS was performed for all three cores, while XRF was measured in core G13/1 and majority of (i.e. all available) samples from G13/3. Content of organic carbon exhibits a similar trend across all three cores, with values fluctuating around 5 % throughout most of the profiles before increasing to 10–15 % in the uppermost 5–10 cm (Figures 5.2, 5.3, 5.4). Apart from that, several TOC spikes occur in deeper parts of the

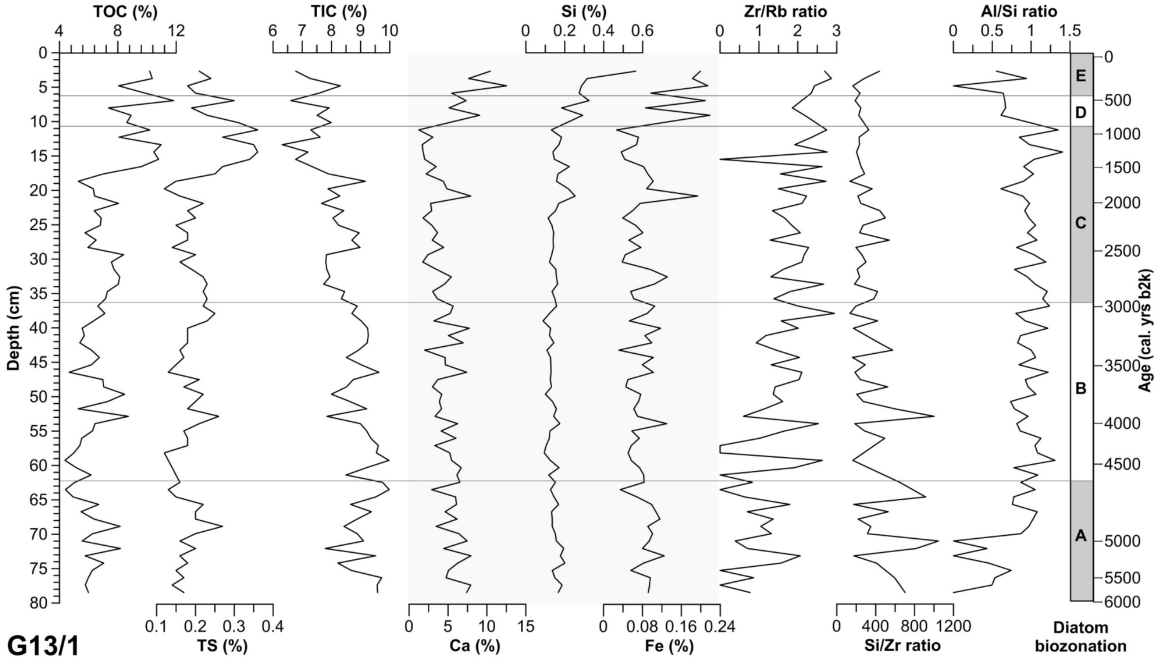

Figure 5.3 Geochemical proxies in G13/1. From left to right: total organic carbon, sulphur and inorganic carbon, content of XRF-detected elements calcium, silicon and iron, and element ratios Zr/Rb, Si/Zr and Al/Si. Chemical composition is expressed as weight ratio (in percent).

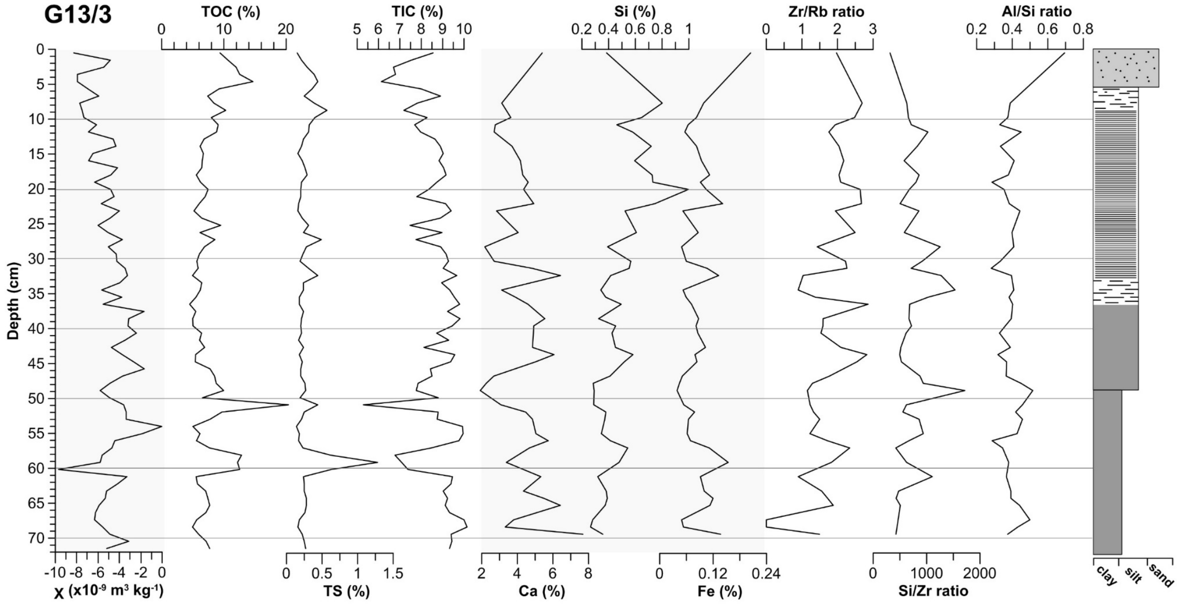

Figure 5.4 Measured parameters and litostratigraphical log for G13/3. Geochemical proxies as in Fig. 5.3.

records, such as a prominent peak at 51 cm in G13/3. Sulphur content (TS) ranges in the interval 0.1–0.5 % and its changes closely follow the TOC variations ($r = 0.81$ for G13/1 and G13/2, $r = 0.56$ for G13/3). A notable exception appears again in the lower part of G13/3, where the most distinct peak of TS reaches 1.3 %. Inorganic carbon content is inversely proportional to TOC (correlation coefficients range from –0.92 to –0.94), but attains similar absolute values, i.e. in the range 5–10 %. Total carbon therefore seems to be come roughly equally from both organic matter and inorganic sources, here carbonate bedrock, although especially towards the top biogenic origin predominates.

XRF spectrometry provided high signal to noise ratio for the elements Si, Cl, K, Ca, Fe, and continuously detected also Al, Rb, Sr and Zr. All elements strongly covary because of high proportion of light elements (with atomic number <13), exacerbating thus the matrix effect, which states that if light elements (LE) increase, all other elements decline correspondingly, and vice versa. Nonetheless, several features are noticeable in both profiles. Calcium is evidently the most abundant element, constitutes around 4.2 and 4.9 % of the sedimentary matter in cores G13/1 and G13/3, respectively. Along with substantial TIC content this points to a significant source of calcium carbonate in the catchment (even though this association is supported only by weak positive correlations of Ca and TIC, in G13/3 significant at 0.05 level). Silicon content varies from 0.1 to 1 % and is most closely related to Al. Iron content keeps below 0.2 %, yet is well representative of other lithogenic elements K, Rb, Ti and Zr, with which it is significantly correlated (Table X in Apendix?). Fe profile markedly resembles also that of Ca, albeit their correlations are slightly lower (yet still significant in G13/1).

When comparing the profiles of Ca, Si, Fe as well as other elements, a lack of agreement between G13/1 and G13/3 is readily noticeable. The matrix effect and highly variable water circumvent these issues and to allow comparison of the cores, effort was made to find concurrence of element ratios in both profiles. Zr/Rb ratio is an example of a comparable proxy, as it displays a steady increase in both cores. On the other hand, frequently used proxy ratios Si/Zr and Al/Si exhibit seemingly no common signal or even inverse behaviour. Reasons behind this discrepancy and meaning of these and other ratios, bearing environmental implications, will be discussed in section VI.2.1.

V.2 Jarfjorden lakes, NE Norway

Two sedimentary cores, out of total seven cores retrieved during the field campaign to Jarfjorden area in 2014, were subjected to thorough palaeolimnological investigation. Results of dating and measurements of physical and geochemical parameters of profiles KH2, cored in Holmvatnet, and KL1, from Langvatnet, are presented here.

V.2.1 Lithostratigraphy and chronology

Cores KH2 and KL1 are composed of silty gyttja of rather homogeneous fine-grained texture. Visually, the colour was the feature changing with the depth most distinctly. Generally, KH2 has grey brown colour, except for depths 21–22 cm, 14–16 cm and 5–8 cm, where the sediment shifts to ochre or reddish-brown colour. Depth 12–14 cm is characterised by lighter shade of grey brown, while the topmost 10 cm is much darker grey brown. Core KH2 was originally 38 cm long, but was compressed due to manipulation during cutting to 36.5 cm. Core KL1 displays more uniform grey brown colouring throughout the profile except a shift to ochre brown at depth 6.5–9 cm. Original length of KL1 was 40 cm, no compression occurred. No marks of laminations nor sudden transitions between units were encountered during cutting, implying a continuous, uninterrupted accumulation under consistent conditions.

In total nine AMS ^{14}C dates revealed a long history of Jarfjorden lakes, spanning the Middle and Late Holocene. Results of radiocarbon dating and calibrated ages are reported in Table 5.2. Due to the lack of macroscopically detectable organic remains, bulk samples were dated, despite the recognised concerns and uncertainties this method involves, such as reservoir effect and multiple carbon sources (Abbott and Stafford 1996). However, both profiles display a chronostratigraphically plausible and consistent results, with only minor

Table 5.2 Results of AMS ^{14}C dating of bulk samples from cores KH2 (Holmvatnet) and KL1 (Langvatnet).

Sample	Laboratory number	Depth (cm)	mg C	^{14}C yrs BP	cal. b2k (± 2 σ)	Min-Max age cal. b2k (± 2 σ)
KH2/57	Poz-78520	8.59	0.09	1980 ± 50	1985 ± 118	1871-2106
KH2/46	Poz-82050	14.32	0.6	3865 ± 30	4351 ± 130	4240-4462
KH2/35	Poz-78521	20.04	0.05	3810 ± 70	4262 ± 222	4039-4465
KH2/21	Poz-82049	27.33	>1	4940 ± 35	5717 ± 86	5650-5785
KH2/6	Poz-82047	35.14	>1	6370 ± 40	7365 ± 106	7232-7470
KL1/65	Poz-82021	7.75	0.3	1480 ± 30	1415 ± 68	1355-1462
KL1/49	Poz-78519	15.75	0.03	3230 ± 70	3513 ± 160	3316-3682
KL1/26	Poz-78518	27.25	0.2	4060 ± 40	4617 ± 198	4475-4851
KL1/7	Poz-82020	36.75	>1	4935 ± 35	5712 ± 82	5649-5780

variations in accumulation rate and no age reversals. The exception is found in KH2, where two samples from depths 14 and 20 cm exhibit the same age ~4.3 ka b2k. This inconsistency might be explained by instantaneous sedimentation, although neither lithology nor proxies display any sign of slumping or bioturbation. More likely, the overlapping ages are caused by large standard deviations of both reported and calibrated ages; sample KH2/35 in particular yielded only 0.05 mg of C for dating, and was thus excluded from the final age-depth model as less reliable of the two. Using the upper date from 14 cm in KH2 also ensures that the two independent age-depth models of KH2 and KL1 share a very similar trend of accumulation rate, with somewhat slower deposition occurring after 3.5–4.5 ka b2k and reflecting thus probably a regional signal. To conclude, bulk radiocarbon dating of Jarfjorden lacustrine sediments seems credible, considering also few possibilities of incorporating 'old', ^{14}C-depleted carbon into the sediments, and the comparability of the results from independently dated samples from KH2 and KL1.

Very convincing results were obtained also from dating by short-lived radionuclides. Although no distinctive peaks of ^{137}Cs were detected, specific activity of ^{210}Pb exhibits a clear drop in the upper 2.5 cm (insets in Fig. 5.4 and 5.5), to form subsequently an equilibrium with ^{226}Ra. Unsupported ^{210}Pb thus enables to estimate age of the upper 2–3 cm to ~150 years b2k. The results also mean that the entire cores were retrieved, including the sediment-water interface, and that accumulation rates increased approximately fourfold near the top, from the mean rate ~0.05 mm·yr^{-1} to ~0.2 mm·yr^{-1}. Again, different degree of sediment compaction and saturation by water cloes to the sediment-water interface may result in this apparent acceleration of sedimentation.

Age-depth modelling suggests that the profile KH2 spans the last ~8 ka (curve fit = 11.48 in Clam software, KH2/35 designated as an outlier; Blaauw 2010). Especially in the lower part of the core, relatively good precision was achieved, since 2σ uncertainty reaches only around 150–250 yrs. Extremely low accumulation rate 0.05 mm·yr^{-1} increased only between 5.7 and 4.4 ka b2k to ~0.1 mm·yr^{-1} and then near the top. Core KL1 covers the last ~6 ka (curve fit = 5.89). A comparable drop in accumulation rate as in KH2 is observed, although it occurrs later at ~3.5 ka b2k.

V.2.2 Physical proxies

Trend of magnetic susceptibility is very similar in both records, even though absolute values are higher in KL1 by about one order of magnitude. In the lower 30 cm of KL1, χ keeps below 10·10^{-7} m^{3}·kg^{-}1 but then increases in a double peak to 30·10^{-7} m^{3}·kg^{-1}. In KH2, χ

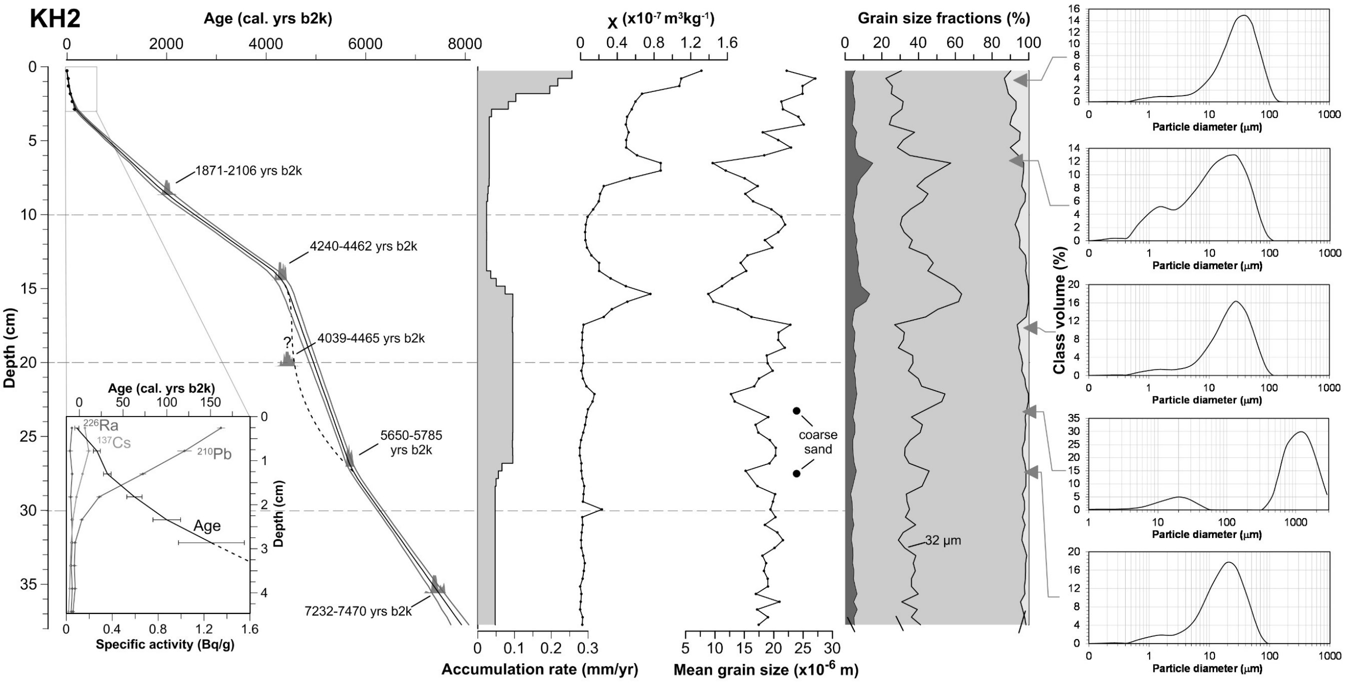

Figure 5.5 Age-depth model, magnetic susceptibility and grain size parameters of the profile KH2.

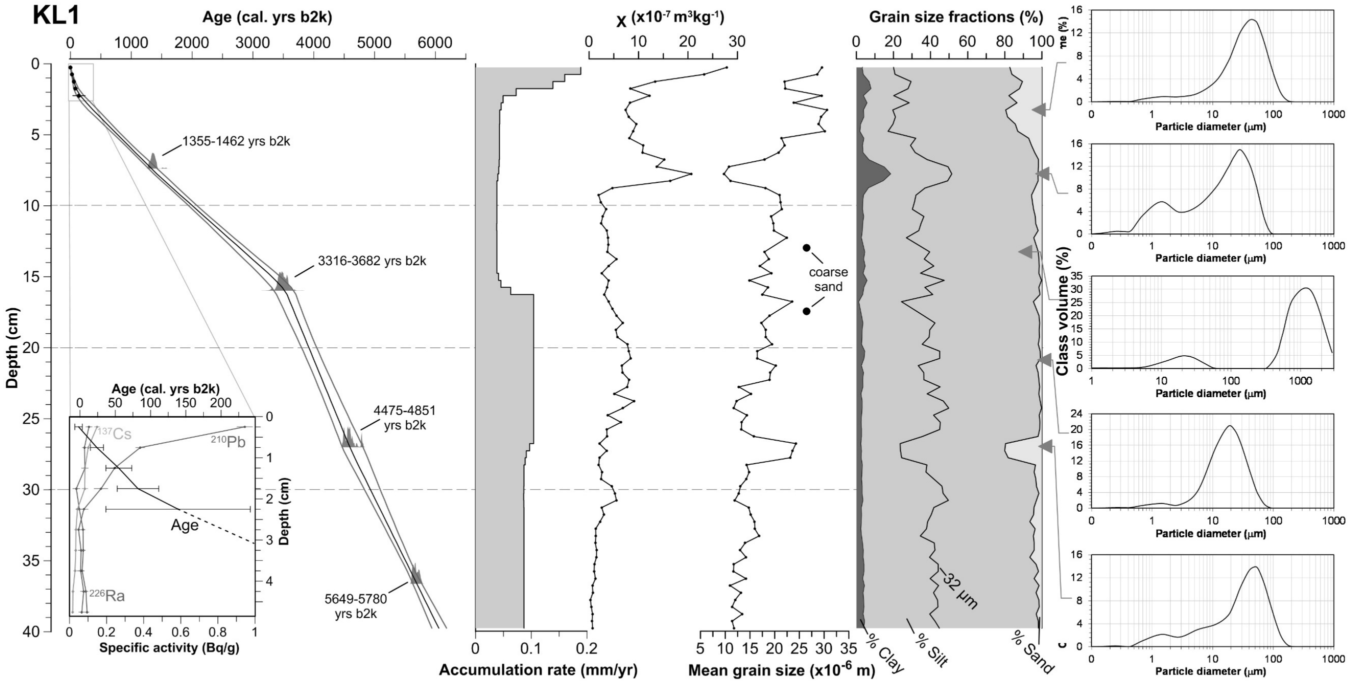

Figure 5.6 Age-depth model, magnetic susceptibility and grain size parameters of the profile KL1.

averages only at $0.2 \cdot 10^{-7}$ $\text{m}^3 \cdot \text{kg}^{-}1$ below 17 cm, but then increases in peaks at 15, 6 and 0.5 cm to $1.4 \cdot 10^{-7}$ $\text{m}^3 \cdot \text{kg}^{-1}$. Higher frequencies of magnetic susceptibility χ_{F2} and χ_{F3} follow closely the low-frequency χ. However, when expressed as χ_{FD}, a very large scatter of the data (sometimes hundreds of percent, undeniably higher than naturally occurring values 0–15 %) discredits the samples with χ values lower than $\sim 0.5 \cdot 10^{-7}$ $\text{m}^3 \cdot \text{kg}^{-1}$. Nonetheless, there is a perceptible signal in the upper parts of the cores with generally higher χ. χ_{FD} reaches on

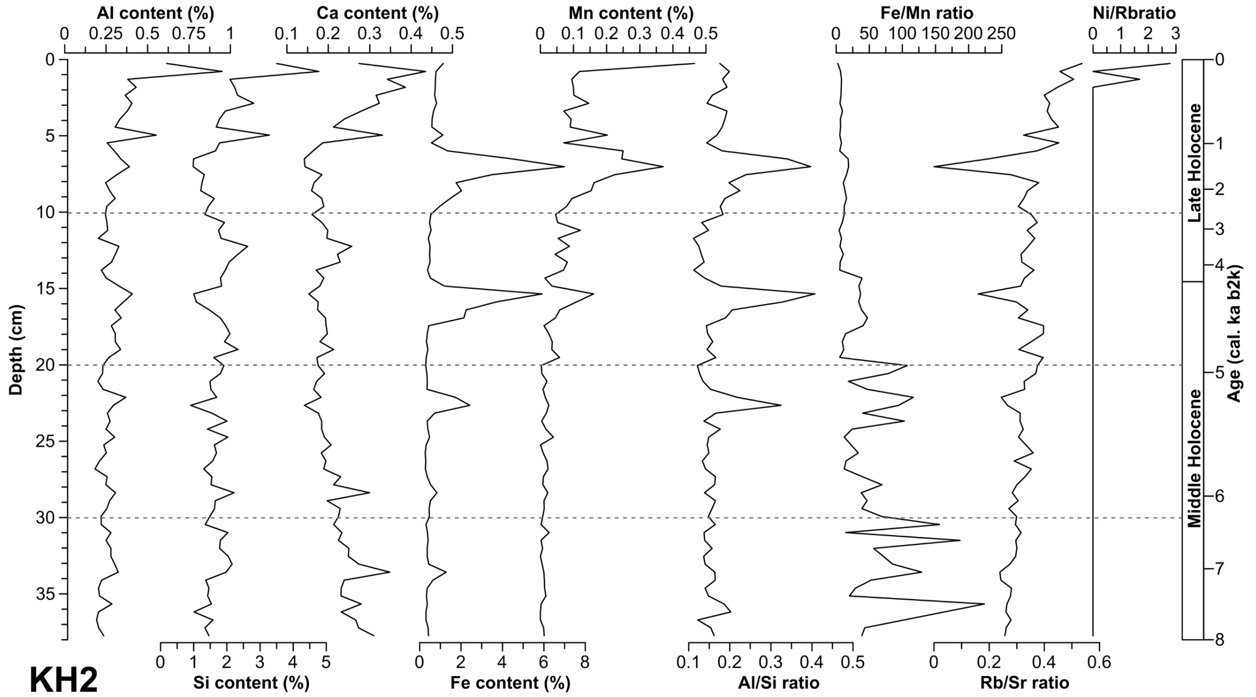

Figure 5.7 XRF geochemical proxy data of selected elements and their ratios in core KH2 (Holmvatnet).

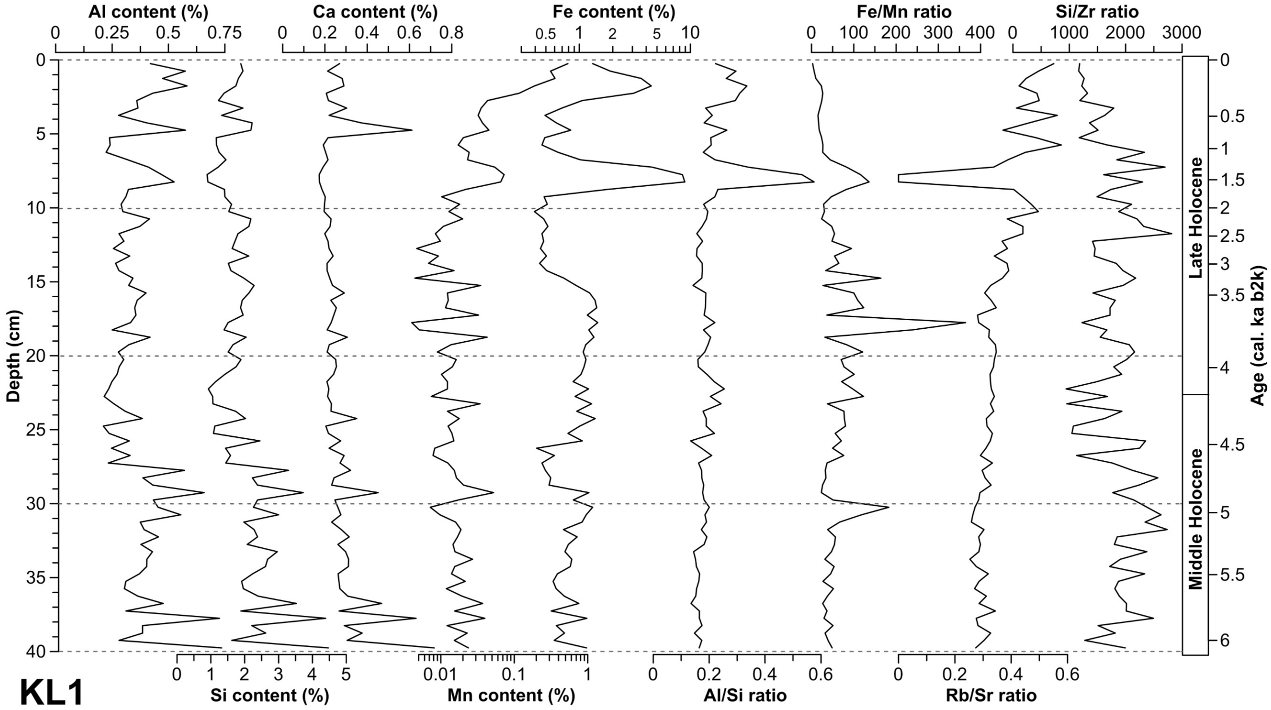

Figure 5.8 XRF geochemical proxy data of selected elements and their ratios in core KL1 (Langvatnet).

average 5 % in KH2 (above 15 cm), whereas in KL1 χ_{FD} reaches 2 % (depths 10–30 cm) before rising to 4 % (depth 10 cm and above). Due to great variability, χ_{FD} is not considered further in principal component analysis.

Grain size variations in the two cores share many similarities as well. The most notable feature is conspicuous fining of the material associated with increases in χ (Fig. 5.5

and 5.6). Texture of the sediment can be characterised as silt or, if sand content exceeds 10 %, as sandy silt. Fine and medium sand is present mainly in the upper 5 cm in both cores. Besides, in two layers in each core, high proportion of medium to very coarse sand was observed in the form of several distinct sand grains. Since these samples highly distort grain size characteristics, they are unaccounted for in calculation of MGS and fractions, and they are displayed in the graphs (Fig. 5.4 and 5.6) only as symbol notation and frequency histogram of particle size. These sandy layers occur at 23 and 28 cm in KH2 and at 13 and 17 cm in KL1. The samples are markedly bimodal, and fine-grained portion of these samples correspond to the character of adjacent silty samples. Clay content reaching up to 20 % is present at depth 15 and 6 cm in KH2 and at 7 cm in KL1. MGS ranges from 10 to 30 μm in both cores. The coarsening trend apparent in MGS rise in the lowermost 15 cm of the core KL1 should be treated cautiously, because ultra-fine particles (<0.5 μm) may have biased the measurement as they were ineffectively washed out from the laser granulometer. The sediment of KH2 and KL1 is mostly poorly sorted, leptokurtic and with excess of coarse particles. Polymodality is present in samples with increased clay content.

V.2.3 Geochemical proxies

Elements with high signal to noise ratio acquired by XRF spectrometry in cores KH2 and KL1 are Al, Si, S, Cl, K, Ca, Mn, Fe, Zn, Rb, Sr and Zr. Content of light elements was rather high (86–95 %) and was inversely proportional to absolute values of majority of lithogenic elements. Of these, the most abundant elements in both cores, that significantly mutually covary (Tables 9.4 and 9.5 in Appendix), are Si (mean content 1.8 %), Al (0.33 %), Ca (0.24 %) and K (0.16 %). To the contrary, Fe (1.1 %) and Mn (0.05 %) display clearly different behaviour and significantly correlate with χ, clay content and Al/Si ratio rather than with other elements. Elements Rb, Sr and Zr reach very low concentrations (mere units of parts per million), but are consistently present throughout the profiles with clear long-term trends, especially when expressed in ratios such as Rb/Sr.

In KH2, elevated content of Al, Si, Ca and other lithogenic elements occurs in the upper 5 cm (Fig. 5.7 and 5.8). Al and Si content in the lower parts of the core is rather stable, but Ca and Zr on the contrary continually decrease towards their minima at 7 cm. In KL1, the most prominent peaks of Al, Si and Ca are found below 37 cm and at 27–32 cm, although in the top 5 cm content of lithogenic elements, in particular Al, Rb and Zr, increases again. Peaks of Fe content coincide with χ and clay content maxima in both cores, i.e. at depths 22, 15 and 6 cm in KH2, and 8 and 1.5 cm in KL1. Manganese partly reflects the peaks of Fe, but the overall trend is that of increasing Mn content throughout the profiles, especially towards the topmost sample, reaching thus maximum values (~0.5 %) in both cores.

Trend of Al/Si ratio closely follows that of Fe content in both profiles. In KH2, Fe/Mn ratio markedly fluctuates below 20 cm depth, but then attains very low values in the upper part of the core. Profile KL1, on the other hand, exhibits high values of Fe/Mn in the middle part of the core, namely the peak at 18 cm. Rb/Sr ratio display remarkably similar trends in respective cores, rising continuously from ~0.3 near the bottom to ~0.6 in the top, however, with a prominent drop at 7 and 8 cm in KH2 and KL1, respectively. The only occurrence of Ni is in the topmost 1.5 cm of the profile KH2, expressed as Ni/Rb ratio in Fig. 5.7. Cu/Rb ratio peaks in the upper samples of KH2 as well, but elevated values are located also below 18 cm. Nickel was not detected in KL1, and Cu/Rb ratio on the contrary reaches the highest values in the lowermost samples. Two wide zones of elevated Si/Zr ratio appear at 7–12 and 27–35 cm in KL1. Most significant increases in Si/Zr ratio in core KH2 occur between 15 and 27 cm and at depth of 6 cm.

V.3 Kobbefjord, SW Greenland

V.3.1 Lithostratigraphy and chronology

Both sediment cores consist of homogeneous dark brown silt to sandy mud and gyttja with high content of minerogenic material. Only upper 5 cm in both cores exhibit perceptible increase in organic matter such as undecomposed mosses and rarely leaf fragments, but nonetheless lithostratigraphic units were not identified. Instead, we use biozonation based on cluster analysis of diatom species data (see above) when presenting stratigraphy of core L4. Five zones 1–5 were defined, with further subdivision of Zones 2 and 4 into subzones a and b. Boundaries of the main Zones 1–5, ordered from the bottom to top, are placed at the depths of 53, 34.5, 26 and 6 cm, respectively. Detailed description of diatom biozones will be given further in the section Diatom stratigraphy.

Four AMS ^{14}C dates were obtained in both cores and together with calibrated ages are presented in Table 1. In order to avoid age reversals, one date in each core was designated as an outlier and thus has not been incorporated into age-depth models. In core L4 the topmost ^{14}C-dated sample (L4/75) exhibited modern carbon content and thus was excluded as an outlier, even though calibrated age fits well into age-depth model. Age of an L3 outlier (L3/75) was derived from a terrestrial plant macrofossil found in the lowermost layer (excluding mixed 3 cm of the core's base) and thus is probably a result of sediment reworking or contamination caused by coring.

Short-lived radioisotope dating has shown that the topmost layers were well preserved and cored undisturbed. Measured specific activity of radionuclides and calculated age is depicted in Fig. 2. The ^{210}Pb profile in core L4 steadily declines to the limit at 4.5 cm and adequately corresponds to the expected model of exponential decay of unsupported ^{210}Pb. Increased concentration of ^{137}Cs is found at 3 cm. Core L3 exhibits a rather chaotic

Table 5.3 Results of AMS ^{14}C dating of terrestrial macroremains from infilled lakes L4 and L3 in Kobbefjord.

Sample	Laboratory number	Depth (cm)	mg C	^{14}C yrs BP	cal. b2k (± 2 σ)	Min-Max age cal. B2k (± 2 σ)
L3/19	Poz-72545	9.25	0.12	180 ± 35	211 ± 178	50–351
L3/40	Poz-65686	19.75	0.2	440 ± 90	506 ± 184	352–691
L3/64	Poz-72546	31.75	0.17	530 ± 30	603 ± 70	560–681
L3/75	Poz-65684	37.25	>1	315 ±30	434 ± 93	352–516
L4/75	Poz-65687	16.6	0.1	101.04 ± 1.42 pMC	187 ± 144	43–330
L4/64	Poz-72549	23.01	0.13	60 ± 40	173 ± 156	72–316
L4/45	Poz-72548	34.08	0.7	150 ± 30	200 ± 168	50–334
L4/22	Poz-72547	47.48	0.19	390 ± 30	487 ± 119	370–560
L4/1	Poz-65685	59.71	0.1	780 ± 140	797 ± 240	585–1013

profile of ^{210}Pb, suggesting changes in sedimentation rate (as CRS model was used) might have taken place here. By analogy, variable influx of short-lived radioisotopes from the upper catchment of L4 could affect ^{210}Pb concentrations downstream. Roughly exponential curve of decrease in ^{210}Pb activity, however, enables to detect convergence of unsupported and supported ^{210}Pb slightly below 4 cm in the core and estimate the sediment age. Profiles of ^{137}Cs and ^{226}Ra lack any noteworthy features usable for dating.

Based on extrapolation of the best-estimate age-depth model (curve fit = 10.69 in Clam software) core L4 extends to 775 cal. yr BP with 2σ uncertainty interval 544–979 cal. yrs BP (Fig. 2). At the beginning the accumulation was relatively slow (0.4 mm yr^{-1}), but steadily accelerated up to 3 mm yr^{-1} in the upper 20 cm. At 4 cm there is a sudden drop of accumulation rate to 0.2 mm yr^{-1} that, however, probably stems from linking two core segments with different dating methods. Accumulation rate then nearly recovers to preceding high values. In core L3 modelled age of the lowermost sample is 635 cal. yr BP with 2σ interval 532–799 cal. yr BP. Accumulation rate on the order of ~1 mm yr^{-1} or less throughout most of the core matches common sedimentation rates observed in Polar regions. Near the core's top the accumulation rate rises steeply to >4 mm yr^{-1}.

V.3.2 Magnetic susceptibility and grain size

Majority of samples in both cores exhibit χ values higher than $1 \cdot 10^{-7}$ m^3·kg^{-1}, revealing thus certain content of ferromagnetic minerals. Lower χ values, characteristic for paramagnetic and diamagnetic materials, are linked to increased organic content. This is well supported by negative correlations with TC ($r = -0.41$ and $r = -0.76$ for cores L4 and L3, respectively; Table S1a and S1b). In core L4 χ reaches constant values in depths between 58 and 15 cm, although mean χ is slightly higher and more variable than in core L3 (Fig. 2). The highest values exceeding $1 \cdot 10^{-6}$ m^3·kg^{-1} are found in the sandy base of core L4 and at 12 cm depth in Zone 4b. Near the core's top, in Zone 5, χ decreases most strikingly. This drop is also reflected in increase of TC and TN content, as well as in mean grain size (MGS). The lowest χ values in core L3 occur in the uppermost 3.5 cm and at depths of 7 and 17–19 cm. All these sections correspond to the peaks of C and N content. Maximum of χ in core L3 occurs close to the core's top at 4.75 cm, interrupting the general trend of χ decline throughout the core.

Fluctuations in grain size are well pronounced in both cores. Sediment of core L4 is poorly sorted and has generally unimodal distribution, although fine-grained units in Zone 2b are partly bimodal. Throughout most of the core, the sediment is characterized as sandy silt to silty sand with MGS ranging from 11 to 80 µm, excluding the topmost sample that

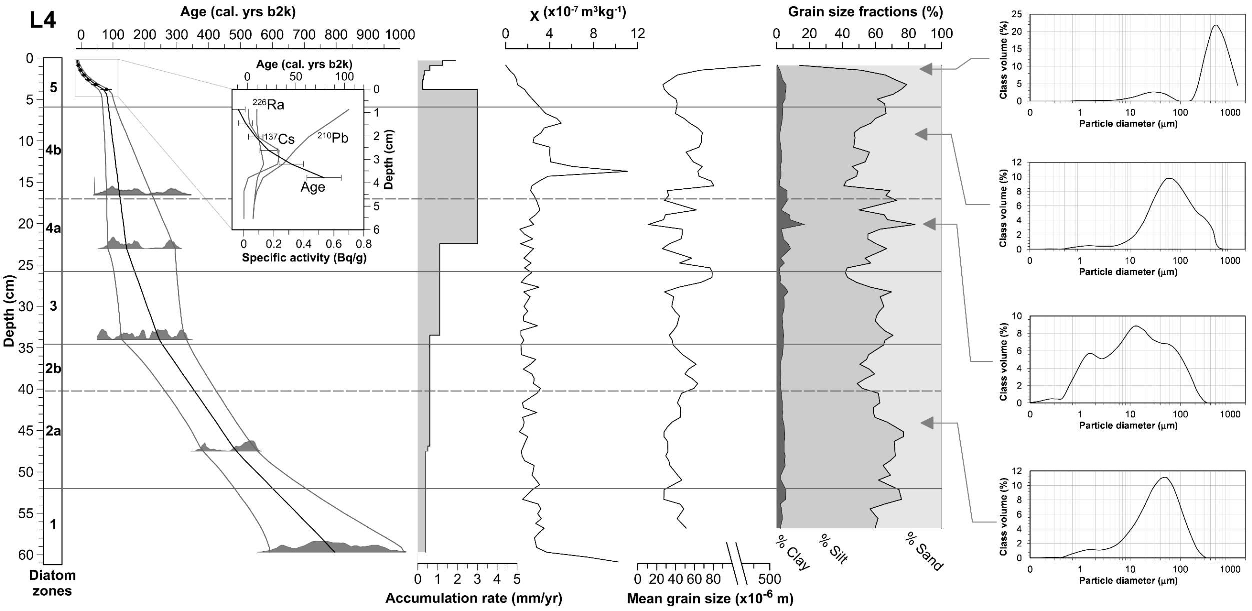

Figure 5.9 Age-depth models of core L4. Desciption see below.

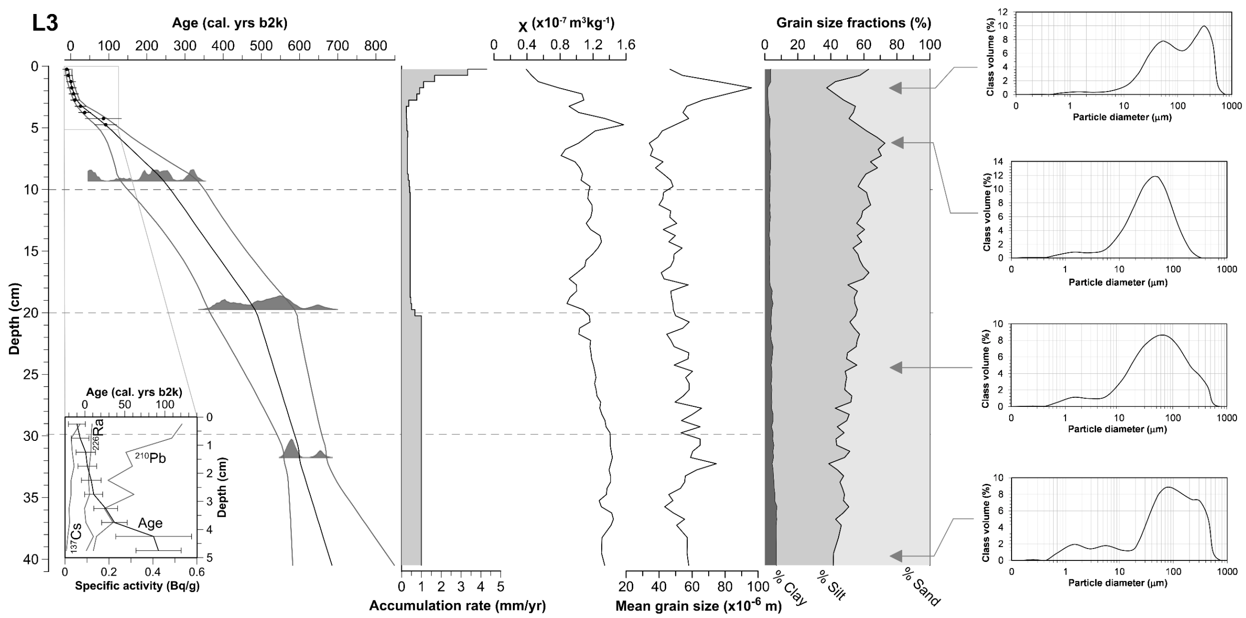

Figure 5.10 Age-depth models of cores L3 based on AMS ^{14}C (grey plots of probability distribution) and short-lived radioisotopes (rectangular insets) dating; best fit model is denoted by black line with 2σ (grey lines on the sides). Also shown are accumulation rate, mass-specific magnetic susceptibility χ and grain size variations.

reaches 460 μm and sand constitutes over 80 % (this sample, however, needs to be treated with caution because of elevated organic content and on the contrary low quantity of material available for grain size measurement). Clay fraction is scantly represented, only in Zone 4b, period of increased variability of grain size, there is a sharp peak of clay content reaching almost 20 % (Fig. 2). χ does not correlate with MGS significantly ($r = -0.13$), although it shows certain degree of correlation with sand ($r = 0.2, p < 0.05$) and silt ($r = -0.2, p < 0.05$). Sediment of core L3 is poorly sorted and in the upper half of mostly unimodal distribution.

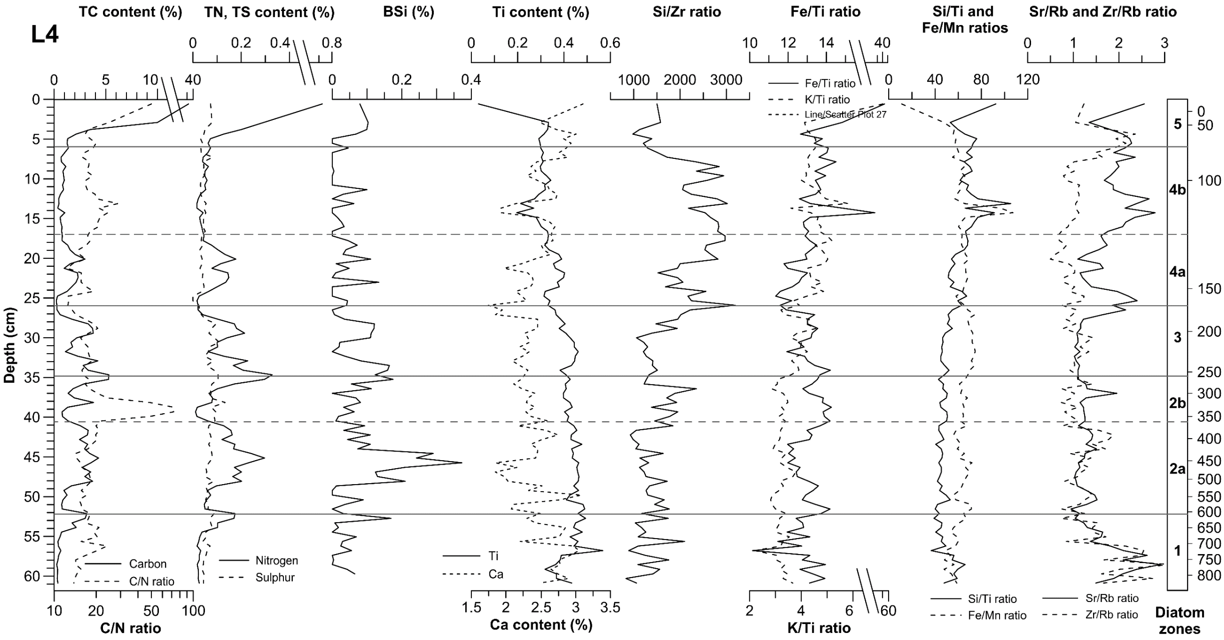

Figure 5.11 Variations in geochemical proxies in cores L4 plotted against depth and calibrated age scale. Diatom biozonation is shown on the right hand side of the plot.

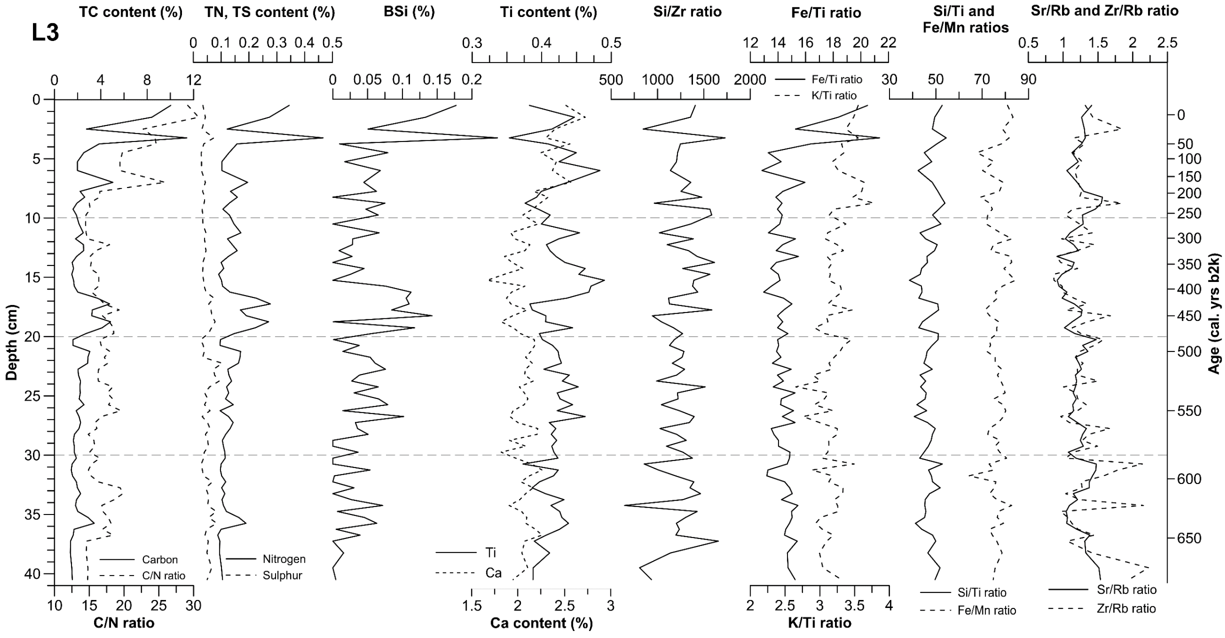

Figure 5.12 Variations in geochemical proxies in core L3.

Near the base, however, bimodal or even trimodal distribution dominates the record. There is a gradual decrease in MGS interrupted only by a peak at 2 cm. The variations in the MGS mainly reflect the sand to silt ratio, whereas clay content is relatively constant, although also declines from ~7 to ~3 %. The MGS follows both gradual decrease and a sudden peak of χ in the upper layers, even though the variables are not significantly correlated (r = 0.13) and the peak of MGS lags that of χ. However, χ in core L3 correlates strongly to grain-size fractions, i.e. positively to sand (r = 0.46) and clay (r = 0.52), and negatively to silt (r = –0.50).

V.3.3 Geochemical proxies

Analysis of elements predominantly constituting organic matter (considering the local bedrock, TC should be largely of organic origin) revealed a similar pattern in both cores (Fig. 5.4): after a prolonged period of low accumulation of TC, TN and TS, a sudden increase of TC and TN subsequently takes place in the top 5 cm, i.e. the last ~50 years, in both cores. Disparity, however, exists in the magnitude of this rise. Whereas average TC content in core L4 reaches 0.3–5 %, which later rises to 36 %, TC content in core L3 increases from 1–5 % to 12 % only. Total sulphur content follows to some extent the fluctuations of TC and TN for most of the cores, but conspicuously no increase is observed toward the tops of both cores. In core L4, main TC and TN maxima besides that in core's topmost Zone 5 are located at the boundaries of Zones 1–2a and 2b–3, while lowest values appear throughout the Zone 4b. The C/N ratio is quite variable, but the values ranging from 13 to 24 for the major part of the core indicate mixed to terrestrial source of organic matter. At the top, the C/N ratio rises to ~50, while an even more prominent peak (C/N = ~70) is found at 32 cm (Zone 2b), where the TN content falls almost to zero. Enhanced proportion of terrigenous organic matter is also found in Zone 4b (C/N = ~29). In core L3 the C/N ratio reaches 14–18 before rising to ~30 near the core's top. Biogenic silica reaches highest values 0.4 % and 0.24 % in Zone 2a inL4 and in the top 5 cm in L3. Otherwise, BSi oscillates between 0 and 0.1 % throughout the both profiles except slight increase at 20–16 cm in L3.

Consecutive data with high signal to noise ratio were acquired for elements Al, Si, P, K, Ca, Mn, Fe, Cu, Zn, Rb, Sr, Zr and Pb. Selected elements and their ratios, most relevant to extraction of environmental information, are shown in Fig. 3 (besides P also Ca and ratios Si/Zr, Fe/Ti, K/Ti, Si/Ti, Fe/Mn, Sr/Rb and Zr/Rb). PCA on aggregated elemental concentration of both cores (Fig. S2) reveals negative correlation on PC1 between C, N, S, P and Al, Si and Sr. Another distinct group of elements on PC2 axis comprises Fe, Rb, Ti and Zr. Potassium and Ca explain little variability in the PCA. Calcium content in both cores averages at 2–3 % and its profiles show a slight rise towards the top (the last ~200years). Core L4 records higher Ca content also in Zones 1 and 2a. Titanium content has a decreasing tendency in core L4, while in core L3 oscillates around 0.4 %, with larger deviations appearing in the upper half of the core.

Grain size variations can be inferred from elemental ratios, considering the propensity of some elements to occur in certain grain fraction. Silicon is typically found in sand fraction, Zr and Sr are often enriched in coarse silts to sands, Ti in silts generally, and finally Al, K, Rb and Fe in clays (Davies et al. 2015). Some of these findings are reflected in correlations of elements with grain-size fractions also in our data, e.g. K and Al correlates with clay ($r = 0.47$ and $r = 0.57$) or Ti and Zr with silt ($r = 0.48$ and $r = 0.51$) in core L4. Remarkably, no similar significant correlations are observed for sand fraction, and thus are the aforementioned assertions supported only by the lack of negative correlations of several elements with sand, e.g. Si ($r = 0.03$, p < 0.75) and Sr ($r = 0.2$, p < 0.06) in core L4, and Zr ($r = 0.18$, $p < 0.13$) in core L3. Some ratios commonly associated with coarser grain sizes, such as Fe/Ti or Zr/K, do not correspond to MGS in our data. The strongest correlation with the MGS is exhibited by the Sr/Rb ratio ($r = 0.57$ in core L4 and $r = 0.29$, $p < 0.014$ in core L3). Sr/Rb attains high values (~2–2.5) in Zones 1 and 4b and at the boundary of Zones 3–4a in core L4. In core L3, the Sr/Rb varies little. Also Zr/Rb partly reflects MGS variations in core L3 ($r = 0.3$), while in core L4 the following ratios are correlated with MGS: Si/Zr ($r = 0.44$), Si/Ti ($r = 0.42$), Al/Si ($r = –0.47$). In both cores Zr/Rb reaches maximum values in lowest and topmost layers (corresponding to Zones 1 and 5 in core L4). Si/Zr follows trends similar to Sr/Rb, but for the Zones 1 and 5 of core L4, where it is significantly lower.

In core L4 the Ti-normalized ratios Fe/Ti, K/Ti and Si/Ti follow a similar trend of gradual increase towards the core's top that is interrupted by two abrupt peaks at 14 cm (K/Ti and Si/Ti slightly lag that of Fe/Ti) and in the topmost sample. Fe/Mn displays a spike at 14 cm as well, but on the contrary dramatically decreases at the core's top from mean values of 50 to 10. In core L3 Si/Ti and Fe/Mn are rather stable throughout the profile, and so are K/Ti until 9 cm and Fe/Ti until 4 cm, where they increase more notably. The Fe/Ti ratio behaves differently in each lake: in core L4 it is positively correlated with χ ($r = 0.48$), while on the contrary in core L3 it correlates negatively ($r = –0.48$) and is clearly bound to organic matter, especially TC ($r = 0.82$).

VI. Discussion

VI.1 Stratigraphic correlation of cores, searching for common (regional, climatic) signal

Abstracting environmental information out of large datasets is not always straightforward, since many proxies will be affected by internal limnologic processes (that are of interest on its own), diagenetic processes differing from core to core, and by other noise in the data (Lowe and Walker 2014). Availability of multiple cores from the same lake or area thus always presents a boon enabling mutual correlation of the cores with the aim to single out the desired conclusive information of universal regional validity and reproducibility (e.g. Snowball and Sandgren 1996, Thompson et al. 2012). Individual dating of each core that is being correlated undoubtedly facilitates finding the stratigraphic correlations, but even without the precise chronology it is possible to link the cores together on a single age scale, as will be shown next. The numerical method of sequence slotting used for the inter-core correlation resembles dendrochronological cross-dating, i.e. matching and ordering of tree-ring series for construction of the master chronology.

VI.1.1 Lake Garmaksla

Three recovered cores were subjected to non-destructive analyses first and then redistributed to other labs for biostratigraphical analyses of diatoms, chironomids and plant macrofossils, the results of which are discussed in the text. Furthermore, only the samples from the 'master' core G13/1 have been dated by AMS ^{14}C method, and the top 10 cm of G13/2 by short-lived radioisotopes. Because a different kind of destructive analysis was performed in each core, the cores must be correlated on the basis of abiotic proxies. Following the lithostratigraphic and chemostratigraphic description of Garmaksla cores (section V.1), the inter-core correlation was established by linking the corresponding layers in each core. Limits of lamination were used as fixed lithostratigraphic tie-points, although due to gradual transitions especially the lower boundary may suffer from the inaccuracy of few cm. The optimal ordering of the stratigraphic data using the abovementioned tie-points and proxies of χ, TC, TS and TC/TS ratio as performed by sequence slotting (Thompson et al. 2012) is shown in Fig. 6.1. These proxies were selected because they were measured in all three cores, although in case of χ and TC their correlations are not obvious immediately. Variable water, carbonate and organic content confounds the magnetic signal (Evans and Heller 2003), and

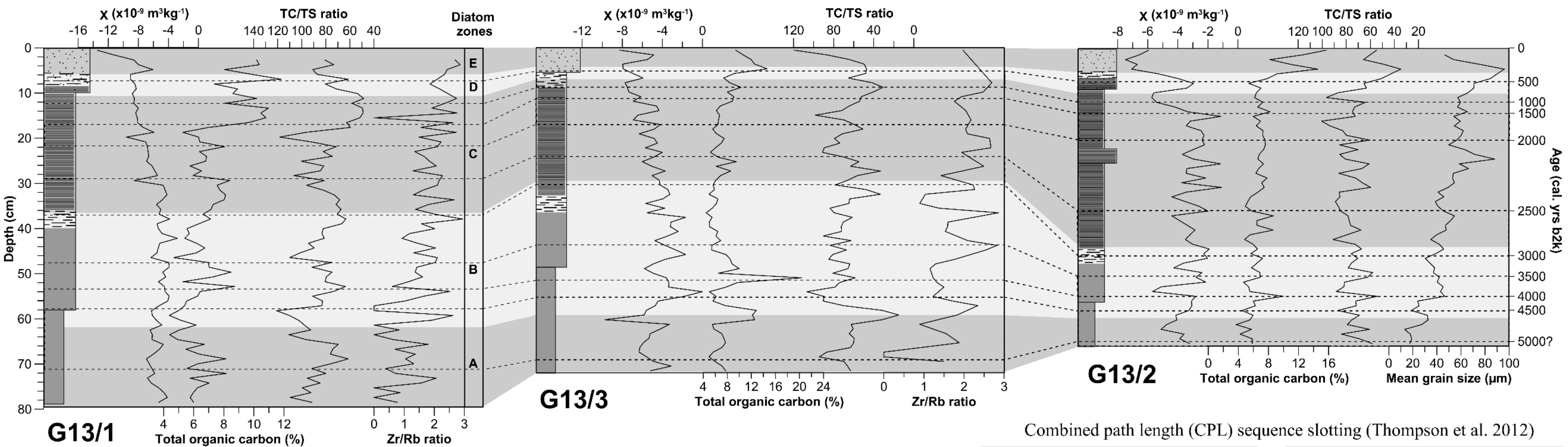

Figure 6.1 Stratigraphic correlation of Garmaksla cores based on lithostratigraphy and selected proxies (above), used to establish the composite age-depth model and assign the age to depths in all three cores. Diatom zones (alternating grey bands) and equivalent ages (dotted lines) shown for all three cores. Correlation is based on sequence slotting (Thompson et al. 2012) with parameters and settings of CPL runs displayed to the right (Table 6.1).

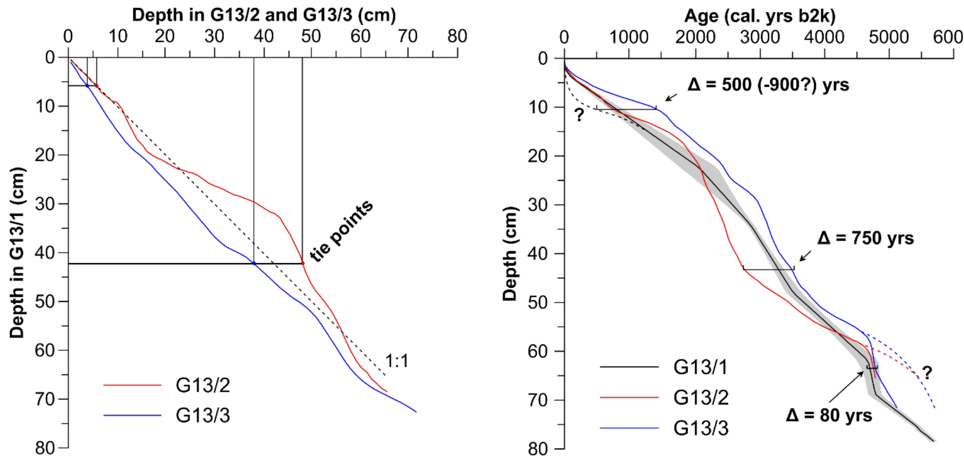

Figure 6.2 Correspondence of depths in G13/1 (y axis) to other two Garmaksla cores (red and blue line), as computed by CPL sequence slotting, with bounadries of laminations used as tie points (left); comparison of age-depth models of individual Garmaksla cores (black, red and blue lines), with highest and lowest age divergence denoted by Δ and with apparent uncertainties (dotted lines) (right).

Combined path length (CPL) sequence slotting (Thompson et al. 2012)

Results G13/1 - G13/2

Sequence A (G13/1) N = 72
Sequence B (G13/2) N = 63
Distance measure used: City-block

Variable:	Weights:
Mag. Susc.	1
TOC	1
TS	0.5
TC/TS ratio	5

total length CPL = 701.49

Seq./Level	A	B as A	PPL
A1	1.0		14.634
A2	2.0		17.599
B4		2.200	26.123
B5		2.403	34.737
A3	3.0		60.151
A4	4.0		64.398
B6		4.568	80.082
B7		4.758	85.319
A5	5.0		92.01
…			…

Results G13/1 - G13/3

Sequence A (G13/1) N = 72
Sequence B (G13/3) N = 70
Distance measure used: City-block

Variable:	Weights:
Mag. Susc.	1
TOC	1
TS	1
TC/TS ratio	5

total length CPL = 637.04

Seq./Level	A	B as A	PPL
A1	1.0		20.158
A2	2.0		23.394
B3		2.424	27.165
A3	3.0		32.284
A4	4.0		36.711
B4		4.653	43.844
A5	5.0		47.630
B5		5.183	49.702
B6		5.470	52.950
…			…

Table 6.1 Results, parameters and settings used for CPL sequence slotting, by which correlation between Garmaksla cores was established (Thompson et al. 2012). Slotting was performed on 4 variables with different assigned weights. Example of ordering for the first few layers shown at the end.

they are primarily bound to organic matter (TOC and TS correlation coefficient around 0.81 in all cores; TOC was replaced by TC due to slightly greater correlations with TS; TOC and TC correlate with $r = 0.95$ and 0.98 in G13/1 and G13/3, respectively,). Unless a certain kind of preferential bacterial utilization of either carbon or sulphur occurred during decomposition (Håkanson and Janson 1983), TC/TS ratio should be similar in the sediments across the lake basin. Therefore, TC/TS ratio was assigned the highest weight in sequence slotting.

Validity of correlation was subsequently checked by comparison of MGS in G13/2 with Zr/Rb ratio in the other two cores. Zr/Rb ratio may serve as a proxy for grain size variations in finer-grained sediment (Kylander et al. 2011). As evident in Fig. 6.1, a coarsening trend is indeed observed in all three cores. Further confirmation can be provided by biostratigraphic data from the considered cores (Pinseel 2014; Vondrák, unpublished data). Analysis of diatom microfossils (Pinseel 2014) identified a significant shift in assemblages at 36 cm in G13/1 where lamination begins. Chironomid assemblage also (although not significantly) changes near the onset of lamination in G13/3 at ~35.5 cm (Vondrák, personal communication). Both transitions mark primarily a shift towards less diverse biological assemblages. Similarly, productivity of both diatoms and chironomids increases significantly in the upper 3–4 cm of their respective cores, close to the upper limit of laminae, and corroborates the validity of correlations.

Establishment of the equivalent layers between the cores enabled to assign age to each depth, based on the composite age-depth model (Figure 6.2). Comparison of the individual age-depth models of each core documents to what degree the models deviate in each layer. The greatest difference of ~750 yrs is observed at 45 cm, whereas at 63 cm the models converge to ~80 yrs. However, due to dissimilarity of proxies and no evident tying points, the shorter cores G13/2 and G13/3 might have not been correctly correlated to G13/1 below 60 cm, so they can actually extend further back into the past. Divergence is also apparent between 5 and 15 cm, exacerbated by the uncertainty of the master age-depth model. According to Pinseel (2014), significant shift of diatom assemblages, interpreted as a response to warming following the end of LIA, occurs already at 11 cm in G13/1. On Svalbard, LIA ended by the end of the 19th or beginning of the 20th century (Guilizzoni et al. 2005, Jiang et al. 2011, Røthe et al. 2015, Balascio et al. 2017), whereas depth of 11 cm corresponds to ~900 yrs b2k in the presented age-depth model. However, this section of core G13/1 between depths suffers from a scarcity of dated samples (only one outlier exhibiting modern carbon content at 7 cm and then a date at 22 cm). Two possible scenarios are therefore at play: i) The age-depth model overestimates the age by several centuries in this section of the core, with transition of the biozones C to D indicating the end of LIA (Pinseel 2014) and boundary of the biozones D and E signifying more recent warming during the 20th century (this would mean accumulation rate must have increased significantly in the upper ~10 cm, and possibly that the ^{14}C dated layer at 7 cm is not an outlier), or ii) the age-depth model is more or less accurate and boundary of biozones D to E represents a response of diatoms to a different driving factor, perhaps non-climatic or local event, and not the LIA termination (which is marked by transition of zones D to E; Pinseel 2014).

VI.1.2 Jarfjorden lakes

Proxy data of the two cores bear several notable similarities and it would be possible to correlate them even without the absolute age scale. Radiocarbon dating, however, conveyed confirmation that the peaks mainly of χ, MGS, Al/Si and Rb/Sr are synchronous. Although no macrofossils were found for dating, bulk ^{14}C samples correspond well between each other, so that no other customization was necessary to the age-depth model. Moreover, bulk dates were successfully used in nearby lakes on crystalline bedrock with satisfying results (Luoto et al. 2013). Hence, there is good confidence that age-depth model for both profiles

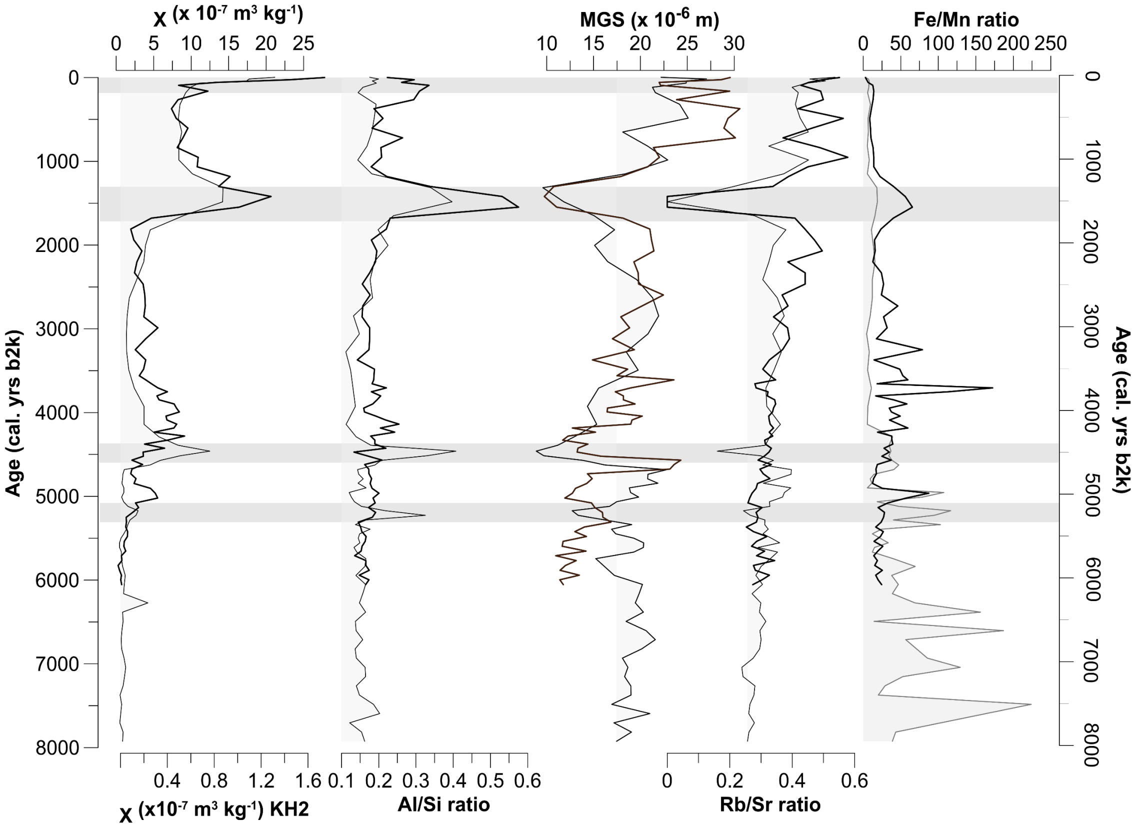

Figure 6.2 Correlation of selected proxies in cores KH2 and KL1 from Jarfjorden. Thanks to good correspondence, data are plotted on age scale so that similarity would be more evident.

is right. The only slight disagreement may be found between lower χ and MGS peaks at 5.2 and 4.5 ka b2k in core KH2, which are shifted by approximately 0.2 ka b2k in core KL2 towards younger age (Fig. 6.2). This slight divergence, however, is already inherent in standard error of 14C dates and does not represent a substantial complication. Mean temporal resolution of the records is ~100yrs for KH2 and ~70 yrs for KL1, which is still satisfactory value for discerning (sub-)millennial cycles or events (Lowe and Walker 2014). Profile KL1, unfortunately, spans shorter time interval than KL1 by 2 ka less, but in spite of this most of the Middle and Late Holocene are covered.

VI.1.3 Kobbefjord profiles

According to the results of radiocarbon and short-lived radioisotope dating the cores L4 and L3 cover nearly the last millennium. As such they represent a detailed environmental archive with approximate (although quite variable) temporal resolution of ~5–15 years. Perceptible uncertainties characterizing constructed age-depth models are the result of rather large AMS ^{14}C dating errors affected by low amount of organic carbon (generally < 1 mg C) in dated samples. The uncertainty is further emphasised by coincidence with radiocarbon plateaux, i.e. periods of increased variability in atmospheric ^{14}C content (Guilderson et al. 2005). These plateaux hinder or practically disenable accurate dating after 1650 AD (Stuiver 1978), which is also the case of herein presented chronostratigraphies. Despite these difficulties simulated age-depth models can be considered robust and reliable thanks to combining two different dating methods, using only terrestrial plant macrofossils for ^{14}C dating (Barnekow

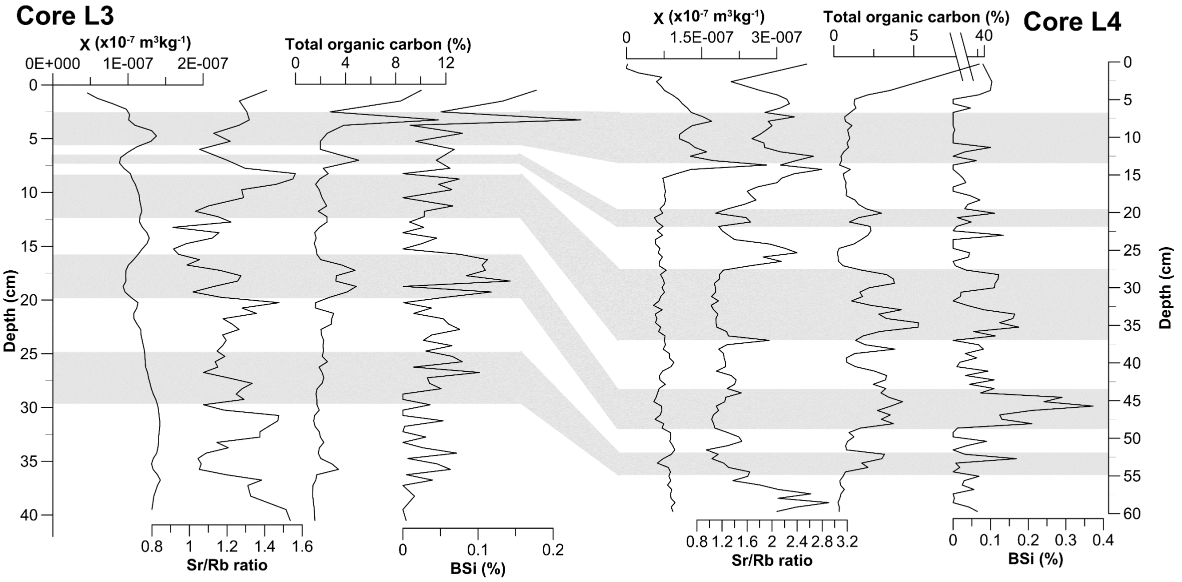

Figure 6.3 Correlation of main proxies from cores L3 and L4 as linked by CPLSlot with weights of magnetic susceptibility, Sr/Rb ratio, TC and BSi. Profiles are displayed on different depth scales.

et al. 1998; Björck and Wohlfarth 2001), and finally obtaining comparable results for both investigated profiles (Fig. 6.3). Slumping or other perturbations of sediment in certain parts of the cores may thus present the most prominent uncertainty of chronology, owing *inter alia* to low resolution of dated points. The tops of the cores have been, however, deposited very recently and continuous sedimentation has been ongoing until present, as short-lived radioisotope dating convincingly suggests, exponential decrease in ^{210}Pb in particular (Fig. 2). Additional chronological control is added by the peak of ^{137}Cs in two samples of core L4 that probably records culmination of nuclear bomb testing before its ban in 1963 AD (Appleby 2008); these two samples display ages of 1955 and 1978 AD, the dates that closely encircle the 1963 bomb peak. Sudden increase in accumulation rate observed in topmost layers (upper ~3 cm) of both cores probably reflects a lesser degree of sediment compaction close to the lake bottom or an artefact of dating (exponential increase in age of samples dated by short-lived radionuclides implying high rates close to the top) rather than elevated sediment input into the lake basin alone. This is supported by decreasing values of χ towards the tops of the cores.

Linking the two cores L4 and L3 proved difficult due to abovementioned discrepancies in accumulation rate, even if they were both ^{14}C dated. The accumulation rates of two cores, however, greatly differed in the respective lower and upper parts. The lower lake L3 seems to have been infilled earlier, already by ~500 yrs b2k, after which the accumulation rate decreased. The upper lake L4, to the contrary, entered the phase of maximum sedimentation ~200–100 yrs b2k. Therefore, the depth with prominent peak of TC and BSi at 15–20 cm in L3 most probably corresponds to depth 43–48 in L4. Likely explanation for this divergence in sedimentation rates may lie in that lake L3 had been largely infilled before the littoral of lake L4 developed into a bog and more effectively captured the input of material. Catchment filtering in the upper lake thus restricted downstream transport of entrained material, following the paludification and infilling of the upper lake (Anderson et al. 2012). Also given this reason, the lower lake is not as suitable for extracting climatic signal as the upper lake L4, due to great inter-basin interactions and influence by other than climatic factors. Further in this thesis, emphasis will be put on the interpretation of the records from lake L4.

VI.2 Interpretation of proxy data in relation to specific conditions of given lake/catchment/climate in studied areas and to age-depth models

VI.2.1 Garmaksla Lake

Very atypical composition of the sediment from Garmaksla Lake undoubtedly influenced abiotic conditions, which are revealed by performed physical and geochemical analyses, usually applied to more inorganic, minerogenic material. Extremely high organic content in conjunction with carbonate bedrock thus implies diamagnetic behaviour of the sediment, conveying little interesting palaeoenvironmental information. High water and organic content in Garmaksla sediments profoundly affects also the detection of elements by XRF spectrometry (Boyle et al. 2015, Chawchai et al. 2015), to such a degree that concentration of light elements (LE) behaves almost exactly inversely to lithogenic elements of Ca, Cl, K, Fe and Sr content (Fig. 6.4). XRF data of element concentration in cores G13/1 and G13/3 were therefore aggregated together and subjected to factor analysis, so that the general principles governing the behaviour of geochemical proxies in the lake, valid for both cores, could be unravelled. Absolute values of these mostly lithogenic elements will be biased to a certain degree by LE variations, i.e. organic matter. Interestingly, however, LE content dramatically decreases in the core's top, where more water-saturated sediment would be expected, and where actually higher organic content was detected. Enrichment in lithogenic elements in the upper 10 cm of both cores (Fig. 5.3 and 5.4) could therefore indeed mean elevated input of detrital material into the lake (Kylander et al. 2011). Moving now on to Si and Al, these elements, significantly saturating PC2, explain still about one fourth of total variance, yet their variation is unaffected by changes in LE and other minerogenic elements. Si and Al originate most probably from alumino-silicate minerals, brought into the lake by

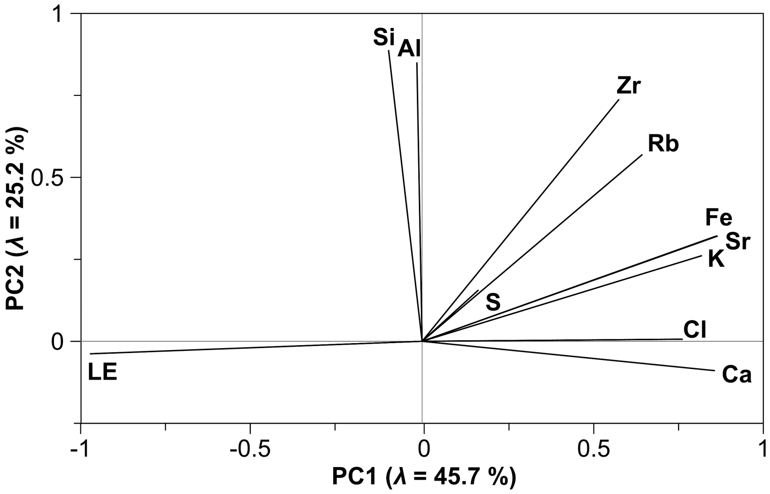

Figure 6.4 Primary component plot of aggregated XRF data from Garmaksla lake. The first and second component explain 45.7 % and 25.2 % of total observed variance, respectively. The light elements (LE) strongly negatively saturate the first PC and probably decrease the interpretative value of lithogenic elements.

weathering of local sandstones and siltstones (Håkanson and Janson 1983). Their contribution to overall sedimentary matter is minor compared to carbonates (represented by TIC, Ca and Sr), but not negligible. Finally, conservative lithogenic elements Zr and Rb saturate both primary components and also reflect detrital input, since these two elements play little role in biochemical cycles (Kylander et al. 2011). Zr is associated with heavy minerals (e.g. zircon) and generally coarser fraction, whereas Rb is enriched in finer common minerals such as mica and clays. Zr/Rb ratio therefore reflects granulometric changes of detrital material (Kylander et al. 2011), as evident when comparing Zr/Rb profiles of G13/1 and G13/3 with MGS in G13/2. Gradual increase of all these parameters throughout the record indicates coarsening of the material. Similar trend of other proxies for coarser grain size, ratios of Zr/K (Cuven et al. 2011) and Zr/Fe (Wilhelm et al. 2013), confirms this gradual MGS increase.

Ca/Si and Sr/Rb ratios also display a similar trend in both cores. Close correspondence between the Ca/Si and Sr/Rb profiles in the individual cores (Fig. 9.x) suggests both these ratios share a similar mechanism. Ca/Si ratio may indicate relative proportion of carbonates to silicates in the sediment, i.e. relative proportion of authigenic carbonate precipitation to detrital input (Jouve et al. 2013). Sr/Rb ratio usually indicates relative contribution of physical and chemical weathering to detrital inputs (Kalugin et al. 2007), as Sr is more easily leached and drained from the open catchments than Rb. Strontium, however, often co-precipitates with calcite, either partially substituting Ca in the crystal lattice, or as strontianite, mineral of aragonite group (Kylander et al. 2011). Sr/Rb could thus also indicate intensity of authigenic carbonate precipitation, similarly as Sr/Ti ratio (Kylander et al. 2011), which could not be used in Garmaksla profiles due to poor detection of Ti. Imperfect similarity between the abovementioned Ca/Si and Zr/Rb ratios may arise from biogenic utilization of silicon by diatoms or differential precipitation of $CaCo_3$ and $SrCO_3$.

Calcareous bedrock induces natural alkalinity of the lake water, with pH ~8.5–9 (as measured in summer seasons of 2012 and 2013; Čepová 2013, Pinseel 2014). Carbonate system of the lake is suited to buffer shifts in pH by establishing an equilibrium between $Ca(HCO_3)_2$, CO_2, HCO_3^- and CO_3^{-II} (Wetzel 2001). Any changes in CO_2 will cause reaction of buffering mechanism and cause changes in calcite precipitation, according to the equation:

$$Ca(HCO_3)_2 \leftrightarrow CaCO_3 \downarrow + H_2O + CO_2$$

Influx of Ca$^+$ and (bi)carbonates from the catchment by chemical weathering ascertains that high concentrations of dissolved HCO$_3^-$ (dominant at pH ~8.5), but also CO$_2$ and CO$_3^{-II}$ are present in the water and available as nutrients for phyto- and zooplankton (Wetzel 2001). Calcification of calcareous plants and algae may indeed stimulate photosynthesis by preventing CO$_2$ depletion (McConaughey and Whelan 1996). Thanks to high pH, a portion of excess dissolved carbonates is precipitated as authigenic CaCO$_3$ (and other carbonate minerals) and deposited in the sediment (Håkanson and Janson 1983). High TIC and Ca content in Garmaksla cores thus suggest a continuous carbonate precipitation took place under alkaline conditions. However, in the upper 5–15 cm both these parameters drop substantially. Precipitation of calcite may cease due to changes in lacustrine conditions such as water temperature or salinity (calcite is less soluble in warmer, more saline water), but most affected is by increase in CO$_2$ partial pressure and concomitant response of the lake buffering mechanism (Wetzel 2001). Therefore, CO$_2$ increase might have been the primary driver of limnological changes, making carbonates more soluble and preventing thus their deposition. What was the cause of this CO$_2$ increase and in which part of the water column did it occur? Pinseel (2014) notes the increased occurrence of *Achnanthidium rosenstockii*, a diatom typical for highly calcareous waters, mainly in Biozone D (depth 5–15 cm in G13/1), precisely corresponding to TIC and Ca minima. According to Pinseel (2014), decline of *A. rosenstockii* at 5 cm was brought about by a transition of lake water towards less calcareous (i.e. alkaline) conditions, possibly in response to elevated levels of anthropogenically induced acid precipitation. However, Svalbard lakes in general, and

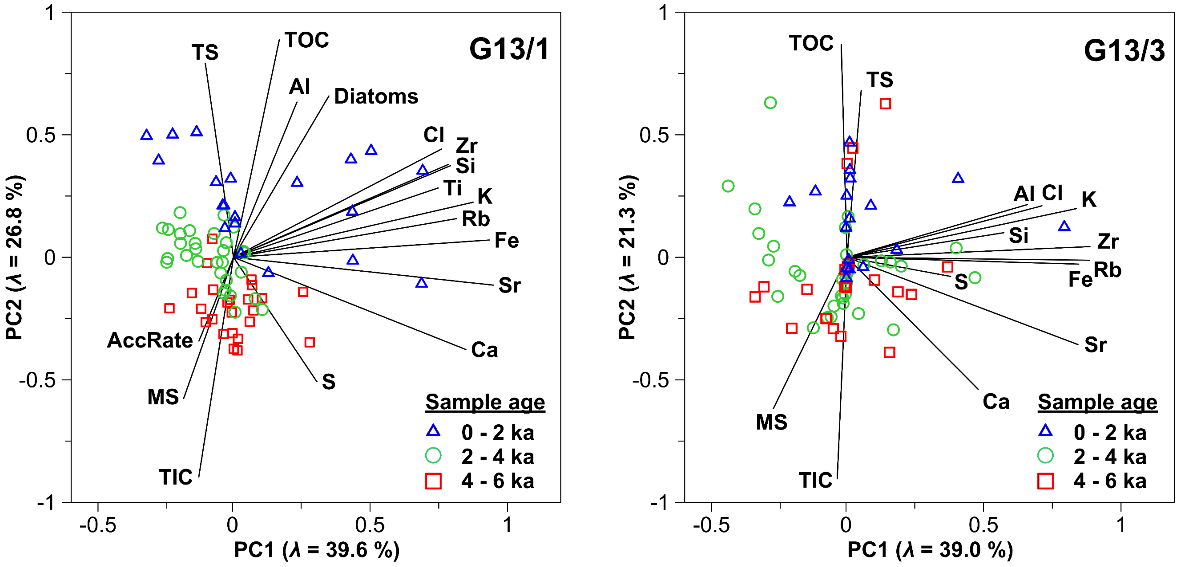

Figure 6.5 PCA biplot of geochemical data and χ (plus accumulation rate and diatom productivity in the left chart) for two Garmaksla cores G13/1 and G13/3. The two PC explain 66.4 and 60.3 % of the total variance in respective cores. Modelled age of the samples, plotted using their PCA scores, is denoted by coloured samples (in ka b2k).

Garmaksla Lake without a doubt as well, are considered well buffered from effects of acid rain (Lien et al. 1995). Moreover, deficiency of Ca and TIC between 15 and 5 cm depth indicates that calcium and carbonate ions were dissolved in water at this stage, offsetting the excess of CO_2, and presenting thus more bioavailable $Ca(HCO_3)_2$ for *A. rosenstockii* (McConaughey and Whelan 1996; Wetzel 2001). Depths 5–15 cm are believed too old to be anthropogenically affected, therefore most likely explanation for CO_2 increase is enhanced biological respiration or suppressed photosynthesis (Wetzel 2001; Cohen 2003). Such conditions might have occurred, providing the lake was stratified or shielded enough to prevent substantial exchange of dissolved gases with the atmosphere. This evidence points to periods of prolonged ice cover or establishment of stable water stratification at ~1.5–0.4 ka b2k (Wetzel 2001). Subsequent disappearance of *A. rosenstockii*, and hint of recovery of Ca and TIC content in the topmost 5 cm might indicate return to conditions suitable for carbonate precipitation. This resulted either from intensified photosynthesis, accompanied by greater utilisation of CO_2, or increase in water temperature or salinity (Wetzel 2001). Gradual decline of Ca and TIC negatively correlated to increase of organic carbon is apparent also in ordination diagrams of geochemical data, where samples are grouped according to their inferred age (Fig. 6.5).

Very small ratio of catchment to lake surface area (~6.5) implies the dominance of in-lake processes (Sarmaja-Korhonen et al. 2005, Van Hove et al. 2006). Role of catchment processes is presumably diminished, resulting in small detrital input by hydrological processes, except possibly by sheet flow or nival discharge. Solutes may be delivered into the lake through subsurface percolation in active layer (Woo 2012). Aeolian influx of silty and fine sand, on the contrary, plays relatively dominant role in such exposed setting (Zwoliński et al. 2008, Rydberg et al. 2016). The elevated plateau to the west of the lake, adjacent to the proglacial zone of Jottunfonna, might presumably offer abundant material to be swept by wind and carried to the lake surface, even though the predominant wind direction lies in the north-south axis of Billefjorden (Zwoliński et al. 2008, Láska et al. 2012). Exceptionally high content of organic matter in this oligotrophic lake, however, suggests that even this influx of material is of minor importance. Autochthonous bioproductivity, therefore contributes most to the material of sediment, in the form of remains of algae, aquatic plants and other planktonic and benthic organisms. Large proportion of terrestrial mosses is also present, although majority arguably was not carried into the lake by streams, but rather washed in from the banks by waves or by inundation of the littoral during rising lake level (Bernardová, unpublished data). All this must be borne in mind when interpreting grain size data – since organic matter and inorganic biogenic material, such as diatom valves (Håkanson and Janson 1983), may constitute dominant fraction of sediment, any changes in community structure of Garmaksla biocoenosis may thus affect the grain size of sediment. Typical size of diatom frustule, for example, ranges from 2 to 200 μm, and large variability of dimensions applies also to present species of chrysophytes, cladocera or chironomid head capsules (Vondrák, personal communication). High clay fraction in the lowermost sediments may thus reflect dominance of relatively small diatom species *Amphora affinis* and considerable fragmentation of valves, as noticed by Pinseel (2014), or generally more advanced degree of decomposition. Similarly, less degraded plant remains near the core's top may cause apparent coarsening of the material (leaching in KOH during pre-treatment for grain size analysis does not usually degrade biogenic material; Last 2001).

Finally, the formation of laminae needs to be discussed, for they represent the most distinct feature of the whole lithostratigraphical record. Unfortunately, little can be concluded with certainty, as the cores were sampled in 1cm steps, which prevented preservation of laminae for closer investigation. Visually, the succession of layers appears to be formed by dark, organic-rich laminae, intercalated with light, siltier, more clastic layers (Fig. 9.2D in Appendix). Lamination is present in the sediment depths corresponding to age ~3–0.4 ka b2k. The absence of laminae before and after this period may have several reasons, although perturbations of sediment may be probably rejected – cores were taken from the deepest, level part of the basin with little probability of slumping, and lake fauna does not attain sizes allowing for significant amount of bioturbation (Vondrák, personal communication). However, changes in bryophyte assemblages at ~4.5–2.5 ka b2k, especially appearance of *Warnstorfia pseudostraminea*, preferring disturbed, periodically inundated habitats (Bernardová, unpublished data), indicate water level fluctuations in this period. Appreciable lowering of the lake level would thus enable wind-induced wave mixing even in presently profundal zone (in opposite to littoral zone that is influenced by waves, i.e. *sensu* Larsen and MacDonald 1993). Nonetheless, this does not explain absence of laminae in the lowest and top part of the cores (before 4.5 and after 0.3 ka b2k, i.e. diatom zones A and E) nor the origin of lamination.

Following this assumption, the mechanism responsible for laminae formation must have operated in the period equivalent to biozones C and D. Varved or laminated sediments were observed on Svalbard, although mostly in glacierised catchments and reflecting thus (annual) glacier activity and melt (Snyder et al. 2000, Guilizzoni et al. 2006, van der Bilt et al. 2015). Comparatively low number of laminae in Garmaksla cores definitely cannot be attributed to annual formation, considering high age of sediment. Moreover, accumulation rate slightly decreases with the onset of lamination, implying lowering of the detrital input rather than an increase. Therefore, a certain mechanism must be responsible for sudden switches in mode of deposition, from biogenic to detrital/minerogenic. Periods of intensified carbonate precipitation followed by biogenic deposition (Zolitschka et al. 2015) are improbable due to low Ca/Si and Sr/Rb ratios in Zone C. Influx of detrital material in arid environments could thereby result from storms or periods of intensified wind circulation (Francus et al. 2013). In climatic conditions of Svalbard, nevertheless, storms or strong winter winds are expected to occur regularly and probably would not be capable to entrain large amount of grains on single occasion. The resulting stratigraphic sequence would contain a greater number of thinner layers (Lamoureux and Gilbert 2004). Instead, prolonged multiannual periods of frozen lake surface would detain aeolian detrital accumulation on lake ice cover, possibly trapping the wind-blown material in snow covering the ice lid (Cuven et al. 2010). In the meantime, imprisoned biota would slowly accumulate on the lake bottom, only to be buried by piled aeolian dust when the ice lid melts during a warm summer (Retelle and Child 1996, Cuven et al. 2010). I lean towards this explanation as even in the unprecedently warm 21st century (Førland et al. 2010) Garmaksla Lake ice cover may break up as late as August (Čepová 2013, Kavan, personal communication). In the conditions of Neoglacial cooling, corresponding to laminae formation, persistent ice cover for several years in a row is very likely. The fate of aquatic communities during these unfavourable periods is uncertain, as their survival depended on many factors, such as the height of snow on the ice cover influencing light transmittance into the water column (Cohen 2003). Marginal moat of open water between the lake perimeter and the remaining frozen ice lid that often forms during summer could, however, sustain the life in the lake (Retelle and Child 1996, de Wet et al. 2017).

VI.2.2 Jarfjorden lakes

Signature of physical and geochemical proxies in the sedimentary records from Jarfjorden lakes is very similar to each other. Fluctuations in covarying content of lithogenic elements (mainly Si, Ca, K, Rb, Sr and Zr) explain approximately 30 % of the total variance in cores KH2 and KL1, as evident in PCA biplots (Fig. 6.6). It is, however, the second primary component (PC2) that shares not only the comparable loading variables, but also a remarkably synchronous trend in the records. PC2 is saturated primarily by χ, clay content, concentration of Fe, Mn (and Al in KH2), and Al/Si ratio. Correlation coefficients of these independently measured proxies are also very high, generally in the range of 0.4–0.8 for χ, clay, Fe, Mn and Al/Si ratio in both cores (Table 9.4 in Appendix). The peaks of these parameters are the most prominent features of both profiles and temporally coincide, so their origin is discussed in detail below.

On average, Fe content in coarser, magnetically weaker layers keeps below 1 %, but rises by an order of magnitude to the maxima 7–9 % in the peaks of both cores. The same is true for χ values in KL1 rising from $<1\cdot10^{-7}$ $m^3\cdot kg^{-1}$ to $27\cdot10^{-7}$ $m^3\cdot kg^{-1}$. However, χ in the samples of KH2 below 25 cm depth, displaying diamagnetic behaviour ($<10^{-9}$ $m^3\cdot kg^{-1}$, a few of them with negative values of χ) increases by two orders of magnitude to a maximum of $1.3\cdot10^{-7}$ $m^3\cdot kg^{-1}$. Supposing that for example magnetite, a strong ferrimagnetic mineral with $\chi = 5\cdot10^{-4}$ $m^3\cdot kg^{-1}$ (Thompson and Oldfield 1986), is the main source of χ signal, its theoretical concentration should range from virtually zero to no more than ~0.5 %. This is incongruous with the much higher total Fe content, but magnetite needs not to constitute the entire χ signal, as other ferri- or paramagnetic Fe-bearing minerals may represent the remaining bulk of iron content. Hence, the χ signal could be formed either completely by e.g. pyrrhotite (with $\chi = 5\cdot10^{-3}$ $m^3\cdot kg^{-1}$ a few % of pyrrhotite content would induce the observed χ; Thompson and Oldfield 1986), or by a combination of small fraction of magnetite and magnetically weaker mineral, such as haematite, constituting the rest. I incline towards the latter explanation, considering the ochre-red colouring of the layers with magnetic peaks, which is typical for haematite often forming ‘red beds’ (Thompson and Oldfield 1986). Furthermore, besides Fe, these prominent peaks have high content of Mn, Al relative to Si, and also Ti (otherwise mostly below LOD). Aluminium is often found in impurities of crystalline structure of magnetite (Fe_3O_4) and haematite (Fe_2O_3), constituting up to 10 wt % (Thompson and Oldfield 1986). Titanium constitutes titanomagnetites, more specifically the two end members magnetite and ulvospinel (Fe_2TiO_4), and also occurs in titanohaematites in the form of a continuum between polymorphous haematite/maghaemite and ilmenite ($FeTiO_3$; Thompson and Oldfield 1986). Finally, elevated Mn content may signify the occurrence of ferromanganese oxides and hydroxides, possibly in the form of jacobsite ($MnFeO_4$; Thompson and Oldfield 1986), or rhodochrosite ($MnCO_3$; Jones and Bowser 1978). All these minerals except rhodochrosite are oxides, the content of which implies oxic conditions prevailed during sediment accumulation with little subsequent reductive diagenesis (Jones and Bowser 1978, Håkanson and Janson 1983, Boyle 2001). Some of these minerals must be responsible for the observed magnetic signal, and presumably are also somehow connected to fining of the material.

Increase in χ values with smaller grain size was described in Holocene lake sediments on the British Isles (Thompson and Morton 1979, Snowball and Thompson 1990). Snowball and Thompson (1990) demonstrate increase in χ by the factor of 3–8 between the sand and fine clay fractions. It should be noted that magnetic crystal size is largely independent from granulometric grain size (Thompson and Oldfield 1986). Thompson and Morton (1979) interpreted simultaneous χ increase and particle fining in terms of increased concentration of primary magnetite, weathered from bedrock or till and carried from the catchment by fluvial processes. Changes of χ and grain size corresponded in this case to Late Holocene land-use changes, especially reduction in vegetation cover and deforestation, which led to preferential erosion of fine fraction (Thompson and Morton 1979). Gradual declining trend of χ during the Holocene with a slight increase in the last millennium or so is typical also for Finnish lakes, where the soil and vegetation maturation in the catchments reduced the availability of primary magnetite from glacial drifts, before land use changes increased its erodibility from the top soils (Stuber and Thompson 1979). This model could be valid for the two Jarfjorden lakes, as their catchments cover a rather large area (18 and 13.5 km^2) and magnetite may originate from local till or magnetite bands of gneissic bedrock. The cause of such changes in land cover, whether natural or anthropogenic, will be discussed later.

Second proposed model of inverse χ-grain size relation by Thompson and Morton (1979) involves erosion of fine-grained secondary ferrimagnetic minerals formed by pedogenesis from top soils. Land-use changes, e.g. grazing or forest clearance, again explain

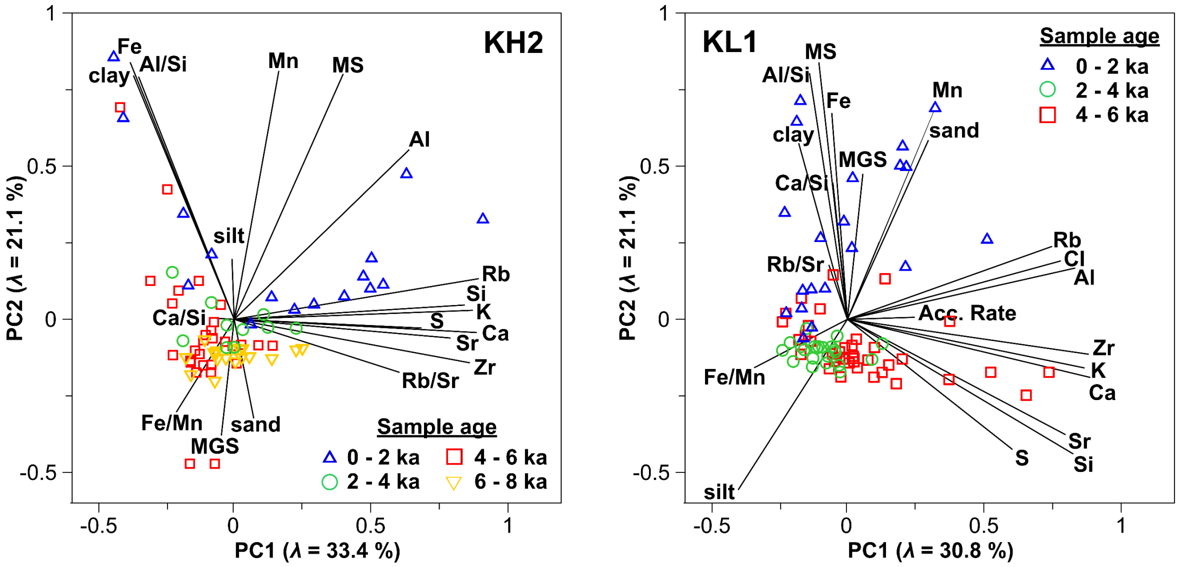

Figure 6.6 Biplot of primary components featuring main physical and geochemical proxies in cores KH2 and KL1, which together explain 54.5 % and 51.9 % of the total variance, respectively. Samples are visualised in the two-dimensional space according to their PCA scores and are categorised into groups based on their inferred age (in ka b2k).

the temporal variations of χ and grain size most easily, although catchments of Loch Lomond and arguably also Jarfjorden lakes lack substantial extents of mature soils, which would provide secondary ferrimagnetic iron oxides (Snowball et al. 1999). Furthermore, presence of very fine-grained superparamagnetic (SP) grains formed by pedogenesis ought to be revealed by heightened χ_{FD} (Dearing et al. 1996). In the χ peaks of Jarfjorden cores, however, χ_{FD} reaches only ~4%, which is more indicative of stable singe domain (SSD) magnetic grains (Dearing et al. 1996). Admittedly, χ_{FD} values might be depressed by frequency-independent paramagnetic or SSD ferrimagnetic grains (Dearing et al. 1996), but this suggestion cannot be corroborated in greater detail due to insufficient data. A few samples in Jarfjorden cores, directly preceding or following the χ peaks, reach χ_{FD} values 6–14 %, this could, however, result from error of measurement nearing the limit of instrument's resolution in magnetically weaker samples.

Changes in depositional environment may also explain correspondence of magnetic susceptibility and grain size (Thompson and Morton 1979). Lower-energy depositional conditions imply according to Stoke's law accumulation of finer material, with associated higher concentration of magnetic grains in the sediment (Håkanson and Janson 1983). Higher lake levels or less intensive wind-induced mixing of the water column could bring about a shift to less energetic environments (Håkanson and Janson 1983, Larsen and MacDonald 1993, Opitz et al. 2012), although given the synchroneity of Jarfjorden records, a clear regional impulse accounting for such change would have to be elucidated. Variable effective moisture and concomitant lake-level changes during the Early and Mid-Holocene thermal optimum were inferred by several studies in northern Fennoscandia (Wolfe et al. 2003, Korhola et al. 2005, Luoto and Sarmaja-Korjonen 2011), although these fluctuations affect predominantly closed-basin systems. Langvatnet and Holmvatnet are open lakes with very different catchment systems and basin morphology, hence the nearly identical sedimentary evidence recording a synchronous response of lake levels to hydroclimatic variations seems improbable. Thompson and Morton (1979) came to a similar conclusion in case of multiple lakes in Loch Lomond catchment.

So far only allogenic sources of ferrimagnetic material were considered, but authigenic lacustrine processes may give rise to formation of magnetic grains as well (Dearing 1999a). In Fennoscandian lakes, great attention has been given to magnetotactic bacteria, able to synthetize ultra-fine bacterial magnetite (Snowball et al. 1999, Paasche et al. 2004). In oligotrophic, oxic waters these microaerophilic bacteria intracellularly produce magnetosomes, i.e. biogenically precipitated SSD magnetite grains with diameter in the range of ~35–120 nm (Evans and Heller 2003, Paasche et al. 2004). According to χ and χ_{FD} values in cores KH2 and KL1, the magnetic signal could be indeed carried by SSD magnetite. Nonetheless, in spite of the greatly increased clay content (up to 18 %), no more than ~0.1 % of particles are smaller than 0.1 µm (although granulometric measurement is very imprecise at this end of the spectra). This amount of ultra-fine particles might be roughly responsible for the observed χ, if all these particles were formed by magnetite (which is improbable), but the source of absolute majority of remaining clay remains unexplained. On the other hand, biogenic origin of the magnetic signal is favoured by two observations. Firstly, terrestrial organic macroremains were not detected in the Jarfjorden cores, suggesting thus mostly autochthonous origin of organic matter, although analysis of organic matter content has yet to be performed to support this verdict. Secondly, χ peaks do not coincide with lithogenic elements of Si, Ca, Rb and Zr, usually signifying detrital input (Davies et al. 2015), which is corroborated by negative correlations of these elements with χ, clay, Fe, Mn and Al/Si (Table 9.4). To conclude, a remarkably pronounced regional impulse would be necessary to induce blooms of magnetotactic bacteria in two independent catchments, as envisaged by Paasche et al. (2004), although the mechanism of which is unidentified in Jarfjorden lakes.

Another aspect of complexity of relationship between χ, grain size and chemical composition arises when inspecting more closely the lower half of core KH2. Below 17 cm the silty sediment carries only paramagnetic to diamagnetic signal (mean $\chi = 3.3 \cdot 10^{-9}\ m^3 \cdot kg^{-1}$), yet its iron content averages at ~0.5 %. This can be explained by a presence of paramagnetic, Fe-bearing mineral, most probably belonging to iron sulphides (Thompson and Oldfield 1986). Indeed, regarding the dilution effects of organic matter and siliciclastic material, 1% mineral fraction composed predominantly of paramagnetic pyrite (FeS_2) with admixture of greigite (Fe_3S_4) or pyrrhotite (Fe_7S_8) would produce the observed χ signal (Thompson and Oldfield 1986) and correspond to 0.5% Fe content. These iron sulphides are formed by diagenesis in prevalently eutrophic, reducing environments of lake bottoms, provided enough iron and sulphur is present in the form of e.g. decomposing organic matter (Jones and Bowser 1978, Evans and Heller 2003). Snowball (1993) demonstrates at the example from lake in Abisko, northern Sweden, that magnetite can be the source of Fe for this sulfurization reaction, leading to a complete post-depositional dissolution of Fe_3O_4. He argues that these anoxic conditions, characteristic by low redox potential and high Fe/Mn ratio, are conditioned by elevated TOC, reflecting thus climatic amelioration. Fe/Mn ratio is a well-established proxy for palaeoredox conditions (e.g. Cuven et al. 2011, Davies et al.

2015); Mn is more prone to dissolution than Fe under reducing conditions, hence increase in Fe/Mn indicates bottom-water hypoxia or enhanced stratification (Boyle 2001, Davies et al. 2015). If reducing conditions are too severe, however, even Fe can be remobilised (Snowball 1993). Returning now to the Jarfjorden cores, the lower part of core KH2 exhibits elevated, but highly variable Fe/Mn ratio, supporting thus assumption of sulfurization and authigenesis of iron sulphides. Markedly fluctuating profile of Fe/Mn is then indicative of intermittent periods of severe anoxic conditions during which even Fe was released from the sediment (Jones and Bowser 1978, Snowball 1993). The period 8–4.5 ka b2k thus might have been characterised either by high bioproductivity, or intensified stratification. Unfortunately, this trend is not reproduced in core KL1. Higher Fe/Mn ratio occurs at around 4 ka b2k, although this is probably caused by very low Mn content. Nevertheless, χ is very low before 4.5 ka b2k. Also, from ~3 ka b2k, Mn content and Mn/Fe ratio, indicatory of oxic conditions (Melles et al. 2012), rise in both cores. Besides, ochre-red colouring implies haematite staining, formed by *in situ* oxidation of detrital magnetites in well oxygenated, oligotrophic waters (Thompson and Oldfield 1986).

Only for completeness, it needs to be mentioned that Fe-rich clay and fine silt laminae with high χ were described by van Daele et al. (2014), who interpret them as layers of tephra, deposited by volcanic eruption in the catchment and afterwards fluvially transported to the lake basin. Given the thickness of clayey layers in Jarfjorden cores, and considering the distance from nearest areas with active volcanism, this source seems highly improbable. Final aspect of these magnetic clayey peaks that has not been discussed yet, high Al/Si ratio, may reflect simply fining of the material (van Daele et al. 2014) or mineralogical changes related to affinity of Al to crystal lattices of ferrimagnetic minerals (Thompson and Oldfield 1986).

Thus, arriving at a conjecture, the influx of fine-grained material with high primary magnetite content seems the most plausible explanation of coinciding peaks of χ, clay, Fe content and Al/Si ratio, in accordance with conclusions of Thompson and Morton (1979), and Stober and Thompson (1979). The magnetic signal was well preserved in oxygen-rich, oligotrophic environment after 4.5 ka b2k, but the earlier record of magnetic detrital input seems to have been obliterated in more productive, oxygen-depleted environments (Snowball 1993). Contemporaneous periods of increased erosion were presumably incited by an external forcing mechanism. Of these, climatic changes are only one of the possible triggers, and most probably would operate in a form of several feedbacks and interactions with landscape. Changes in climatic oceanity or effective moisture could thus induce opening of vegetation cover and shift of treeline and forest line, leading to greater vulnerability of soils to erosion (Allen et al. 2007, Hofgaard et al. 2013).

Land use changes may have caused the observed erosion as well, since rapid reduction in vegetation cover facilitates entrainment and transport of fine weathered material, either derived from soils or regolith (Thompson and Morton 1979). Moreover, Arctic ecosystems are sensitive to even modest anthropogenic impacts, as shown by Massa et al. (2012) in southwestern Greenland. Human settlement of Fennoscandia has a long history, according to Sørensen (2014). Increases in agricultural practices, agrarian expansion, deforestation, heathland expansion took place as far north as Finnmark and as early as 4.5–4.2 ka b2k. Second stage of agrarian expansion, with more common husbandry practices and evidence of erosion, occurred at 2.8–1.5 ka b2k, corresponding to the Iron Age (Sørensen 2014). Evidence of human occupation in Sør-Varanger dates back to Younger Stone Age, as attested by remnants of Gropbakeengen settlement near Kirkenes, whose population peaked at ~4.5 ka b2k (Helskog 1984). This period conspicuously coincides with the first magnetic peaks in Jarfjorden sedimentary cores. Agricultural activities are documented by findings of numerous pollen of grasses in Jarfjorden, indicating pastures and husbandry at 3.1–2.5 ka b2k (Jensen 2012 in Sørensen 2014), and also by discovery of charcoal dust and pollen of *Hordeum* (barley) found in gyttja sediments in Pasvik River valley at 2.5–2 ka b2k, indicating settlement and agricultural practices (Skandfer and Høeg 2012). Most importantly, the second, more pronounced magnetic peak in both records is in close agreement with the inferred period of intensified grazing in Jarfjorden area at ~1.5 ka b2k (Vorren 1983 in Helskog 1984). Concentration of reindeer herds close to drainage areas of studied lakes by ancient Saami populations might have been the trigger for observed erosional events (Andersen 2011). Alternatively, forest clearances by burning or timber exploitation would result in a similar effect, as proposed by Karlsson et al. (2007), although probably not on such a scale as to be recorded in Jarfjorden cores.

Finally, the last and most prominent χ peaks occur in the last ~70 yrs in both cores. This time, however, grain size, Fe and Al/Si ratio do not follow χ variations. Instead, a marked increase of Cu/Rb ratio and detection of Ni for the first time in the upper 1.5 cm of KH2 accompany peak of magnetic susceptibility. I interpret these signals as evidence of airborne pollution from the nearby nickel-copper industrial complex of Petchenganickel Combine, namely the smelter in Nikel and roasting factory in Zapolyarnyy. The production of emissions of SO_2 and heavy metals began in AD 1940s (Myking et al. 2009), which is imminently reflected in the sedimentary record by rising χ, Ni/Rb and Cu/Rb. The SO_2

emissions peaked in AD 1979 and have substantially decreased since, but still they surpass the total volume of Norwegian SO_2 emissions five times (Myking et al. 2009). Local boreal forests have been substantially damaged and in addition to soils, rivers and lakes they have been strongly acidified (Aarestad and Amlid 2009, Myking et al. 2009). The steep rise of χ values towards the tops of the cores probably signifies deposition of airborne ferromagnetic spherules with diameter in the range of 1–20 µm, accompanying fly-ash particles rich in Ni and Cu (Petrovský and Elwood 1999, Evans and Heller 2003). Findings are in concordance with spatially much more expansive study of heavy-metal contamination in Norway-Russia borderland by Rognerud et al. (2013), yet with added advantage of accurate chronological control by ^{210}Pb dating, revealing also a temporal trend of progressively escalating pollution.

So far, I discussed only the origin of magnetic peaks in Jarfjorden records (represented by PC2), which are synchronous and pronounced. The majority of variance in the factor analysis of physico-geochemical data is, however, explained by PC1, denoting mainly the concentration of lithogenic elements (Kylander et al. 2011). That is generally in good agreement between the cores, although PC1 reaches maximum values in KL1 before 4.5 ka b2k, and diverges significantly from KH2 trend. The underlying cause of variations in concentration of lithogenic elements is not clear. Changes in deposition of autochthonous organic matter might dilute detrital material (Virkanen 2000, Chawchai et al. 2015). Hypothesized explanation of disagreement between the two records could involve paraglacial relaxation of steep rock wall on the southern bank of Langvatnet, which would supply debris into the lake basin via gravitational processes early in the Holocene (Ballantyne 2002). Holmvatnet is set in lower relief, and thus the detrital input was restricted to fluvial or aeolian transport already in the earlier phases of the Holocene, resulting in more stable PC1 trend. A rising trend of PC1 in the last ~1ka is, however, coincident with increasing sand content. Niveo-aeolian processes could represent a feasible mechanism responsible for transport of coarse-grained, lithogenic material in (mostly) tree-less tundra environment (Virkanen 2000, Zwoliński et al. 2008, Cuven et al. 2010, Anderson et al. 2012). Strong winter winds could deflate and carry silt and sand grains, and deposit them on lake ice cover, releasing then into lake when ice ablates (Cuven et al. 2010). Thin snow cover and sparser vegetation facilitate such mechanism (Allen et al. 2007, Rydberg et al. 2016). This sedimentation pathway would at the same time explain deposition of very coarse sand grains, detected in few layers in the bathyal zone of the lakes (Cuven et al. 2010). Influx and accumulation of fine silt and clay particles should be, on the other hand, realized through fluvial entrainment and settling from the overflow or underflow plumes (Håkanson and

Janson 1983, Cockburn and Lamoureux 2008, Rydberg et al. 2016). Inverse relationship of fine and coarse fractions is interpreted simply as dilution of wind-borne material by fines during periods of increased fluvial erosion.

VI.2.3 Kobbefjord

The infilled basins were fed by through-flowing streams, their sedimentary record should therefore contain predominantly information of the external conditions in the catchments and mode of deposition. Total carbon content, probably predominantly organic (since no substantial source of carbonate rocks is located in the catchments), should therefore correspond to influx of organic matter from the drainage area. Elevated input of organic matter of terrestrial origin in the topmost layers is thus documented by high TC and C/N ratio. C/N ratio is an indicator of relative dominance of aquatic or terrestrially-derived organic matter in the sediments (Janbu et al. 2011; Kylander et al. 2013) and roughly corresponds to TC and TN profiles. The average C/N values (14–20) throughout the majority of cores L4 and L3 indicate that algae as well as aquatic and vascular plants contributed comparably to the organic matter in the sediment (Meyers and Lallier-Vergès 1999). This is confirmed by significant, but not perfect correlation of TC and BSi, a proxy of diatom productivity. BSi parallels some of the shifts in TC and indicates periods of ameliorated limnic conditions, but BSi values remain low, when terrigenous input prevails. Several periods of elevated C/N ratio (>20–30) stand out from the record and indicate events of enhanced hydrological activity transporting more terrestrial organic matter into the lakes.

Grain size should also reflect the intensity of runoff, considering that the coarser grain size necessitates higher energetic erosional and depositional environment (Lapointe et al. 2012). In our catchment rainfall events are considered the dominant hydrological process, with secondary contribution of spring/summer snow and glacial melt. Increase in MGS should thus indicate shift towards higher precipitation (greater catchment runoff and/or availability of meltwater from snow cover) or higher spring/summer air temperatures (increase in nival and glacial melt; Lamoureux and Gilbert, 2004; Lapointe et al. 2012). Correlation of χ with sand fraction supports association of heavy ferrimagnetic minerals with coarser grain size (Nehyba et al. 2011). The sand fraction therefore represents terrigenous clastic material, while organic matter is clearly associated with silt fraction. Remarkable synchronous increase of both MGS (to >400 μm) and organic matter in the topmost sample of core L4 is, however, caused by presence of coarse organic matter (Van Daele et al. 2014). Finally, aeolian input of terrigenous clastic material into the lakes should be considered, since multiple studies document increased aridity and wind activity in inland West Greenland in the past millennium (Møller et al. 2006; Anderson et al. 2012). Relative contribution of aeolian transport in the studied catchments under marine influence should nevertheless be of minor importance relative to hydrological sediment discharge, and in any case remains unresolved by grain-size analyses alone. Generally, χ is primarily dependent on the content of lithogenic matter carried into the lake by catchment geomorphic processes and this was found valid for Greenland as well (Anderson et al. 2012).

Three distinctive groups of elements were differentiated by PCA analysis of the XRF data (Fig. 6.7): the first principal component PC1 juxtaposed elements bound to organic matter (C, N, S, P) and those found in aluminosilicates (Si, Al and Sr), represented in the studied catchment mainly by feldspars of the gneissic bedrock (Escher and Pulvertaft 1995). Similar behaviour of Al and Si suggests they share the same source, which favours the interpretation of feldspar and mica origin over quartz-containing granites. The Al/Si ratio then corresponds mainly to grain size variations, as evidenced by positive correlations of Al/Si with clay and silt (significant in core L4; Van Daele et al. 2014). The PC2 was saturated by elements Fe, Ti, Rb and Zr, that are associated with hard, heavy minerals (Cuven et al. 2010). All of these lithogenic elements are believed to reflect detrital input into sedimentary basins (Kylander et al. 2013; Davies et al. 2015). Several ratios, such as Si/Ti, Si/Zr or Sr/Rb, can discriminate between these two main groups of lithogenic elements. The Si/Zr and Si/Ti ratios are frequently used as a proxy for biogenic silica content (Balascio et al. 2011; Cuven et al. 2011). Based on the positive correlations of these ratios with MGS, we argue that they

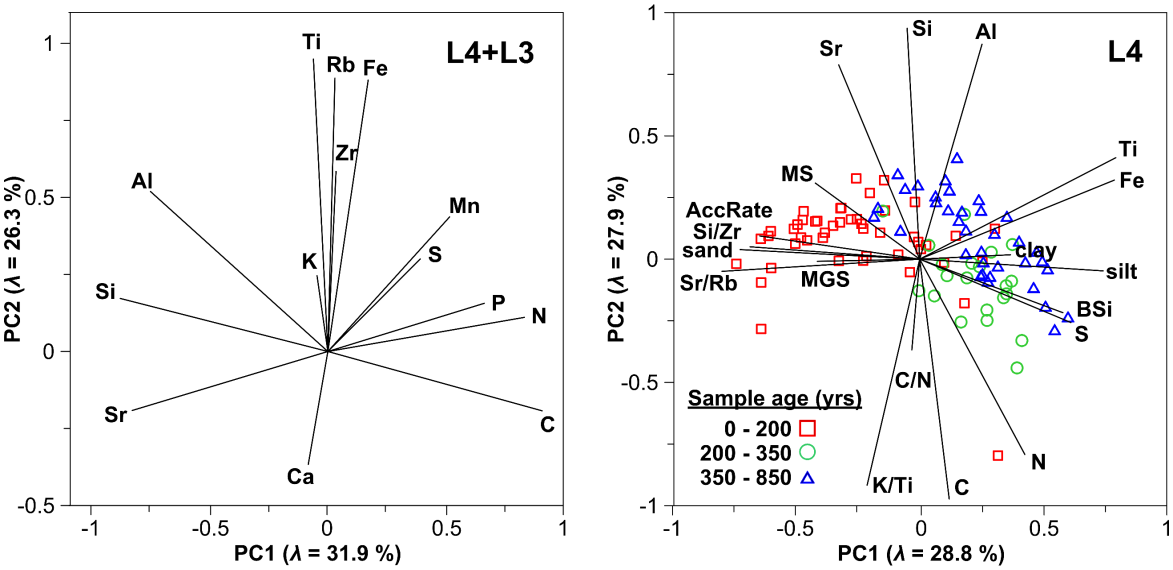

Figure 6.7 Left: Primary component plot of most abundant elements in aggregated data from cores L4 and L3. The XRF and TC, TN and TS geochemical data from both cores were aggregated and analysed together. Right: PCA of main elements and their rations, with granulometric and sedimentological data of core L4 with samples divided according to their age (in yrs b2k).

reflect rather coarse-grained input for our study, as envisaged by Shala et al. (2014). Sr/Rb correlates with MGS even stronger, which is conditioned by affinities of Sr and Rb to sand and clay, respectively. In addition to association with grain size, Sr/Rb ratio (or inverse Rb/Sr) is believed to reflect relative contribution of physical and chemical weathering to the input of terrigenous matter into lake basins (Xu et al. 2010; Fernández et al. 2013), i.e. greater input of unweathered terrigenous fraction (Kalugin et al. 2007). Sr/Rb significantly correlates also with K/Ti (r = 0.28 and r = 0.38 in cores L4 and L3, respectively), serving as another indicator of physical weathering intensity (Arnaud et al. 2012). Potassium is enriched in non-weathered primary minerals, but is relatively quickly leached by weathering processes in contrast to Ti. Higher K/Ti thus signals chemically less altered regolith (Arnaud et al. 2012). The role of Ti, often used as a proxy of detrital material, is questioned by its positive correlation with TC in core L4 (r = 0.31). Both Ti content and TC are correlated with and usually bound to silt fraction (Cuven et al. 2010) and may thus merely reflect the simultaneous input of organic and fine-grained clastic matter into the lake. Calcium is probably also of clastic origin as it covaries with other proxies of detrital input in both cores, mainly Sr/Rb. Granodioritic gneisses contain Ca-rich plagioclase feldspars (Anderson et al. 2012), corroborating thus the idea that feldspars are the source minerals of aluminosilicates.

Redox conditions, principal characteristics influencing in-lake processes, can be inferred from the Fe/Mn ratio (Cuven et al. 2011). In core L4 Ti-normalized Fe and Mn trends are synchronous, suggesting that aerobic conditions prevailed at the lake bottom (Kylander et al. 2013). Such conditions could be expected in this through-flowing infilled lake, which could not attain great depths during the span of our sedimentary record. However, the Fe/Mn ratio peaks at 15 cm (Zone 4b), while it decreases in the topmost sample (Zone 5). Increase in Fe/Mn occurs concomitantly with χ maximum, C/N and Si/Ti peaks and Ca content drop, which may indicate an event of anaerobic decay of organic matter, methanogenesis and N degradation in the sediment (Wetzel 2001). Alternatively, or simultaneously, input of both clastic (minerogenic) and organic material from the catchment was enhanced at that time. Based on the Fe/Mn ratio, the top of the core L4 is on the contrary well oxygenated (Boyle 2001), which suggests complete infilling of the lake and/or lowering of the water level connected with stream incision into the lake infill surface.

VI.3 Synthesis of Holocene palaeoclimatic reconstructions in the North Atlantic region

VI.3.1 Garmaksla, Svalbard

Sedimentary record of Garmaksla Lake reveals a distinct evolution of lacustrine conditions since the Middle Holocene, affecting markedly biological communities in particular. Although quantification of past fluctuations of lake water temperature was so far unsuccessful in case of diatoms due to problems with transfer function (Pinseel 2014), chironomid-based reconstruction of past summer temperatures will likely produce promising results (Vondrák, unpublished data). For now, integrated interpretation of available abiotic and biological proxies offers only qualitative information on past limnic, and by inference local atmospheric, conditions. These changes are confronted with other palaeoenvironmental records from Svalbard (Fig. 6.8) and discussed with possible driving factors and implications for the future direction of the Holocene palaeoenvironmental research in Svalbard.

Notwithstanding the ambiguous interpretation of abiotic proxies in the oldest part of the record, diatom and bryophyte assemblages suggest favourable, rather warm conditions between 5.7 and 4.7 ka b2k (Pinseel 2014, Bernardová, unpublished data). Reasoning is based primarily on prevalence of mesotrophic diatom species *A. affinis* relative to *S. venter*, which conversely prefers colder, more oligotrophic conditions (Fig. 9.4; Pinseel 2014), and abundant occurrence of moss *Calliergon richardsonii*, requiring nutrient-rich environments (Bernardová, unpublished data). Suitable conditions for lake biota, which would be reflected also in abiotic proxies, are suggested only indirectly, perchance by small grain size and low content of coarse silt and sand, implying minimum aeolian clastic input and therefore less vigorous atmospheric circulation (Lamoureux and Gilbert 2004). Biozone A therefore corresponds to the concluding stages of HTM, which was otherwise very pronounced on Svalbard particularly in the Early Holocene (Hald et al. 2007, van der Bilt et al. 2016, Mangerud and Svendsen 2017).

The gradual onset of Neoglaciation is documented by ample evidence from various proxy data and settings around Svalbard. The oceanographic changes usually appeared earliest, already by the beginning of the Middle Holocene, as seen in decline of sea surface temperatures (Hald et al. 2004, Carbonara et al. 2016, Werner et al. 2016) or increase in sea ice concentration in the Fram Strait (i.e. annual southward migration of sea ice front; Müller et al. 2012). Relative dominance of colder Arctic water/meltwater to warmer Atlantic waters is regarded as the driving factor of the overall North Atlantic cooling (Rasmussen et al. 2014). Mangerud and Svendsen (2017) document this gradual replacement of Atlantic waters by decline of thermophilous molluscs *Mytilus edulis*, until at last disappeared from Svalbard between 4.5 and 3.8 ka b2k. These late survivors were found in the very area of the inner Billefjorden, where the climate is most continental and the Arctic waters may have arrived here latest. Sedimentary signature of ice-rafted debris (IRD) from the bottom of Billefjorden further indicates that activity of tidewater glacier Nordenskiöldbreen (10–15 km NE from Garmakla) increased at ~5.5 ka b2k, although more persistent sea ice cover impeded further deposition of IRD after ~3.2 ka b2k (Svendsen and Mangerud 1997, Baeten et al. 2010). On the other hand, enhanced, yet unstable subsurface (>200 m depth) inflow of warm, saline Atlantic waters to Fram Strait is found after 3 ka b2k and suggests decoupling of temperatures between surface and subsurface waters, probably isolated by a distinct pycnocline, west of Svalbard (Rasmussen et al. 2014, Werner et al. 2016). Enhanced stratification in conjunction with decreasing summer insolation (Laskar et al. 2004) may have reinforced sea ice conditions and caused more continental, longer winters at 3–1 ka b2k (Werner et al. 2016).

Terrestrial proxies parallel this long-term oceanic surface cooling, but in a more abrupt and complex manner, probably reflecting varying response of smaller systems with different thresholds to this climate deterioration. Thereby, transition of vegetation dominated by S*alix polaris* to arctic tundra vegetation with *Dryas octopetala* occurred on Kapp Linné between 6.5 and 4.5 ka b2k, with associated cooling and drying (Birks 1991, Alsos et al. 2016). Similarly, in the period 4.5–4.3 ka b2k, glacier reformation is documented around Linnévatnet by Svendsen and Mangerud (1997) and Reusche et al. (2014), and in NW Spitsbergen by van der Bilt et al. (2015). However, Svalbard glaciers display a truly complex behaviour in reaction to external forcing, exacerbated by the internal glacier dynamics and surge advances (Kempf et al. 2013, Farnsworth et al. 2017). Consequently, fluctuations of many glaciers are asynchronous especially, but not exclusively, in the earlier parts of the Neoglaciation (Solomina et al. 2015).

The onset of Neoglacial coincides with the lower part of Biozone B in Garmaksla record, at ~4.6–3.8 ka b2k, and is characterised by a sudden reorganization of the lake ecosystem. Hitherto dominant *A. affinis* is substituted by a diverse assemblage of diatoms, including *S. venter*, which over time establishes itself as the most resilient species at ~3 ka b2k. This was, however, preceded by a period of intense inter-species competition and

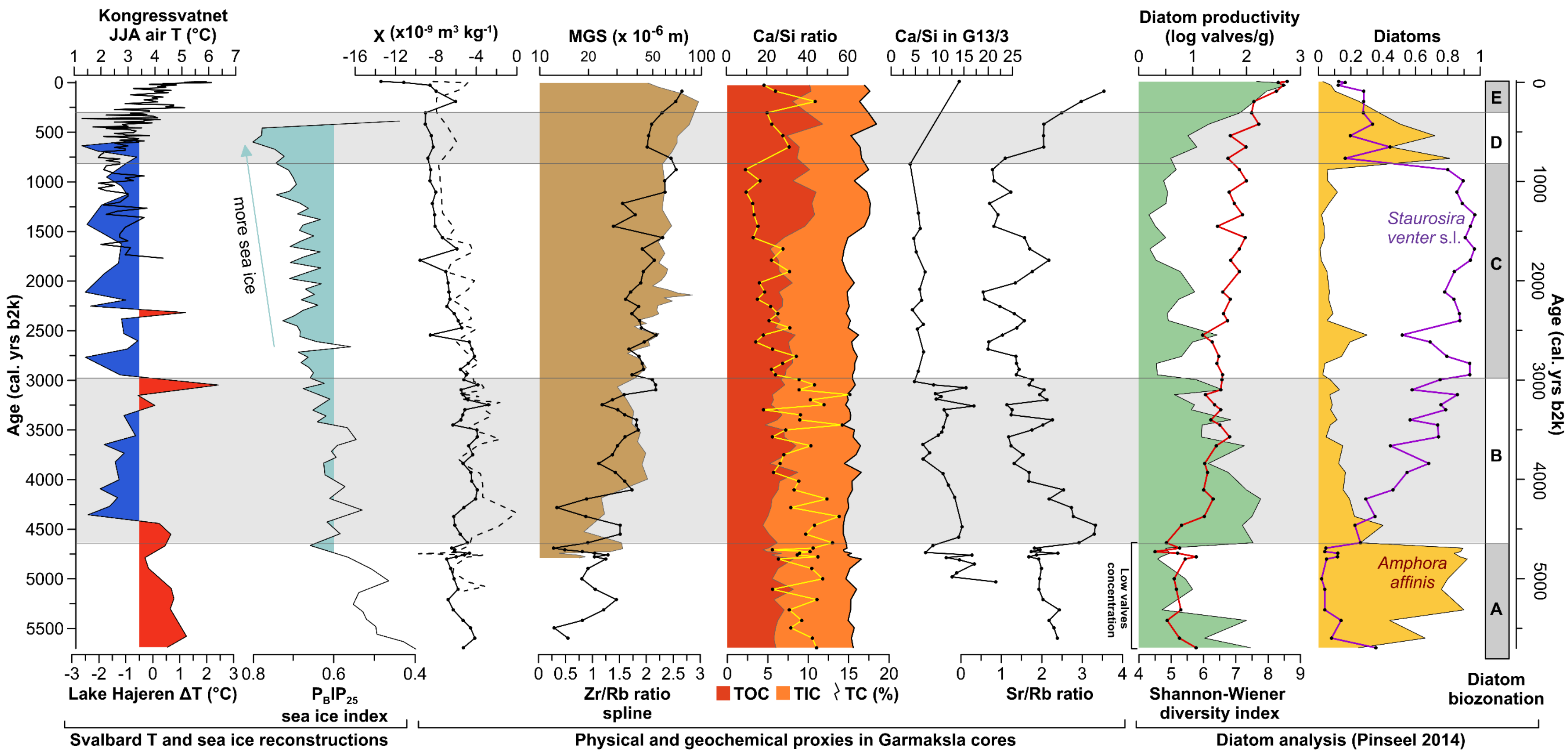

Figure 6.8 Comparison of palaeoenvironmental reconstructions around Svalbard with the sedimentary record of Garmaksla plotted on age scale. From left: Alkenone based reconstructions of summer air temperature in Kongressvatnet for the last 1.8 ka (D'Andrea et al. 2012; black line) and Lake Hajeren (van der Bilt et al. 2016; red-blue fill); P_BIP_{25} index of sea ice conditions near the continental margin off Svalbard coast in Fram Strait (Müller et al. 2012); Garmaksla cores: magnetic susceptibility (χ) in cores G13/1 (solid line) and G13/3 (dotted line); mean grain size (MGS) in µm in core G13/2 (solid line) and Zr/Rb ratio as proxy for grain size in G13/3 (light brown fill); total organic (TOC; red fill) and inorganic (TIC; orange fill) carbon content in % and Ca/Si ratio as proxy for carbonates (yellow line with black dots) in G13/1; Ca/Si ratio in G13/3; Sr/Rb ratio as proxy for detrital input/weathering; Diatom analysis (from Pinseel 2014): diatom productivity (expressed as decadic logarithm of valves counts per 1 g of dry sediment; green fill) and Shannon-Wiener diversity index (red line); relative abundance of two dominant species mesotrophic *Amphora affinis* (orange fill) and more oligotrophic *Staurosira venter* s.l. (violet line); Diatom biozonation based on broken-stick analysis.

concomitant increased biodiversity (Pinseel 2014). Interestingly, also bryophyte diversity increases in this period, with presence of several species of *Warnstorfia*, including *W. pseudostraminea*, thriving in periodically inundated habitats (Bernardová, unpublished data). Ca/Si and Sr/Rb ratios markedly fluctuate and reach above average values, indicating thus periods of carbonate precipitation. Together these proxies suggest highly variable lacustrine conditions with substantial lake level changes, promoting growth of mosses in the littoral and carbonate authigenesis.

The transition of Zones A/B (~4.6 ka b2k at Garmaksla time-scale) corresponds to large-scale cooling of the region, probably coeval with cooling at ~4.4 ka b2k described by van der Bilt et al. (2016) and other aforementioned events at ~5–4 ka b2k related to changes in oceanic circulation. At around this time, increased production of sea ice from the Arctic Ocean reached seasonally the west coast of Svalbard (Werner et al. 2013), including Isfjorden and other Spitsbergen fjords (Rasmussen et al. 2013). Onset of cold summers and winters probably lowered the threshold for reestablishment of glaciation (Reusche et al. 2014, van der Bilt et al. 2014), although glacier advances were mostly short-lived due to possible moisture starvation (Balascio et al. 2017). Nonetheless, weak stratification of the adjacent seas and only seasonal export of sea ice from the Arctic Ocean possibly ensured ice-free summers (Werner et al. 2013), even in Billefjorden (Baeten et al. 2010). Therefore, summer precipitation might have not been greatly reduced, and yet glaciers were starved of solid precipitation (de Wet et al. 2017). Even so a few glaciers advanced (van der Bilt et al. 2015, Miller et al. 2017), but these may be only sporadic random surges resulting from previous long-term mass accumulation (Farnsworth et al. 2017).

Persisting pronounced seasonality and high summer-to-early-autumn 24h insolation (Laskar et al. 2004) meant that ice cover of Garmaksla could melt during summer, and the exposed water surface may have absorbed more incident solar radiation. Relatively strong, dry advective winds on days with positive net radiation could induce substantial evaporation even in generally cold climate (Láska et al. 2013, Leppäranta et al. 2017). Yet, seasonally open seas conveyed certain moisture. I argue that these regional predispositions resulted in fluctuations of water level, shifts in biological communities and increased carbonate precipitation. Correlation of these sudden changes with other events at ~4.5–3 ka b2k such as later fleeting warming in Lake Hajeren record, perhaps a reflection of 2.8 ka event (Fig. 6.8; van der Bilt et al. 2016) or other lakes on the west coast of Spitsbergen (de Wet et al. 2017, Gjerde et al. 2017) is, however, in my opinion, unattainable. These other lakes are located much closer to the intersection of West Spitsbergen Current and Arctic Polar waters, making them sensitive to any oscillations thereof (Werner et al. 2016), whereas Garmaksla Lake experienced much more continental climate with pronounced seasonality. This behaviour might be unique with respect to other records hitherto observed on Svalbard, and more representative of large inland areas with vast ice caps.

Subsequently, Garmaksla Lake reached a new state at ~3 ka b2k with the onset of lamination (Zone C). *S. venter* was firmly established and biodiversity of both diatoms and mosses reached the absolute low (Pinseel 2014, Bernardová, unpublished data). Decreasing seasonality and even colder summers ensued in multiannual ice cover, possibly lasting for several years or even decades. Aeolian dust and sand accumulated on the ice cover, and only during warm summers, when the ice melted, was released and deposited on the lake bottom (Lamoureux and Gilbert 2004, Cuven et al. 2010). During the frozen phase, lake biota probably survived, since there is no indication of hiatus, diatom assemblage shifts, or bioproductivity decline (Pinseel 2014). The lake ecosystem might have acquired nutrients from thawed moat at the lake perimeter, or through primary productivity, provided the lake was covered with black ice and little or no snow cover (Wetzel 2001, de Wet et al. 2017). Signs of amelioration are apparent e.g. at ~2.5 ka b2k as a spike of *A. affinis* or by TOC increase after 1.5 ka b2k. The latter event, concurrent with increase of TIC, Ca/Si and Sr/Rb, and *A. rosenstockii* might imply respiration exceeded photosynthesis, hypothetically due to decrease in light availability (perhaps more snowfall or stronger winds disrupted formation or transmissivity of black ice).

Baeten et al. (2010) assume that Billefjorden was permanently covered by shore-fast ice between ~3.2 and ~0.1 ka b2k. Sea ice progressively enveloped Svalbard and pervaded also into the fjords (Müller et al. 2012). However, despite the lowest sea surface temperatures occurring in this period, intensified subsurface advection of Atlantic warm waters is reported west of Spitsbergen including Isfjorden after ~3 ka b2k (Hald et al. 2007, Rasmussen et al. 2013, Werner et al. 2016). Behaviour of these two water masses was thus decoupled mainly due to density differences (Werner et al. 2013). Strong pycnocline separating these two water masses probably blocked heat release from Atlantic waters, which resulted in the most severe Holocene cooling in the region (Werner et al. 2016, van der Bilt et al. 2016). Decline in summer temperatures and correspondent shorter ablation period are considered as likely triggers of glacier advances (Miller et al. 2017). Most glaciers advanced after 2 ka b2k (Solomina et al. 2016) and those located in the southwest of Spitsbergen reached their Holocene maxima already between 2 and 1.5 ka b2k (Reusche et al. 2014, Philipps et al. 2017). Apart from that, the whole region was in a state of 'hibernation', with very few glaciological, oceanographic or biological processes (freeze-thaw and aeolian processes may constitute an exception).

Further invigorating of Atlantic water inflow and simultaneous growth of sea ice extent resulted in very instable, but generally warming oceanic conditions after 2 ka b2k (Rasmussen et al. 2014). In principle, the same process responsible for warming detected in marine cores (Rasmussen et al. 2014, Werner et al. 2016) and lacustrine records after ~1 ka b2k (D'Andrea et al. 2012, Balascio et al. 2017, this study) may have also caused the maximum Holocene glacier advances on Svalbard (Solomina et al. 2016). At least for the massive ice caps and glaciers, thermal history may play an important role upon receiving substantial mass of solid precipitation, since it retards the effects of concomitant warming. Therefore, the most (especially marine-terminating) glaciers on Svalbard reached their Holocene, Neoglacial and LIA maxima at the end of the 19th or by the beginning of the 20th centuries (Rachlewicz et al. 2007, Baeten et al. 2010, Błaszczyk et al. 2013).

The response of Garmaksla Lake ecosystem is somewhat more complicated and therefore elusive. Reoccurrence of *A.affinis* and *C. richardsonii* at ~0.8 ka b2k and ongoing increase in diatom productivity and biodiversity may signify a return to warmer or mesotrophic conditions (Pinseel et al. 2014). Diatom shifts at this period, however, usually mark the onset of LIA (Jones and Birks 2004). Furthermore, the laminae were still forming until ~0.3 ka b2k, when also chironomid assemblage significantly reacts to warming (Vondrák, unpublished data). This is comparable with findings of Brooks and Birks (2004) and Luoto et al. (2014). It is not certain if peak of sand content and MGS corresponds to influx of coarse particles, or whether its source is biogenic (e.g. by expansion of diatoms with large valves and large chironomid species, or lessser degradation of detritus). Increase of Ca/Si and Sr/Rb ratios may indicate resumed carbonate precipitation, hence increased photosynthesis or light availability. To summarize the evidence, zone D may correspond to more unstable period during the LIA with unstable atmospheric circulation and variable, albeit at least occasionally warmer, conditions. Transition of zones D to E then corresponds to the most recent shift of diatom communities observed on Svalbard (Pinseel 2014), possibly anthropogenically influenced (Holmgren et al. 2010). Many authors, however, place this transition later into the 20th century (Guilizzoni et al. 2006, Jiang et al. 2011). Hopefully, more detailed chironomid and bryophyte stratigraphy will provide clues on the final determination of this last detected stage in Garmaksla Lake history.

VI.3.2 Jarfjorden, northern Norway

Considering that so far only dating and analyses of abiotic proxies were undertaken in Jarfjorden lake records, the presented Middle to Late Holocene palaeoenvironmental reconstruction is rather tentative. However, as shown in Chapter VI.2.2, close correspondence between several independent lines of evidence revealed notable fingerprints of environmental and limnological changes in the sedimentary archive.

The oldest recorded period 8–6.5 ka b2k (possibly up to 4.5 ka b2k), characterised by higher accumulation rates, very low χ and elevated Fe/Mn ratio (Fig. 6.9), is interpreted as a phase of increased accumulation of autochthonous organic matter and decomposition, reflecting higher aquatic bioproductivity and possibly more favourable climate (Snowball 1993). This period corresponds to inferred HTM in Fennoscandia (Birks and Seppä 2010, Sejrup et al. 2016), when mean summer air temperatures were ~1.5–2.5 °C higher relative to present, as documented by vegetation dynamics (Solovieva et al. 2005, Allen et al. 2007, Jensen and Vorren 2008), changes in subfossil assemblages of diatoms (Rantala et al. 2015) and aquatic organisms (Korhola et al. 2002, Sarmaja-Korjonen et al. 2006, Ilyashuk et al. 2013, Luoto et al. 2014b), or glacier retreats (Wittmeier et al. 2015, Jansen et al. 2016). The climate was generally more continental between 9 and 4 ka b2k, so despite longer and warmer summers and higher precipitation totals, winters were probably colder and precipitation-evaporation balance declined (Allen et al. 2007). Decreased effective moisture led to general lowering of lake levels, predominantly in hydrologically closed basins (Korhola et al. 2005, Rantala et al. 2015), sometimes resulting in complete desiccation of shallow lakes (Sarmaja-Korjonen et al. 2006). Exact timing and amplitude of peak Holocene warmth are nonetheless difficult to constrain more definitely owing to different sensitivity and response times of various biological proxies (Shala et al. 2017). Chironomid-based summer temperature reconstructions thus imply maximum warming in the Early Holocene (Luoto et al. 2014b, Shala et al. 2017), whereas pollen-based reconstructions (possibly reflecting delay of post-glacial tree succession and migration; Väliranta et al. 2015) and other reconstructions are in accordance with the paradigm of the Mid-Holocene Thermal Maximum (Birks and Seppä 2010, Shala et al. 2017).

If there are uncertainties in age, duration and amplitude of HTM across Fennoscandia, even greater doubts concern the subsequent climatic development, beginning by ~4–5 ka b2k, i.e. during the Middle–Late Holocene transition (Walker et al 2012). In general, gradual cooling and moistening of climate took place in northern Fennoscandia after 4 ka b2k (Birks and Seppä 2010). This is documented by glacier advances and lowering of equilibrium line altitude in coastal Finnmark with the onset of the Neoglacial between 4 and 2 ka b2k (Bakke et al. 2005, Wittmeier et al. 2015, Jansen et al. 2016), lowering of treeline altitude in the Scandes (Karlsson et al. 2007, Jensen and Vorren 2008), as well as in a multitude of palynological and lacustrine biological proxies (Solovieva et al. 2005, Allen et al. 2007, Ilyashuk et al. 2013, Luoto et al. 2014b, Rantala et al. 2015), including rising lake levels (Korhola et al. 2005, Sarmaja-Korjonen et al. 2006, Rantala et al. 2015). Moistening and invigorating of the atmospheric circulation probably induced substantial changes in lake mixing regimes, which is documented in shifts of diatom assemblages across Fennoscandia (Rantala et al. 2015). In a shallow lake Várddoaijávri (150 km west of Jarfjorden), Rantala et al. (2015) found re-emergence of heavy planktonic diatom *Aulacoseira italica*, which necessitates deep and more turbulent waters to stay in the water column. This shift towards more efficient vertical mixing induced probably by stronger winds occurred at 4.2 ka b2k (Rantala et al. 2015).

Increased mixing of water column is registered in shift from anoxic to oxic conditions, as inferred from lower Fe/Mn, that occurred at ~4.2 ka b2k also in Holmvatnet (Fig. 6.9). However, redox conditions in Langvatnet do not follow the same trend as in KH2. Possibly, different locations of coring points in respect to lake basins morphometries may explain such discrepancy. Core KH2 was drilled in an embayment, not in the deepest part of the lake basin. Invigorated water mixing of the hypolimnion may have shifted the anoxic layer deeper into the lake (Boehrer and Shulman 2008). On the other hand, a very deep Langvatnet was cored near the depocenter, from where the anoxic hypolimion could not relocate any lower. The subsequent increase in Fe/Mn could be attributed to variations in deposition of organic matter or primary productivity, or it may simply reflect the input of Mn-depleted ferrimagnetic minerals (Snowball 1993, Wetzel 2001).

In Jarfjorden geochemical record, gradual, synchronous rise of Rb/Sr ratio might mirror increasing contribution of chemically weathered material to the overall detrital input into the lakes (Xu et al. 2010, Fernández et al. 2013). More intensive chemical weathering necessitates more water available in the catchment and thus may imply progressive increase in effective moisture or precipitation (Fernández et al. 2013), or alternatively greater depth of active layer. On the other hand, Allen et al. (2007) argue that chemical weathering contrarily dominated during HTM owing to warmer temperatures, whereas higher snow cover in winter offered better protection of the bedrock and glacial drifts from freeze-thaw cycles and reduced thus effectivity of mechanical weathering (Allen et al. 2007). Therefore, the relationship between relative abundance of Rb and Sr content and chemical weathering

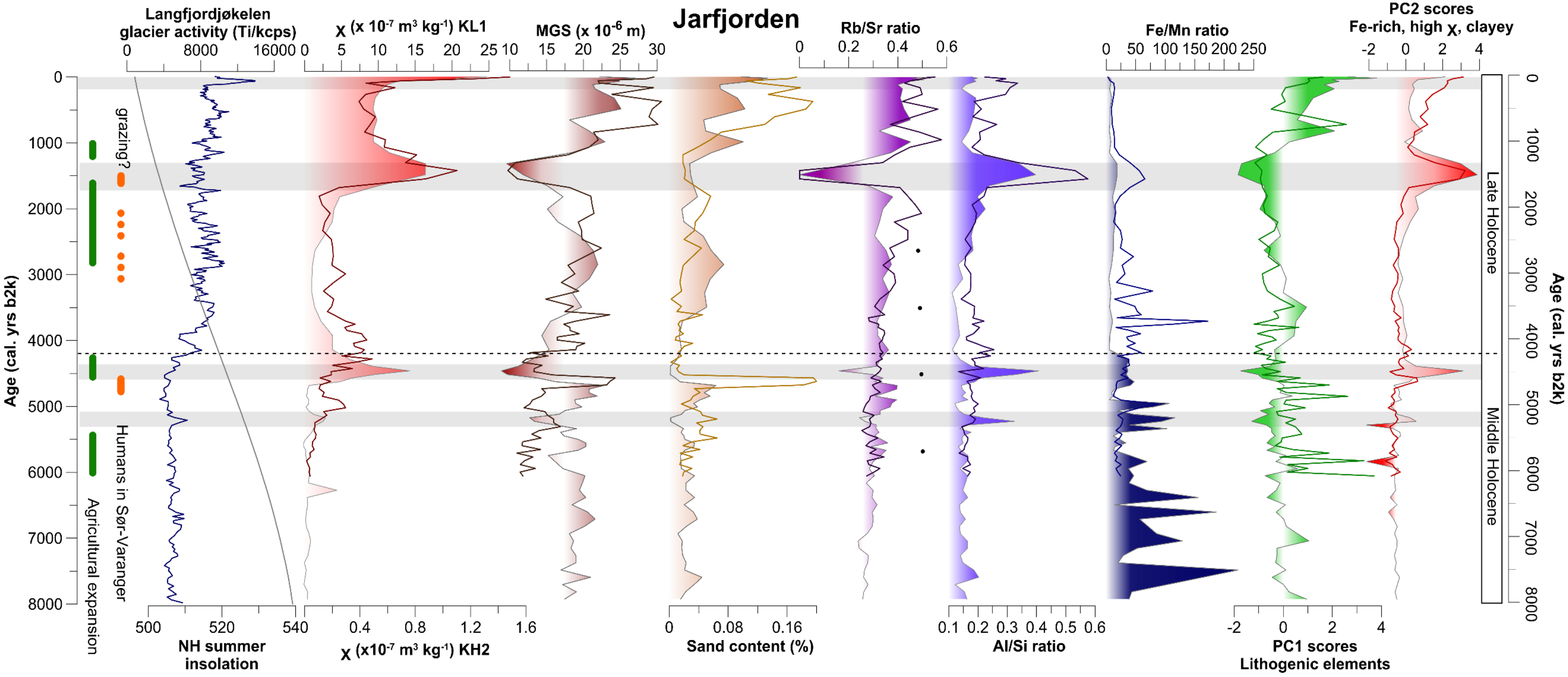

Figure 6.8 Comparison of regional palaeoenvironmental and archaeological evidence with Jarfjorden lacustrine record: Periods of agrarian expansion (Sørensen 2014) and indication of human presence in Sør-Varanger (for references see the main text); July insolation at 69°N (grey line; Laskar et al. 2004); activity of Langfjordjøkelen glacier as inferred from Ti counts proxy in sedimentary record of Lake Jøkelvatnet (71°N, 22°E; blue line; Wittmeier et al. 2015); Jarfjorden sedimentary record (from left, filled lines refer to core KH2, simple lines to KL1): magnetic susceptibility (χ), mean grain size (MGS), sand content, XRF element ratios of Rb/Sr, Al/Si, and Fe/Mn, and first and second PCA scores.. Grey bars indicate periods of sudden shifts in conditions of the lake catchments, probably vegetation reduction and increased erosion.

is complex and may be strongly influenced by the catchment area and lithology, leading actually to inverse behaviour of Rb/Sr ratio on different temporal and spatial scale relative to intensity of chemical weathering (Xu et al. 2010). The significance of parallel increase in Rb/Sr ratio would thus deserve more attention and examination by advanced geochemical methods. Prominent trough in Rb/Sr ratio at 1.5 ka b2k is probably not related to climate, but rather to mineralogical or textural changes of the sediment associated with increase in χ and clay (Xu et al. 2010, Hošek et al. 2015).

By the end of the Mid-Holocene, both sedimentary records seem to reveal incipient soil/regolith erosion in the catchments. The first two peaks at ~5.2 and ~4.5 ka b2k bear the diagnostic signs of these events (i.e. high χ, clay and Fe content, Al/Si ratio), although of smaller magnitude than the peak at 1.5 ka b2k. Allen et al. (2007) argue that increased erosion of glacial deposits followed the opening of vegetation after 4.6 ka b2k. This period is generally characterized by greater environmental variability and instability in Fennoscandia (Allen et al. 2007, Wittmeier et al. 2015). It is therefore possible that climatic deterioration led to a chain of events that enabled more effective erosion and transport of top soils or regolith (Snowball et al. 1993, Virkanen 2000). Although no studies trace the exact shifts of northern tree line and forest line during the Holocene in Jarfjorden, and considering the present configuration of taiga-tundra ecotone, it is likely that pine and birch forests extended to the Jarfjorden area during HTM (Allen et al. 2007, Hofgaard et al. 2013). In accordance with summer cooling and moistening during the onset of Neoglacial, forest lines may have migrated southwards, which resulted in greater erodibility of the substrate. Destabilization of soils following deforestation was documented elsewhere (Hammarlund et al. 2004, Reuss et al. 2010), although the timing of forest line retreat differs based on the exact location of boundary between the biomes, altitude and topography. Observed peaks in Jarfjorden cores, therefore, cannot be easily correlated to other records.

Uncertainty in linking the detected events to climatic and environmental fluctuations rises a possibility of direct or indirect anthropogenic influence. Several authors attribute the forest retreats to human disturbances (Virkanen et al. 2000, Karlsson et al. 2007, D'Anjou et al. 2012) or to grazing by domesticated reindeer herds (Vorren 1983 in Helskog 1984, Andersen 2011). Archaeological evidence moreover indicates humans were present near Kirkenes at 5–4.5 ka b2k (Helskog 1984), in the period of general agrarian expansion in Fennoscandia (Sørensen 2014). The episode of erosion might have been therefore induced by human activities in the Jarfjorden area, or by a synergic effect of anthropogenic and climatic impact on the considered catchments.

Both sedimentary profiles display a similar, stationary trend between ~4 and 1.8 ka b2k, pointing to stable conditions. Another marked episode of catchment erosion, however, occurred at ~1.5 ka b2k. Several palaeoenvironmental reconstructions associate this period with deteriorated climate in northern Fennoscandia, as inferred from $\delta^{18}O$ from speleothems in Søylegrotta cave (Lauritzen and Lundberg 1999), or chironomid-based summer temperature reconstructions (Luoto et al. 2014a, Rantala et al. 2014). Numerous glacier advances between 1.8 and 1 ka b2k (Bakke et al. 2005, Wittmeier et al. 2015, Solomina et al. 2016) manifest increased oceanic influence as stronger westerlies bring more winter precipitation also to the northern Scandes (Bakke et al. 2008). Relatively colder conditions of the Migration period (1.85–1.3 ka b2k) are also indicated by dendroclimatological reconstruction of summer temperatures using late wood density of pines (Esper et al. 2014). These events, however, are often stretched over a wide period and sometimes do not display such a pronounced peak as in Jarfjorden lakes. The distinct peak, on the other hand, probably marks crossing of a threshold value, after which erosion drastically accelerated. Whether this was caused by further opening of the vegetation cover, at this time probably retreat of birch tree line (Hofgaard et al. 2012), is debatable. Human influence, however, should be again considered in this case. Evidence of reindeer grazing was asserted directly from the Jarfjorden area at ~1.5 ka b2k (Vorren 1983 in Helskog 1984). Catchment vegetation thus might have been disturbed by intensified grazing and trampling, and owing to adverse climatic conditions, the former vegetation might have not been able to recolonise the area (Allen et al. 2007), which is reflected in ongoing moderate rates of erosion from 1.5 ka b2k until present. A similar development was assessed further west on the Lofoten Islands, where the peak deforestation and grazing coincided with the maximum of Iron Age population (D'Anjou et al. 2012).

Following the episode of erosion, a considerable increase of sand grains suggests increased aeolian activity in colder and drier climate. Sparse vegetation cover and less snowfall would facilitate deflation and transport of sand and silt to the lake ice cover (Allen et al. 2007). Suitable material for aeolian transport might have been supplied by intensive periglacial processes. The final increase of χ in the last 70 yrs, coincident with accelerated deposition of Ni and Cu, marks the onset of contamination by industrial aerosols and SO_2 from the newly established smelters in the close proximity to the catchments. The industrial complex causes damage to sensitive boreal ecosystems of the Norwegian-Russian boundary, as evident by acidification and visible injuries of plants (Myking et al. 2009, Rognerud et al. 2013).

VI.3.3 Kobbefjord, southwestern Greenland

Sedimentary profiles from Kobbefjord record ~800 years of lake evolution and sedimentation that was nevertheless regulated by ongoing climatic changes. Progressive Neoglacial cooling culminated in the LIA (globally ~750–150 years b2k; D'Andrea et al. 2011), but was marked by several fluctuations, probably related to Medieval Climate Anomaly. Favourable climatic conditions peaked in the West Greenland around 1150–750 years b2k, coinciding with establishment of the Norse settlement (D'Andrea et al. 2011, Ribeiro et al. 2012, Massa et al. 2012). Glaciers and ice caps in other catchments of Kobbefjord area steadily retreated since ~1.4 ka to 850 yrs b2k (Larsen et al. 2017). This trend was reversed by a significant cooling that occurred afterwards, around 800–600 yrs b2k (Fig. 6.10), as inferred from marine (Seidenkrantz et al. 2007; Sha et al. 2011) and lacustrine records (D'Andrea et al. 2011). Also, the main GrIS margin ~100 km to the northwest of Kobbefjord reached a maximum position during a minor re-advance at at ~550 yrs b2k (Levy et al. 2017). Zone 1 in core L4 corresponds to this period of cooling and exhibits moderate accumulation rate of terrigenous, mainly clastic matter (low TC and TN, slightly elevated C/N, high Sr/Rb, overall low accumulation rate), turbulent water column and oligotrophic conditions (low productivity and diversity, diatom assemblage including *A. tethera and B. brebissoni,* Fig. 9.5). The upper studied lake was less productive at that time, as the regional climate cooled, a shift reflected in very low chemical weathering (high Sr/Rb). These rather cold conditions correspond to inferred period of significant cooling at ~960–680 yrs b2k described by D'Andrea et al. (2011), which probably contributed to the abandonment of the Norse Western Settlement at ~700–650 yrs b2k. Aridity pulse accompanied this cold period, as documented by an increase in aeolian dust deposition (Møller et al. 2006; Anderson et al. 2012) and low snow accumulation rate on GrIS (Andersen et al. 2006). This may explain the discrepancy between high Sr/Rb and low Si/Zr, proxy for grain size, in core L4: physical weathering dominated, but arid conditions permitted transport of a limited amount of rather fine-grained material to the lake basin.

Lake and climatic conditions ameliorated in the period ~500–350 yrs b2k (Zone 2a). Accumulation rate, Si/Zr and Sr/Rb remained low, χ and MGS kept steady values. Diatom diversity increased, and so did the productivity and TC in the latter part of Zone 2a. Biogenic silica exhibits the most prominent peak from the whole record ~450 yrs b2k. This is in agreement with improved limnological conditions in Kangerlussuaq lakes (D'Andrea et al. 2011) and in Southern Greenland (Kaplan et al. 2002; Millet et al. 2014) that prevailed at ~550–330 yrs b2k. Marine core from west of Kangerlussuaq also indicates cessation of extremely cold sea-surface conditions at ~425–340 yrs b2k (Sha et al. 2011). Other marine records, however, diverge during this period: either no warming is recorded (Ribeiro et al. 2012), or occurs too early to correlate with this event (short-term warming is recorded at ~570 yrs b2k in the Ameralik fjord core; Seidenkrantz et al. 2007). Around this time predominantly positive NAO switched into highly variable, often negative mode (Olsen et al. 2012, Ortega et al. 2015). Negative phases of NAO then coincide with warming events in the Greenland region (Fig. 6.10), including the one at the onset of Zone 2a. Temperatures inferred from Dye-3 borehole measurements (Dahl-Jensen et al. 1998), however, report opposite trend of continuous cooling from Medieval warm period until ~450 yrs b2k, and remain inconsistent with other records until ~250 yrs b2k.

Decline in biotic proxies (productivity, diversity, BSi and TC), increase of pH and dominance of *T. flocculosa* characterize subzone 2b (~370–270 yrs b2k), indicating colder, less productive waters. *Psammothidium* spp. is present throughout this subzone and together with higher MGS and Si/Zr implies greater influx of sand grains from the catchment due to intensification of hydrological processes. Sr/Rb does not follow increase in Si/Zr completely, which suggests enough moisture was available for efficient chemical weathering even despite lower temperatures. Additionally, C/N peak might mark sheet washing of terrestrial plants and/or soil erosion into the lake. In summary, proxies indicate colder, but also wetter climate for this period. The cooling, coinciding with the Maunder solar minimum (~350–285 yrs b2k), is mirrored again in records of D'Andrea et al. (2011), Millet et al. (2014) and winter temperatures inferred from δ^{18}O signal in GrIS ice cores (Vinther et al. 2003). Tidewater glacier Kangiata Nunaata Sermia (~80 km to the west of Kobbefjord) reached its mximum LIA position following this cold period (Pearce et al. 2014). Cooling in Greenland is, however, usually connected to drying, and some studies indeed record peak LIA aridity (Andersen et al. 2006).

Continuous climate deterioration leading towards regional LIA culmination in the second half of the 19th century (based on evidence from glaciers; Dahl-Jensen et al. 1998; Weidick et al. 2012) was interrupted by another brief warm interlude ~240–160 yrs b2k (Vinther et al. 2003, D'Andrea et al. 2011, Millet et al. 2014). The episode is again reflected in our record in Zone 3 by increased aquatic productivity, BSi and TC, and contrarily lower clastic input. Several indicators (presence of *F. oldenburgiana*, lowest inferred pH) suggest, however, only modest amelioration of lake temperature. Ensuing subzones 4a and especially 4b already document transition to the coldest and probably also the most humid period in our record. Diatom assemblages, BSi and TC imply oligotrophic conditions and low productivity, except for a brief period at the transition of subzones 4a and 4b with peak of clay content and lowest diatom diversity. Double maxima of MGS, Sr/Rb and Si/Zr are indicative of potent hydrological processes that are capable to entrain large amount of coarse clastic material. In subzone 4b these processes probably intensified, as the highest accumulation rates and χ suggest. The exact character of environmental conditions behind the invigoration of geomorphic processes in the catchment is difficult to disentangle. The period of interest (~150–80 yrs b2k), however, clearly experienced severe winters (Vinther et al. 2003, 2006) and sufficient precipitation for glacier advances (Weidick et al. 2012). Intensive rainfall events or rapid snowmelt may have resulted in greater material transport into the catchments (Lapointe et al. 2012).

Rapid infilling of the upper lake basin caused lowering of water depth and transition of the lake into present peat bog (Zone 1, ~80 yrs b2k until present). Diatom productivity and diversity further declined and BSi stagnated, whereas TC, TP, chrysophyte to diatom ratio (Smol 1985) and species *E. paludosa* and *Ch. hassiaca* significantly increased, implying development of organic-rich, oligotrophic environment (van de Vijver et al. 2004), overgrown by *Sphagnum*-dominated moss cushion. The last stage of the upper lake ontogeny occurred during the period of rapid warming in Greenland, culminating in the 20th century (Vinther et al. 2003, 2006). The environmental signal in core L4 is, however, probably obliterated by entire reorganisation of processes controlling the response of proxies to external forcing. Evidence of the current changes (after ~80 yrs b2k) thus cannot be extracted from the presented sedimentary record only, because of the inherent interrelationship of individual components that forms the complex climate-catchment-lake system (Anderson et al. 2012). Every sedimentary record should be investigated in respect to local climatic and catchment specific conditions, in order to detect interactions between the system components (McGowan et al. 2008). Accordingly, a difference between the main periods of infilling in the upper and lower lakes has to be stressed, and I hypothesise that the lower lake was largely infilled before the catchment filtering in the upper lake restricted downstream transport of entrained material, following the paludification and infilling of the upper lake (Anderson et al. 2012). Alternatively, the sedimentary dam of the lake L3 may have been breached, which would result in cessation of accumulation at the cored location Owing to this reason, sedimentary sequence from the lower lake was responding differently to external factors than the upper lake, even though they share a number of features in their proxy data.

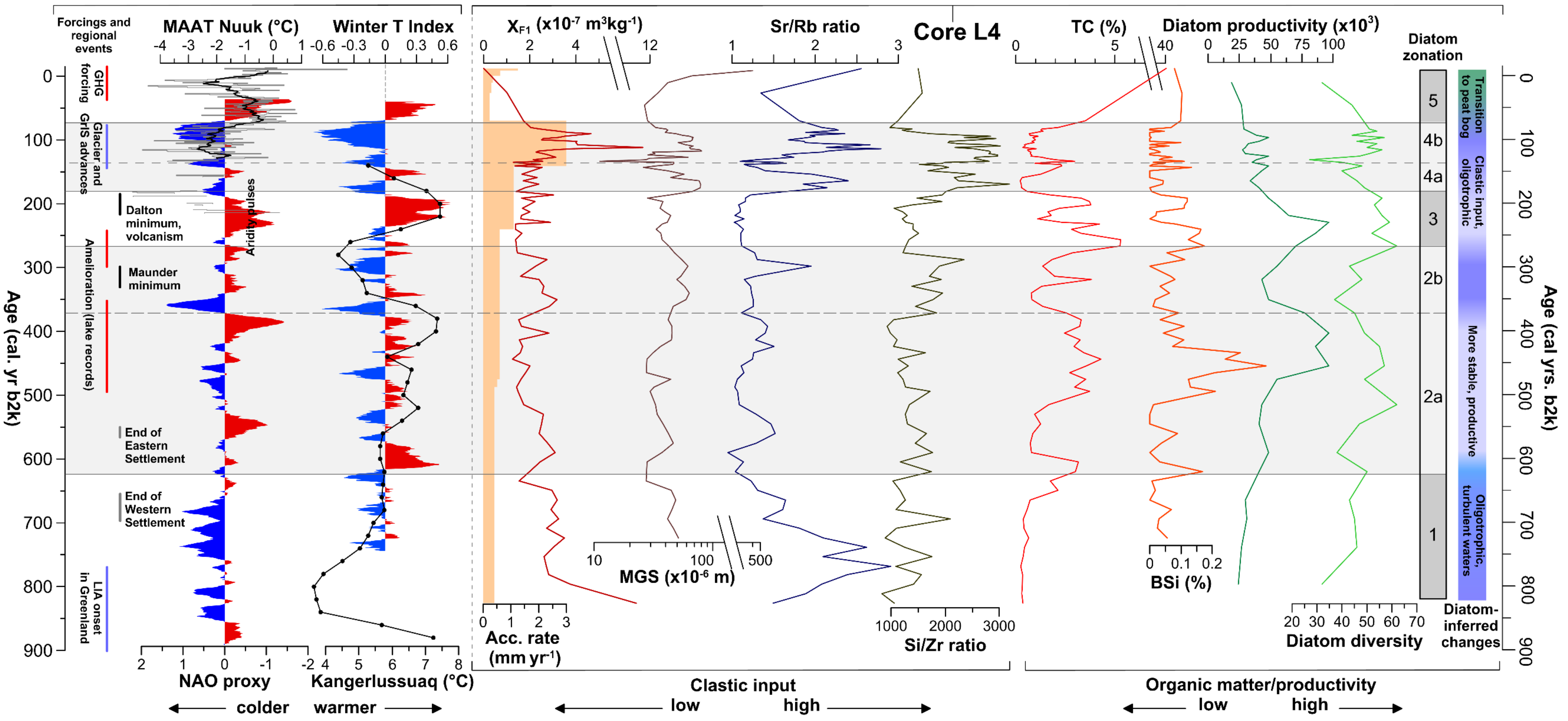

Figure 6.10 Comparison of regional environmental changes with selected proxies from the studied sedimentary profile L4. From left: Main climatic and regional events discussed in the text; mean annual air tepmerature (MAAT) record from Nuuk meteorological station (black line) with 11-yr running mean (grey) (Vinther et al. 2006); NAO index based on 48 terrestial and marine proxies from NH(Ortega et al. 2015); Southern Greenland winter temperature index reconstructed from stable isotopes in Greenland ice cores (Vinther et al. 2003); alkenone-based reconstruction of mid-summer lake water temperatures in two lakes of Kangerlussuaq area (D'Andrea et al. 2011); main proxies from core L4: accumulation rate, magnetic susceptibility (χ), mean grain size (MGS, Sr/Rb and Si/Zr ratios, total carbon (TC), biogenic silica (%), diatom productivity and diversity, main stages of lake ontogeny, and biozonation based on CONISS analysis (Chattová, unpublished data).

VI.3.4 Evolution and driving factors of Holocene climate in the North Atlantic region

On the Holocene timescale, the climate of the North Atlantic region was governed mainly by summer insolation, decreasing since 11 ka b2k and largely responsible for the early onset of HTM in the Arctic, but with preeminent modulation by oceanic and atmospheric systems (Miller et al. 2010a, Sejrup et al. 2017). Obliquity of the Earth's axis peaked at the beginning of the Holocene and signified greater total solar insolation to the high northern latitudes. Gradual decrease of incoming solar insolation by ~10 % due to decreasing obliquity of the Earth's axis (Laskar et al. 2004) was certainly substantial for the Holocene climate forcing, but the observed climatic changes rarely exhibit such linear, gradual trends. Changes in intensity of AMOC and modes of atmospheric circulation such as NAO or AO directly influenced the climatic patterns on millennial, centennial and shorter timescales (Vinther et al. 2003, Hald et al. 2007, Olsen et al. 2013, Rasmussen et al. 2014). Furthermore, presence of vast continental ice sheets on the European and North American continents long into the Holocene (remnants of Laurentide Ice Sheet melted away by ~6.8 ka b2k; Carlson et al. 2008) regulated atmospheric and oceanic circulation by i) topographic and albedo effects, ii) stable anti-cyclone persistence above the ice sheets, and iii) rapid releases of fresh meltwater into the oceans ('hosing'; Teller et al. 2002, Sejrup et al. 2016). For example, the final major outburst flood of ice-dammed Lake Agassiz at ~8.4 ka b2k caused disruption of thermohaline circulation in the region, ensuing in transient, but widespread cooling known as 8.2 ka event (Teller et al. 2002, Daley et al. 2011, Rasmussen et al. 2014). This prominent episode registered in a number of palaeorecords on the Northern Hemisphere was chosen as a suitable stratigraphic boundary between the Early and Middle Holocene stages (Walker et al. 2012). Variations in AMOC and transport of warm Atlantic waters to the north were in control of different timing of peak Holocene warmth, with more northern regions around Svalbard experiencing HTM already by ~10 ka b2k, whereas in other more southerly locations HTM occurred at ~6 ka b2k (Hald et al. 2007, Kaufman et al. 2009, Briner et al. 2016, Sejrup et al. 2016). Owing to the Arctic Amplification, the peak warmth in the North Atlantic also exceeded the mean global Holocene temperature anomaly (Fig. 6.11; Miller et al. 2010b, Sejrup et al. 2016).

The onset of Neoglaciation coincides with the Early-Middle Holocene transition at 4.2 ka b2k and signals profound changes in the North Atlantic region (Sejrup et al. 2016). Majority of proxy data in Fennoscandia and Svalbard exhibits cooling (e.g. Birks and Seppä 2010, Sejrup et al. 2016, van der Bilt et al. 2016), but precipitation patterns mostly differ. On Svalbard, polar air masses gain on dominance, which reduces the flux of moist warm air from the south (Balascio et al. 2016) and does not allow substantial advances of local glaciers despite the favourable cooler temperatures (van der Bilt et al. 2015, de Wet et al. 2017). Fennoscandia experiences, on the other hand, more oceanic climate with less pronounced seasonality after ~4.2 ka b2k (Allen et al. 2007, Bakke et al. 2008). This is mainly documented by rising lake levels (Luoto et al. 2011) and glacier advances (Wittmeier et al. 2015). However, absolute precipitation totals likely decreased (Allen et al. 2007), as the predominantly snow-bearing winter westerlies decreased its activity (Bakke et al. 2008). Climate of Greenland exhibits bipartite behaviour, since the eastern side of the island closer

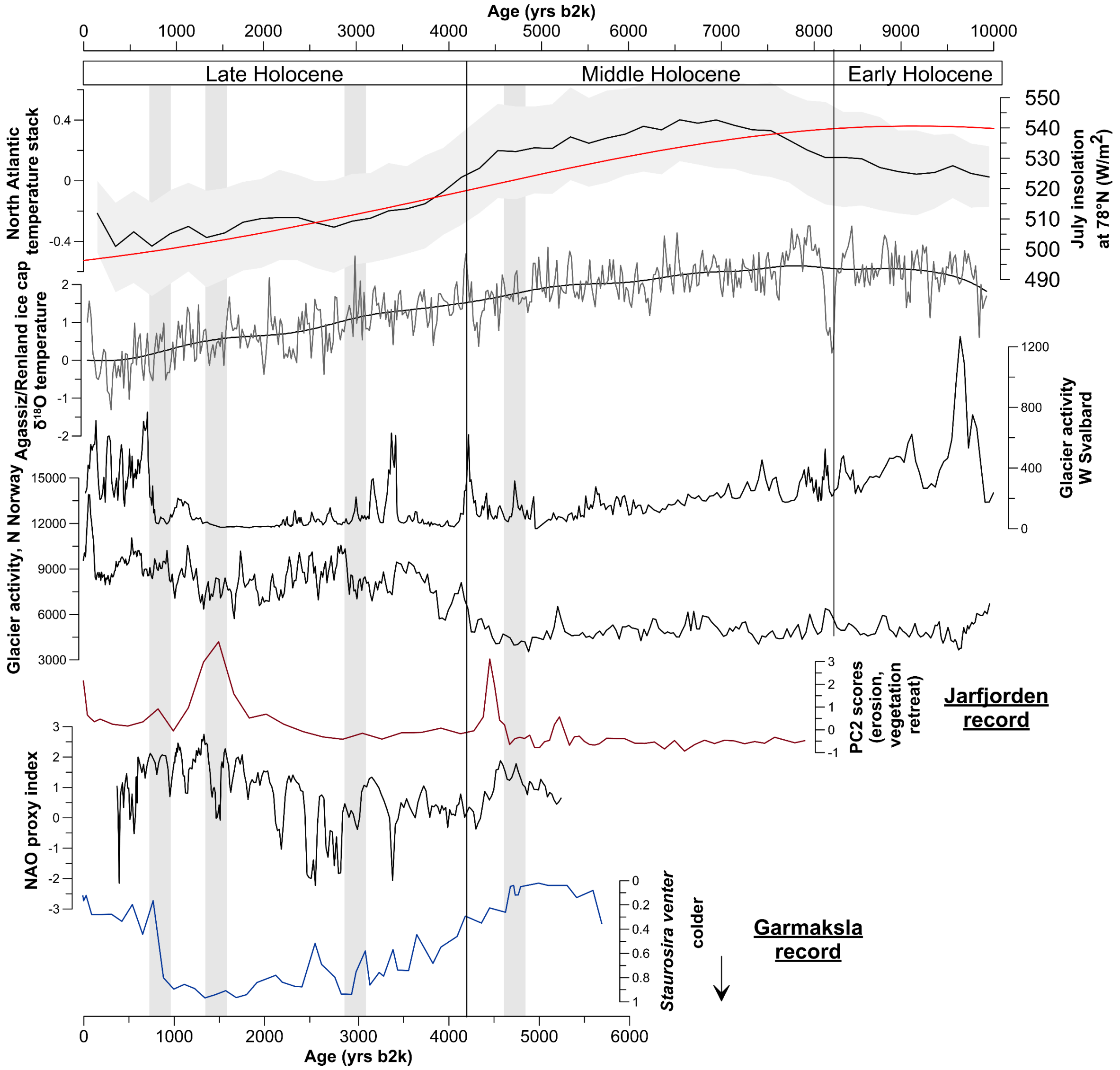

Figure 6.11 Proxy records from North Atlantic region: Incoming July insolation at 78°N (red line; Laskar et al. 2004); stack of marine and terrestrial Holocene temperature reconstruction from northern North Atlantic and Fennoscandia (Sejrup et al. 2016), δ^{18}O temperature difference from Renland and Agassiz ice caps, northern Greenland corrected for uplift (Vinther et al. 2009); glacier activity based on Ti/LOI and Ti counts profiles from sedimentary records of distal glacier-fed lakes Hajeren, Svalbard (van der Bilt et al. 2015), and Jøkelvatnet, northern Norway (Wittmeier et al. 2015); Jarfjorden record based on PC2 score of erosional activity and changes of vegetation cover in the catchment; NAO index from W Greenland lake (Olsen et al. 2012); abundance of *S. venter,* indicating colder conditions from Garmaksla sedimentary record.

to the North Atlantic experiences cooling (Briner et al. 2016), whereas some records on the western coast express significant warming (D'Andrea et al. 2011) or delayed final stages of HTM until ~3 ka b2k (Seidenkrantz et al. 2007). The GrIS reached its minimum extent by ~4 ka b2k (Larsen et al. 2015).

The emanating pattern of the Neoglaciation in the North Atlantic bears the AMOC signature with substantial modulation by NAO (van der Bilt et al. 2016, Werner et al. 2013). The underlying cause for changes of AMOC at Mid-Late Holocene transition, however, seems to emanate from the Arctic Ocean. By ~5 ka b2k, the final stage of post-glacial sea level rise, possibly in conjunction with glacioisostatic collapse of forebulge of the Barents-Kara Ice Sheet, caused flooding of the northern Eurasian continental shelves (Werner et al. 2013). Larger area available for sea ice cover thus accelerated drift ice formation. Concurrently, reorganization of the Arctic Ocean circulation changed the directions of Transpolar Drift and Beaufort Gyre, which ultimately increased export of drift sea ice through Fram Strait (Werner et al. 2013). The polar front reached Svalbard after 5 ka b2k and caused seasonal freezing of waters encircling the archipelago (Rasmussen et al. 2012, Werner et al. 2013). By this time, subsurface inflow of Antarctic waters to Svalbard continental slope weakened, thus resulting in weak stratification of the ocean column, export of sea ice and short ice-free summers (Rasmussen et al. 2013). On Svalbard, however, air temperatures possibly reached Holocene minima (van der Bilt et al. 2016). The cooling around 4.5 ka b2k is detected in various forms in records from Svalbard and northern Norway presented in this thesis.

Between 4 and 2 ka b2k, multi-centennial trend of NAO was mostly negative, which is supported by Late-Holocene reconstructions from Greenland (Olsen et al. 2012) and Fennoscandia (Bakke et al. 2008). Decadal variability of NAO seems to be the most prominent factor of atmospheric circulation in the North Atlantic (Ortega et al. 2015). Positive NAO anomalies are associated with northwards shifts of storm tracks (i.e. atmospheric cyclones) and increased storminess and winter precipitation in Fennoscandia (Bakke et al. 2008). Furthermore, positive phases of NAO correspond with advection of warm Atlantic waters to Svalbard continental shelf and reduction of sea ice extent, although discerning the cause and consequence is difficult (Müller et al. 2012). Greenland thus during negative NAO phases between 4 and 2 ka b2k periodically experienced warmer climate (D'Andrea et al. 2011, Olsen et al. 2012), whereas Fennoscandian climate became more continental and generally colder due to ingressions of polar air masses (Allen et al. 2007).

The last 2 ka around Svalbard experienced alternating influence of subsurface warm Atlantic waters and surface Arctic waters and fresh glacier meltwater (Rasmussen et al. 2013). In general, however, AMOC seems to have strengthened and positive NAO, associated e.g. with Medieval Climate Anomaly, prevailed (Bakke et al. 2008, Ortega et al. 2015). Advection of heat thus may have increased atmospheric moisture and nourished the cryosphere, which conversely increased meltwater flux to the ocean, intensified water stratification and decelerated the heat transfer (Müller et al. 2016, de Wet et al. 2016, Werner et al. 2016). Freshwater forcing together with insolation changes thus bonds in a complex feedback mechanism, resulting in unstable conditions of the last two millennia (Rasmussen et al. 2013, Werner et al. 2016). Greater release of meltwater from large ice sheets (such as from Laurentide Ice Sheet in the Early Holocene) or generally just greater land ice mass is therefore inversely proportional to AMOC strength (Sejrup et al. 2016). This is important with regard to Greenland, as will be shown further

AMOC is closely related to Atlantic Multidecadal Oscillation (AMO), or sea surface temperature anomaly relative to norm, which expresses transport of heat to higher latitude with 60–90-yr periodicity. Again, a relationship between AMO and NAO was found in empirical proxy data (Olsen et al. 2012). (On shorter, decadal time scales, NAO is closely related to the Arctic Oscillation and polar vortex (Hall et al. 2014). The pressure difference is dependent on the temperature difference between the cold Arctic and relatively warm continents during winter. Positive Arctic Oscillation is in turn related to greater sea ice extent, impeding heat transfer from the oceans, and maintaining stable cold air masses over the Arctic (Overland et al. 2011). Negative Arctic Oscillation phase, on the other hand, decelerates polar jet streams, which start meandering and cause more frequent igressions of polar air masses to the mild latitudes (Overland et al. 2011). Explosive volcanism is the last important factor of North Atlantic necessary to mention. The last millennium has seen periods of increased volcanism which together with solar minima may have intensified the LIA severity (Robock et al. 2009). Positive phase of NAO regularly emerges two years after major NH volcanic eruption (Ortega et al. 2015).

NAO is of great importance for mass balance of GrIS, since it influences its surface melt extent and implicitly also albedo and runoff. A lasting negative NAO index and a related high Greenland Blocking index (GBI) initiates three feedback mechanisms through warming and melting of snow (Box et al. 2012): i) advection of warm air masses along the western flank of the GrIS brings more sensible heat; ii) anticyclonic conditions promote clear skies and concomitant increased solar irradiance; iii) ice-sheet surface is darker due to decreased summer snowfall. Furthermore, high GBI together with Arctic Dipole anomaly (Overland et al. 2012). alter summer Arctic atmospheric circulation and cause persistent positive temperature anomalies mainly along the west coast of Greenland (Hanna et al. 2012). Southern advection can thus form ‘heat dome’ over GrIS and adjacent deglaciated areas (Hanna et al., 2014). Such conditions of switching between two NAO phases are recorded *inter alia* in the lacustrine sediments of the southwestern Greenland (Olsen et al. 2012, Roman et al. under review, this thesis).

More recently, Thomas et al. (2009) noticed an extensive simultaneous thinning of distant outlet GrIS glaciers with deep submerged beds and attributed it to warming of deep ocean waters around. Submarine melt rates of west Greenland glaciers display values of two orders greater for than surface melt (Rignot et al. 2010). Relatively warm ocean waters originating in the subtropical North Atlantic (Straneo et al. 2012) are brought to calving fronts by convection driven by subglacial meltwater, discharging from grounding line upwards as an overflow plume (this mechanism apparently initiated the retreat of Jakobshavn Isbræ and other glaciers, Motyka et al. 2011). However, subpolar waters have been warming by increased inflow of subtropical waters, which has been caused by atmospheric and oceanic circulation changes, e.g. NAO or Atlantic multidecadal oscillation

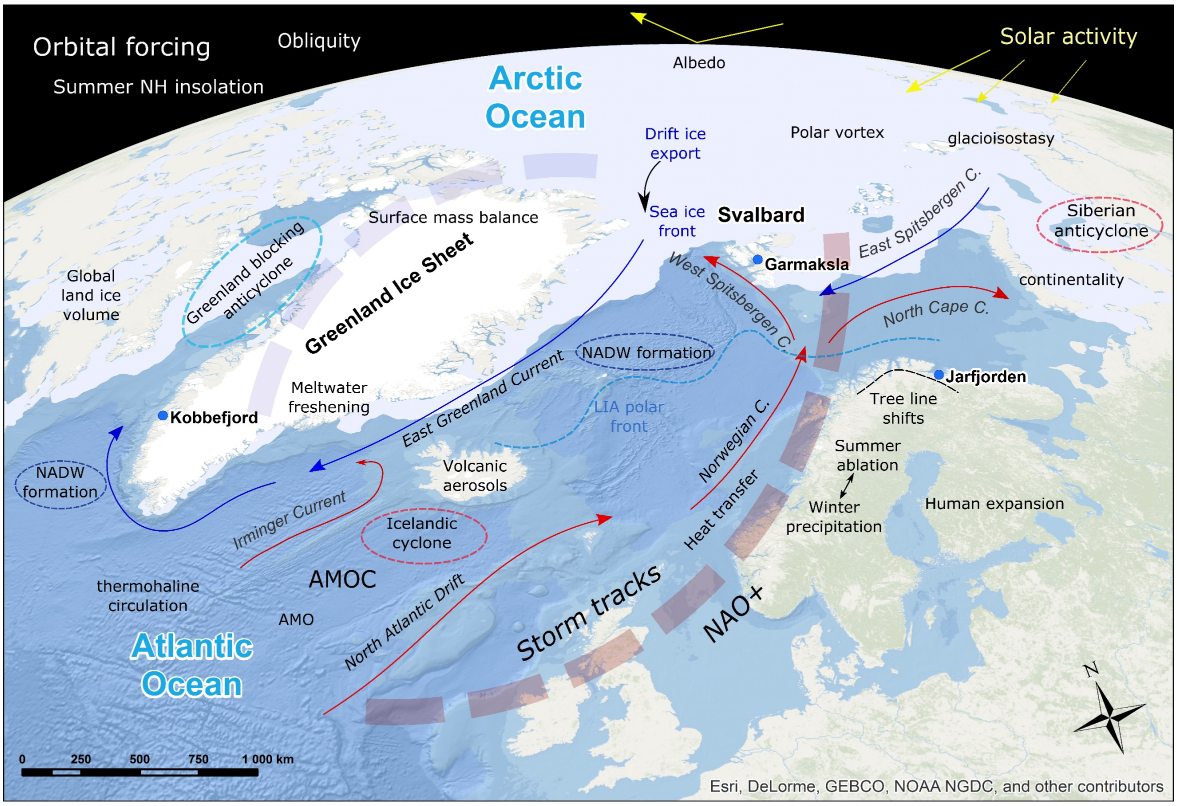

Figure 6.12 Conceptual diagram of various elements of the North Atlantic climate system, that acted upon the environment during the Holocene. Positive phase of NAO is displayed. For details see the main text.

(Straneo and Heimbach 2013). Inversely, GrIS mass loss and ocean freshening in the Labrador Sea can affect the AMOC through suppression of NADW formation in the Labrador Sea (Böning et al. 2016). Unprecedented rates of GrIS mass loss are documented for the 20th century from climatic re-analyses (Box et al. 2013), but also from e.g. cell-wall thickness of Arctic shrubs (Buras et al. 2017). Further extensive melting of the GrIS may thus lead to decreasing or even terminating the heat transport to higher latitudes of the North Atlantic, with all the climatic consequences for the population of Europe (Rahmstorf et al. 2015, Hansen et al. 2016). The only precedence for such situations occurred last time during the disintegration of the Laurentide Ice Sheet and and 8.2 ka event (Sejrup et al. 2016).

VII.Conclusions

This thesis examined how the peri-Atlantic Arctic, one of the most sensitive components of the Earth climate system, experienced pronounced climatic fluctuations during the Holocene. The marked HTM warming gradually descended into the Neoglacial period. Various external forcings and their role in shaping the North Atlantic climate were examined, including solar insolation and orbital forcing, changes in distribution of terrestrial and sea ice masses, volcanic activity, and changes in oceanic and atmospheric circulation.

Three sites located in different parts of the region were selected for palaeoenvironmental reconstructions in order to explore the driving mechanisms of the peri-Atlantic Arctic environmental variability. The main goal was to extract climatic information. With this intention, sedimentary cores from i) Lake Garmaksla, Central Svalbard, ii) Jarfjorden, northeastern Norway, and iii) Kobbefjord area, southwestern Greenland, were obtained and subjected to multi-proxy analyses. The absolute chronostratigraphic framework was secured through comprehensive dating by radiocarbon (^{14}C) and short-lived radioisotopes (^{210}Pb, ^{137}Cs). Next, analyses of magnetic susceptibility, grain size distribution, element composition by means of X-ray fluorescence (XRF), and elements bound to organic matter, i.e. organic carbon, nitrogen, sulphur and biogenic silica, were performed. Stratigraphic sequences were correlated in order to improve accuracy and reliability of the age-depth models. Exploratory statistics and factor analysis (PCA) were applied to extract relevant palaeoenvironmental information. Correlation coefficients and matrices helped in finding the association between the element concentrations and other abiotic proxy data

The presented palaeoenvironmental reconstruction from Garmaksla Lake covers the last 5.5 ka., i.e. the Middle and Late Holocene. Very organic sediment precluded efficient use of several sedimentological proxies (magnetic susceptibility, grain size), although several element ratios were found to mirror ecological shifts of aquatic communities. Moreover, interpretation regarding the formation of laminae was postulated. It was found that Garmaksla Lake sensitively reacted especially sensitively not only to variations sea ice extent but also shifts of oceanity-continentality, which is a response probably unique in hitherto documented natural archives from Svalbard. Several climatic deteriorations, approximately coincident with 4.2 and 2.8 ka events, were expressed in the record. The early onset of Little Ice Age and transition to warm 20th century is recorded in the topmost layers of the sedimentary sequence.

Sedimentary records of Jarfjorden lakes also cover better part of the Holocene and reveal episodes of increased erosion and reduction of vegetation cover, usually during periods of increased environmental instability. The disturbances were induced either by natural or anthropogenic influence, Moreover, evidence of pollution is present in the last 70 years. Infilled lakes from southwestern Greenland document the lake ontogeny and transition to peat bog that was nevertheless modulated by climate, especially the North Atlantic Oscillation over the past ~800 years. The synthesis of palaeoreconstructions from the entire peri-Atlantic Arctic pinpoints the importance of understanding the interconnected factors of climatic variability on the Holocene time scale, since it provides clues on the climate development of the region in the anthropogenically impacted future.

Altogether, this work proves the usefulness of applied methods – they were fast, cheap (except for dating), mostly non-destructive and highly informative. However, I need to accentuate the importance of other simultaneous, mainly biological analyses that were performed on analysed material by colleagues. The limnic ecosystem and sediments, influenced by its catchment and climate, is inherently very complex system and any investigation dealing with the paleolimnological reconstruction should always attempt to use a plethora of methods. In case of Garmaksla and Kobbefjord lakes, the interpretations were greatly enhanced by conclusions of biologists investigating the same cores from the same area. In case of Jarfjorden lakes, the interpretations depended solely on abiotic proxies, which resulted in partially indefinite conclusions. Nevertheless, even if applied methods are used unaccompanied, they should prove a valuable tool in deciphering the past changes.

VIII. References

Aagaard, K., Foldvik, A., Hillman, S.R., 1987. The West Spitsbergen Current: Disposition and water mass transformation. *Journal of Geophysical Research* 92, 3778.

Aarrestad, P.A., Aamlid, D., 1999. Vegetation monitoring in South-Varanger, Norway - Species composition of ground vegetation and its relation to environmental variables and pollution impact. *Environmental Monitoring and Assessment* 58, 1–21.

Abbott, M., Stafford, T.J., 1996. Radiocarbon geochemistry of modern and ancient Arctic lake systems, Baffin Island, Canada. *Quaternary Research* 311, 300–311.

Aebly, F. A., Fritz, S.C., 2009. Palaeohydrology of Kangerlussuaq (Sondre Stromfjord), West Greenland during the last 8000 years. *The Holocene* 19, 91–104.

Allen, J.R.M., Long, A.J., Ottley, C.J., Graham Pearson, D., Huntley, B., 2007. Holocene climate variability in northernmost Europe. *Quaternary Science Reviews* 26, 1432–1453.

Alley, R.B., 1998. Icing the North Atlantic. *Nature* 392, 335–337.

Alley, R.B., Marotzke, J., Nordhaus, W.D., Overpeck, J.T., Peteet, D.M., Pielke, R. a, Pierrehumbert, R.T., Rhines, P.B., Stocker, T.F., Talley, L.D., Wallace, J.M., 2003. Abrupt climate change. *Science* 299, 2005–10.

An, Z., Kukla, G., Porter, S., Xiao, J., 1991. Magnetic susceptibility evidence of monsoon variation on the Loess Plateau of central China during the last 130,000 years. *Quaternary Research* 36, 29–36.

Andersen, K.K., Ditlevsen, P.D., Rasmussen, S.O., Clausen, H.B., Vinther, B.M., Johnsen, S.J., Steffensen, J.P., 2006. Retrieving a common accumulation record from Greenland ice cores for the past 1800 years. *Journal of Geophysical Research Atmospheres* 111, 1–12.

Andersen, O., 2011. Reindeer-herding cultures in northern Nordland, Norway: Methods for documenting traces of reindeer herders in the landscape and for dating reindeer-herding activities. *Quaternary International* 238, 63–75.

Anderson, N.J., Liversidge, A.C., McGowan, S., Jones, M.D., 2012. Lake and catchment response to Holocene environmental change: Spatial variability along a climate gradient in southwest Greenland. *Journal of Paleolimnology* 48, 209–222.

Appleby, P.G., 2008. Three decades of dating recent sediments by fallout radionuclides: a review. *The Holocene* 18, 83–93.

Appleby, P.G., Oldfield, F., 1978. The calculation of 210Pb dates assuming a constant rate of supply of unsuported 210Pb to the sediment. *Catena* 5, 1–8.

Baeten, N.J., Forwick, M., Vogt, C., Vorren, T.O., 2010. Late Weichselian and Holocene sedimentary environments and glacial activity in Billefjorden, Svalbard, in: Fjord Systems and Archives. 207–223.

Bakke, J., Dahl, S.O., Paasche, Ø., Løvlie, R., Nesje, A., 2005. Glacier fluctuations, equilibrium-line altitudes and palaeoclimate in Lyngen, northern Norway, during the Lateglacial and Holocene. *The Holocene* 15, 518–540.

Bakke, J., Dahl, S.O., Paasche, Ø., Riis Simonsen, J., Kvisvik, B., Bakke, K., Nesje, A., 2010. A complete record of Holocene glacier variability at Austre Okstindbreen, northern Norway: an integrated approach. *Quaternary Science Reviews* 29, 1246–1262.

Bakke, J., Lie, Ø., Dahl, S.O., Nesje, A., Bjune, A.E., 2008. Strength and spatial patterns of the Holocene wintertime westerlies in the NE Atlantic region. *Global and Planetary Change* 60, 28–41.

Balascio, N.L., D'Andrea, W.J., Gjerde, M., Bakke, J., 2017. Hydroclimate variability of High Arctic Svalbard during the Holocene inferred from hydrogen isotopes of leaf waxes. *Quaternary Science Reviews* 1–11.

Balascio, N.L., Zhang, Z., Bradley, R.S., Perren, B., Dahl, S.O., Bakke, J., 2011. A multi-proxy approach to assessing isolation basin stratigraphy from the Lofoten Islands, Norway. *Quaternary Research* 75, 288–300.

Ballantyne, C.K., 2002. Paraglacial geomorphology. *Quaternary Science Reviews* 21, 1935–2017.

Barker, P., 2009. Paleolimnology. In: Gornitz, V. (ed.): Encyclopedia of Paleoclimatology and Ancient Environments. Springer, p. 738–743.

Birks, H.H., 1991. Holocene vegetational history and climatic change in west Spitsbergen - plant macrofossils from Skardtjorna, an Arctic lake. *The Holocene* 1, 209–218.

Birks, H.J.B., Seppä, H., 2010. Late-Quaternary palaeoclimatic research in Fennoscandia - A historical review. *Boreas* 39, 655–673.

Blaauw, M., 2010. Methods and code for "classical" age-modelling of radiocarbon sequences. *Quaternary Geochronology* 5, 512–518.

Błaszczyk, M., Jania, J.A., Kolondra, L., 2013. Fluctuations of tidewater glaciers in Hornsund Fjord (Southern Svalbard) since the beginning of the 20th century. *Polish Polar Research* 34, 203–224.

Blott, S.J., Pye, K., 2001. GRADISTAT: a grain size distribution and statistics package for the analysis of unconsolidated sediments. *Earth Surface Processes and Landforms* 26, 1237–1248.

Boehrer, B., Schultze, M., 2008. Stratification of lakes. *Reviews of Geophysics* 46, 1–27.

Bond, G., Broecker, W., Johnsen, S., McManus, J., Labeyrie, L., Jouzel, J., Bonani, G., 1993. Correlations between climate records from North Atlantic sediments and Greenland ice. *Nature* 365, 143–147.

Böning, C.W., Behrens, E., Biastoch, A., Getzlaff, K., Bamber, J.L., 2016. Emerging impact of Greenland meltwater on deepwater formation in the North Atlantic Ocean. *Nature Geoscience* 9, 523–527.

Box, J.E., Cressie, N., Bromwich, D.H., Jung, J.-H., van den Broeke, M., van Angelen, J.H., Forster, R.R., Miège, C., Mosley-Thompson, E., Vinther, B., McConnell, J.R., 2013. Greenland Ice Sheet Mass Balance Reconstruction. Part I: Net Snow Accumulation (1600–2009). *Journal of Climate* 26, 3919–3934.

Box, J.E., Fettweis, X., Stroeve, J.C., Tedesco, M., Hall, D.K., Steffen, K., 2012. Greenland ice sheet albedo feedback: thermodynamics and atmospheric drivers. *The Cryosphere* 6, 821–839.

Boyle, J.F., Chiverrell, R.C., Schillereff, D., 2015. Approaches to Water Content Correction and Calibration for µXRF Core Scanning: Comparing X-ray Scattering with Simple Regression of Elemental Concentrations, in: Micro-XRF Studies of Sediment Cores: Applications of a Non-Destructive Tool for the Environmental Sciences. 373–390.

Bradley, R.S., 2015. Paleoclimatology: Reconstructing Climates of the Quaternary, Academic Press, Amsterdam, 3rd edition, 675 p.

Briner, J.P., McKay, N.P., Axford, Y., Bennike, O., Bradley, R.S., de Vernal, A., Fisher, D., Francus, P., Fréchette, B., Gajewski, K., Jennings, A., Kaufman, D.S., Miller, G., Rouston, C., Wagner, B., 2016. Holocene climate change in Arctic Canada and Greenland. *Quaternary Science Reviews* 147, 340–364.

Broecker, W.S., Denton, G.H., 1990. The role of ocean-atmosphere reorganizations in glacial cycles. *Quaternary Science Reviews* 9, 305–341.

Bronk Ramsey, C., 2009. Bayesian Analysis of Radiocarbon Dates. *Radiocarbon* 51, 337–360.

Brooks, S.J., Birks, H.J.B., 2004. The dynamics of Chironomidae (Insecta: Diptera) assemblages in response to environmental change during the past 700 years on Svalbard. *Journal of Paleolimnology* 31, 483–498.

Buras, A., Lehejček, J., Michalová, Z., Morrissey, R.C., Svoboda, M., Wilmking, M., 2017. Shrubs shed light on 20th century Greenland Ice Sheet melting. *Boreas*.

Carbonara, K., Mezgec, K., Varagona, G., Musco, M.E., Lucchi, R.G., Villa, G., Morigi, C., Melis, R., Caffau, M., 2016. Palaeoclimatic changes in Kveithola, Svalbard, during the Late Pleistocene deglaciation and Holocene: Evidences from microfossil and sedimentary records. *Palaeogeography, Palaeoclimatology, Palaeoecology* 463, 136–149.

Cappelen, J., 2013. Greenland - DMI Historical Climate Data Collection 1873-2012. Danish Meteorological Institute, Copenhagen.

Čepová, D., 2013. Jezerní ekosystémy vybrané oblasti souostroví Špicberky. Bachelor thesis, Depratment of Regional Geography, Faculty of Science, PalackýUniversity, Olomouc, 72 p.

Clark, P.U., Pisias, N.G., Stocker, T.F., Weaver, A.J., 2002. The role of the thermohaline circulation in abrupt climate change. *Nature* 415, 863–869.

Cockburn, J.M.H., Lamoureux, S.F., 2008. Inflow and lake controls on short-term mass accumulation and sedimentary particle size in a High Arctic lake: implications for interpreting varved lacustrine sedimentary records. *Journal of Paleolimnology* 40, 923–942.

Croudace, I.W., Rothwell, R.G., 2015. Micro-XRF Studies of Sediment Cores.

Cohen, A.S., 2003. Paleolimnology: the history and evolution of lake systems. Oxford University Press, Inc., New York. 500 p.

Cuven, S., Francus, P., Lamoureux, S.F., 2011. Mid to Late Holocene hydroclimatic and geochemical records from the varved sediments of East Lake, Cape Bounty, Canadian High Arctic. *Quaternary Science Reviews* 30, 2651–2665.

Cuven, S., Francus, P., Lamoureux, S.F., 2010. Estimation of grain size variability with micro X-ray fluorescence in laminated lacustrine sediments, Cape Bounty, Canadian High Arctic. *Journal of Paleolimnology* 44, 803–817.

D'Andrea, W.J., Huang, Y., Fritz, S.C., Anderson, N.J., 2011. Abrupt Holocene climate change as an important factor for human migration in West Greenland. *Proceedings of the National Academy of Sciences* 108, 9765–9769.

D'Andrea, W.J., Vaillencourt, D.A., Balascio, N.L., Werner, A., Roof, S.R., Retelle, M., Bradley, R.S., 2012. Mild Little Ice Age and unprecedented recent warmth in an 1800 year lake sediment record from Svalbard. *Geology* 40, 1007–1010.

D'Anjou, R.M., Bradley, R.S., Balascio, N.L., Finkelstein, D.B., 2012. Climate impacts on human settlement and agricultural activities in northern Norway revealed through sediment biogeochemistry. *Proceedings of the National Academy of Sciences of the United States of America* 109, 20332–20337.

Dahl-Jensen, D., Mosegaard, K., Gundestrup, N., Clow, G.D., Johnsen, S.J., Hansen, A.W., Balling, N., 1998. Past Temperatures Directly from the Greenland Ice Sheet. *Science* 282, 268–271.

Daley, T.J., Thomas, E.R., Holmes, J. a., Street-Perrott, F.A., Chapman, M.R., Tindall, J.C., Valdes, P.J., Loader, N.J., Marshall, J.D., Wolff, E.W., Hopley, P.J., Atkinson, T., Barber, K.E., Fisher, E.H., Robertson, I., Hughes, P.D.M., Roberts, C.N., 2011. The 8200yr BP cold event in stable isotope records from the North Atlantic region. *Global and Planetary Change* 79, 288–302.

Dallmann, W. K., Piepjohn, K., Blomeier, D. 2004. Geological map of Billegjorden, central Spitsbergen, Svalbard, with geological excursion guide. 1:50,000. Theme map No. 36; Norsk Polarinstittutt.

Davies, S.J., Lamb, H.F., Roberts, S.J., 2015. Micro-XRF Core Scanning in Palaeolimnology: Recent Developments, in: Micro-XRF Studies of Sediment Cores: Applications of a Non-Destructive Tool for the Environmental Sciences. 189–226.

Dearing, J.A., 1999a. Holocene environmental change from magnetic proxies in lake sediments. In: Maher, B.A., Thompson, R. (eds.): Quaternary Climates, Environments and Magnetism. Cambridge University Press, Cambridge, 231–278.

Dearing, J.A., 1999b. Magnetic susceptibility. In: Walden, J., Oldfield, F., Smith, J. (eds.): Environmental magnetism: a practical guide. Technical Guide, No. 6. Quaternary Research Association, London, 35–62.

Dearing, J.A., Dann, R.J.L., Hay, K., Lees, J.A., Loveland, P.J., Maher, B.A., O'Grady, K., 1996. Frequency-dependent susceptibility measurements of environmental materials. *Geophysical Journal International* 124, 228–240.

De Vries, H., 1958. Variations in concentration of radiocarbon with time and location on Earth, Koninkijk Nederlandse Akademie von Wetenschappen, Amsterdam, Proceedings, B61, 94–102.

de Wet, G.A., Balascio, N.L., D'Andrea, W.J., Bakke, J., Bradley, R.S., Perren, B., 2017. Holocene glacier activity reconstructed from proglacial lake Gjøavatnet on Amsterdamøya, NW Svalbard. *Quaternary Science Reviews*, in press.

Escher, J.C., Pulvertaft, T.R.C., 1995. Geological Map of Greenland, 1:2 500 000. Geological Survey of Greenland, Copenhagen.

Esper, J., Düthorn, E., Krusic, P.J., Timonen, M., Büntgen, U., 2014. Northern European summer temperature variations over the Common Era from integrated tree-ring density records. *Journal of Quaternary Science* 29, 487–494.

Evans, M.E., Heller, F., 2003. Environmental magnetism: Principles and Applications of Enviromagnetics. Academic Press, Amsterdam, 299 p.

Farnsworth, W.R., Ingólfsson, Ó., Noormets, R., Allaart, L., Alexanderson, H., Henriksen, M., Schomacker, A., 2017. Dynamic Holocene glacial history of St. Jonsfjorden, Svalbard. *Boreas* 46.

Folk, R.L., Ward, W.C., 1957. Brazos River bar [Texas]; a study in the significance of grain size parameters. *Journal of Sedimentary Research* 27, 3–26.

Førland, E.J., Benestad, R., Hanssen-Bauer, I., Haugen, J.E., Skaugen, T.E., 2011. Temperature and Precipitation Development at Svalbard 1900–2100. *Advances in Meteorology* 2011, 1–14.

Francke, A., Wennrich, V., Sauerbrey, M., Juschus, O., Melles, M., Brigham-Grette, J., 2013. Multivariate statistic and time series analyses of grain-size data in Quaternary sediments of Lake El'gygytgyn, NE Russia. *Climate of the Past* 9, 2459–2470.

Francus, P., von Suchodoletz, H., Dietze, M., Donner, R. V., Bouchard, F., Roy, A.-J., Fagot, M., Verschuren, D., Kröpelin, S., 2013. Varved sediments of Lake Yoa (Ounianga Kebir, Chad) reveal progressive drying of the Sahara during the last 6100 years. *Sedimentology* 60, 911–934.

Funder, S., Kjeldsen, K.K., Kjær, K.H., Ó Cofaigh, C., 2011. The Greenland Ice Sheet during the past 300,000 years: A review. In: Ehlers, J., Gibbard, P.L., Hughes, P.D. (eds.): Quaternary glaciations – extent and chronology. Elsevier, Amsterdam, 699-713.

Gjerde, M., Bakke, J., D'Andrea, W.J., Balascio, N.L., Bradley, R.S., Vasskog, K., Ólafsdóttir, S., Røthe, T.O., Perren, B.B., Hormes, A., 2017. Holocene multi-proxy environmental reconstruction from lake Hakluytvatnet, Amsterdamøya Island, Svalbard (79.5°N). *Quaternary Science Reviews* 1–13.

Glew, J.R., 1989. A new trigger mechanism for sediment samplers. *Journal of Paleolimnology* 2, 241–243.

Guilizzoni, P., Marchetto, A., Lami, A., Brauer, A., Vigliotti, L., Musazzi, S., Langone, L., Manca, M., Lucchini, F., Calanchi, N., Dinelli, E., Mordenti, A., 2006. Records of environmental and climatic changes during the late Holocene from Svalbard: palaeolimnology of Kongressvatnet. *Journal of Paleolimnology* 36, 325–351.

Hagen, J.O., Liestøl, O., Roland, E., Jørgensen, T., 1993. Glacier Atlas of Svalbard. Norsk Polarinstitutt, Oslo, 169 p.

Håkanson, L., Jansson, M., 1983. Principles of Lake Sedimentology. Springer, Berlin, 316 p.

Hald, M., Andersson, C., Ebbesen, H., Jansen, E., Klitgaard-Kristensen, D., Risebrobakken, B., Salomonsen, G.R., Sarnthein, M., Sejrup, H.P., Telford, R.J., 2007. Variations in temperature and extent of Atlantic Water in the northern North Atlantic during the Holocene. *Quaternary Science Reviews* 26, 3423–3440.

Hald, M., Ebbesen, H., Forwick, M., Godtliebsen, F., Khomenko, L., Korsun, S., Ringstad Olsen, L., Vorren, T.O., 2004. Holocene paleoceanography and glacial history of the West Spitsbergen area, Euro-Arctic margin. *Quaternary Science Reviews* 23, 2075–2088.

Hall, C.M., 2009. Dating, radiometric methods. In: Gornitz, V. (ed.): Encyclopedia of Paleoclimatology and Ancient Environments. Springer, 255–260.

Hall, R., Erdélyi, R., Hanna, E., Jones, J.M., Scaife, A. a., 2015. Drivers of North Atlantic Polar Front jet stream variability. *International Journal of Climatology* 35, 1697–1720.

Hammarlund, D., Velle, G., Wolfe, B.B., Edwards, T.W.D., Bergman, J., Holmgren, S., Lamme, S., Snowball, I., Wohlfarth, B., Possnert, G., 2004. Palaeolimnological and sedimentary responses to Holocene forest retreat in the Scandes Mountains, west-central Sweden. *The Holocene* 14, 862–876.

Hanna, E., Fettweis, X., Mernild, S.H., Cappelen, J., Ribergaard, M.H., Shuman, C. a., Steffen, K., Wood, L., Mote, T.L., 2014. Atmospheric and oceanic climate forcing of the exceptional Greenland ice sheet surface melt in summer 2012. *International Journal of Climatology* 34, 1022–1037.

Hanna, E., Mernild, S.H., Cappelen, J., Steffen, K., 2012. Recent warming in Greenland in a long-term instrumental (1881–2012) climatic context: I. Evaluation of surface air temperature records. *Environmental Research Letters* 7, 45404.

Hansen, J., Sato, M., Hearty, P., Ruedy, R., Kelley, M., Masson-Delmotte, V., Russell, G., Tselioudis, G., Cao, J., Rignot, E., Velicogna, I., Tormey, B., Donovan, B., Kandiano, E., Von Schuckmann, K., Kharecha, P., Legrande, A.N., Bauer, M., 2016. Ice melt, sea level rise and superstorms: Evidence from paleoclimate data, climate modeling, and modern observations that 2 °c global warming could be dangerous. *Atmospheric Chemistry and Physics* 16, 3761–3812.

Heinrich, H., 1988. Origin and consequences of cyclic ice rafting in the northeast Atlantic Ocean during the past 130,000 years. *Quaternary research* 152, 142–152.

Helskog, K., 1984. The younger stone age settlements in Varanger, North Norway. *Acta Borealia* 1, 39–70.

Hisdal, V., 1998. Svalbard Nature and History, Norsk Polarinstitutt, Oslo, 127 p.

Hofgaard, A., Tømmervik, H., Rees, G., Hanssen, F., 2013. Latitudinal forest advance in northernmost Norway since the early 20th century. *Journal of Biogeography* 40, 938–949.

Holmgren, S.U., Bigler, C., Ingólfsson, Ó., Wolfe, A.P., 2010. The Holocene–Anthropocene transition in lakes of western Spitsbergen, Svalbard (Norwegian High Arctic): climate change and nitrogen deposition. *Journal of Paleolimnology* 43, 393–412.

Hošek, J., Hambach, U., Lisá, L., Grygar, T.M., Horáček, I., Meszner, S., Knésl, I., 2015. An integrated rock-magnetic and geochemical approach to loess/paleosol sequences from Bohemia and Moravia (Czech Republic): Implications for the Upper Pleistocene paleoenvironment in central Europe. *Palaeogeography, Palaeoclimatology, Palaeoecology* 418, 344–358.

Howat, I.M., A. Negrete, B.E. Smith, 2014. The Greenland Ice Mapping Project (GIMP) land classification and surface elevation datasets, *The Cryosphere*, 8 1509-1518.

Hungr, O., Leroueil, S., Picarelli, L., 2014. The Varnes classification of landslide types, an update. *Landslides* 11, 167–194.

Chawchai, S., Kylander, M.E., Chabangborn, A., Löwemark, L., Wohlfarth, B., 2015. Testing commonly used X-ray fluorescence core scanning-based proxies for organic-rich lake sediments and peat. *Boreas 10.1111/bor.12145*.

Ilyashuk, E.A., Ilyashuk, B.P., Kolka, V. V., Hammarlund, D., 2013. Holocene climate variability on the Kola Peninsula, Russian Subarctic, based on aquatic invertebrate records from lake sediments. *Quaternary Research* 79, 350–361.

Ingólfsson, Ó., Landvik, J.Y., 2013. The Svalbard–Barents Sea ice-sheet – Historical, current and future perspectives. *Quaternary Science Reviews* 64, 33–60.

INTERACT 2012. INTERACT Station Catalogue. In: Elger, K., Opel, T., Topp-Jørgensen, E. and Rasch, M. (eds.). Danish Centre for Environment and Energy, Aarhus University, Denmark. 192 p.

Jansen, H.L., Simonsen, J.R., Dahl, S.O., Bakke, J., Nielsen, P.R., 2016. Holocene glacier and climate fluctuations of the maritime ice cap Hogtuvbreen, northern Norway. *The Holocene*, 1-20.

Jensen, C., Vorren, K.-D., 2008. Holocene vegetation and climate dynamics of the boreal alpine ecotone of northwestern Fennoscandia. *Journal of Quaternary Science* 23, 719–743.

Jiang, S., Liu, X., Sun, J., Yuan, L., Sun, L., Wang, Y., 2011. A multi-proxy sediment record of late Holocene and recent climate change from a lake near Ny-Ålesund, Svalbard. *Boreas* 40, 468–480.

Jones, B.F., Bowser, C.J., 1978. The Mineralogy and Related Chemistry of Lake Sediments, in: Lerman, A. (Ed.), Lakes: Chamistry, Geology and Physics. Springer New York, New York, NY, 179–235.

Jones, V.J., Birks, H.J.B., 2004. Lake-sediment records of recent environmental change on Svalbard: Results of diatom analysis. *Journal of Paleolimnology* 31, 445–466.

Jouve, G., Francus, P., Lamoureux, S., Provencher-Nolet, L., Hahn, A., Haberzettl, T., Fortin, D., Nuttin, L., 2013. Microsedimentological characterization using image analysis and μ-XRF as indicators of sedimentary processes and climate changes during Lateglacial at Laguna Potrok Aike, Santa Cruz, Argentina. *Quaternary Science Reviews* 71, 191–204.

Kalugin, I., Daryin, A., Smolyaninova, L., Andreev, A., Diekmann, B., Khlystov, O., 2007. 800-yr-long records of annual air temperature and precipitation over southern Siberia inferred from Teletskoye Lake sediments. *Quaternary Research* 67, 400–410.

Kaplan, M.R., Wolfe, A.P., Miller, G.H., 2002. Holocene Environmental Variability in Southern Greenland Inferred from Lake Sediments. *Quaternary Research* 58, 149–159.

Karlsson, H., Hornberg, G., Hannon, G., Nordstrom, E.-M., 2007. Long-term vegetation changes in the northern Scandinavian forest limit: a human impact-climate synergy? *The Holocene* 17, 37–49.

Kaufman, D.S., Schneider, D.P., McKay, N.P., Ammann, C.M., Bradley, R.S., Briffa, K.R., Miller, G.H., Otto-Bliesner, B.L., Overpeck, J.T., Vinther, B.M., Arctic Lakes 2k Project Members, 2009. Recent Warming Reverses Long-Term Arctic Cooling. *Science* 325, 1236–1239.

Kempf, P., Forwick, M., Laberg, J.S., Vorren, T.O., 2013. Late Weichselian and Holocene sedimentary palaeoenvironment and glacial activity in the high-arctic van Keulenfjorden, Spitsbergen. *The Holocene* 23, 1607–1618.

Kjeldsen, K.K., Korsgaard, N.J., Bjørk, A.A., Khan, S.A., Box, J.E., Funder, S., Larsen, N.K., Bamber, J.L., Colgan, W., van den Broeke, M., Siggaard-Andersen, M.-L., Nuth, C., Schomacker, A., Andresen, C.S., Willerslev, E., Kjær, K.H., 2015. Spatial and temporal distribution of mass loss from the Greenland Ice Sheet since AD 1900. *Nature* 528, 396–400.

Kletetschka, G., Hrubá, J., Nábělek, L., 2015. Magnetic susceptibility of wet vs. dry sediment and mass normalized vs. volume normalized magnetic susceptibility. AGU Fall Meeting Abstracts, 2015.

Korhola, A., Tikkanen, M., Weckström, J., 2005. Quantification of Holocene lake-level changes in Finnish Lapland using a cladocera - Lake depth transfer model. *Journal of Paleolimnology* 34, 175–190.

Korhola, A., Vasko, K., Toivonen, H.T.T., Olander, H., 2002. Holocene temperature changes in northern Fennoscandia reconstructed from chironomids using Bayesian modelling. *Quaternary Science Reviews* 21, 1841–1860.

Kottek, M., Grieser, J., Beck, C., Rudolf, B., Rubel, F., 2006. World map of the Köppen-Geiger climate classification updated. *Meteorologische Zeitschrift* 15, 259–263.

Kylander, M.E., Ampel, L., Wohlfarth, B., Veres, D., 2011. High-resolution X-ray fluorescence core scanning analysis of Les Echets (France) sedimentary sequence: new insights from chemical proxies. *Journal of Quaternary Science* 26, 109–117.

Lamoureux, S.F., Gilbert, R., 2004. A 750-yr record of autumn snowfall and temperature variability and winter storminess recorded in the varved sediments of Bear Lake, Devon Island, Arctic Canada. *Quaternary Research* 61, 134–147.

Lanza, R., Meloni, A., 2006. The Earth's Magnetism: An Introduction for Geologists. Springer, Berlin, Heidelberg, New York, .

Lapointe, F., Francus, P., Lamoureux, S.F., Saïd, M., Cuven, S., 2012. 1750 years of large rainfall events inferred from particle size at East Lake, Cape Bounty, Melville Island, Canada. *Journal of Paleolimnology* 48, 159–173.

Larsen, C.P.S., MacDonald, G.M., 1993. Lake morphometry, sediment mixing and the selection of sites for fine resolution palaeoecological studies. *Quaternary Science Reviews* 12, 781–792.

Larsen, N.K., Kjær, K.H., Lecavalier, B., Bjørk, A.A., Colding, S., Huybrechts, P., Jakobsen, K.E., Kjeldsen, K.K., Knudsen, K.L., Odgaard, B. V., Olsen, J., 2015. The response of the southern Greenland ice sheet to the Holocene thermal maximum. *Geology* 43, 291–294.

Larsen, N.K., Strunk, A., Levy, L.B., Olsen, J., Bjørk, A., Lauridsen, T.L., Jeppesen, E., Davidson, T.A., 2017. Strong altitudinal control on the response of local glaciers to Holocene climate change in southwest Greenland. *Quaternary Science Reviews* 168, 69–78.

Láska, K., Witoszová, D., Prošek, P., 2012. Weather patterns of the coastal zone of Petuniabukta, central Spitsbergen in the period 2008–2010. *Polish Polar Research* 33, 309–326.

Laskar, J., Robutel, P., Joutel, F., Gastineau, M., Correia, A. C.M., Levrard, B., 2004. A long-term numerical solution for the insolation quantities of the Earth. *Astronomy and Astrophysics* 428, 261–285.

Last, W.M., 2001. Mineralogical analysis of lake sediments. In: Last. W.M., Smol, J.P. (eds.): Tracking Environmental Change Using Lake Sediments, Volume 2: Physical and Geochemical Methods. Kluwer Academic Publisher, Dordrecht, 143–188.

Leppäranta, M., Lindgren, E., Shirasawa, K., 2017. The heat budget of Lake Kilpisjärvi in the Arctic tundra. *Hydrology Research* 48, 969–980.

Levy, L.B., Larsen, N.K., Davidson, T.A., Strunk, A., Olsen, J., Jeppesen, E., 2017. Contrasting evidence of Holocene ice margin retreat, south-western Greenland. *Journal of Quaternary Science* 9999, 1–13.

Lexa, M., 2015. Dendroclimatology of Arctic shrubs. Master thesis, Department of Physical Geography and Geoecology, Faculty of Science, Charles University, Praha, 80 p.

Libby, W.F., Anderson, E.C., Arnold, J.R., 1949. Age Determination by Radiocarbon Content: World-Wide Assay of Natural Radiocarbon. *Science* 109, 227–228.

Lien, L., Henriksen, A., Traaen, T.S., 1995. Critical loads of acidity to surface waters: Svalbard. *Science of The Total Environment* 160–161, 703–713.

Lohne, Ø.S., Mangerud, J., Birks, H.H., 2013. Precise ^{14}C ages of the Vedde and Saksunarvatn ashes and the Younger Dryas boundaries from western Norway and their comparison with the Greenland Ice Core (GICC05) chronology. *Journal of Quaternary Science* 28, 490–500.

Lowe, J., Walker, M., 2014. Reconstructing Quaternary Environments. 3rd edition, Routledge, London, 538 p.

Luláк, M., Hanáček, M., Nývlt, D., Ditrich, O., 2017. Sea Ice-Free Conditions in Inner Fjord on Spitsbergen (Mimerbukta, Billefjorden) in Early Holocene. Poster at Arctic Science Summit Week 2017 Conference, 1st-5th April 2017, Praha, Czech Republic.

Luoto, T.P., Brooks, S.J., Salonen, V.P., 2014a. Ecological responses to climate change in a bird-impacted High Arctic pond (Nordaustlandet, Svalbard). *Journal of Paleolimnology* 51, 87–97.

Luoto, T.P., Kaukolehto, M., Weckström, J., Korhola, A., Väliranta, M., 2014b. New evidence of warm early-Holocene summers in subarctic Finland based on an enhanced regional chironomid-based temperature calibration model. *Quaternary Research* 81, 50–62.

Luoto, T.P., Sarmaja-Korjonen, K., 2011. Midge-inferred Holocene effective moisture fluctuations in a subarctic lake, northern Lapland. *Boreas* 40, 650–659.

Mackie, E.A. V., Lloyd, J.M., Leng, M.J., Bentley, M.J., Arrowsmith, C., 2007. Assessment of δ13C and C/N ratios in bulk organic matter as palaeosalinity indicators in Holocene and Lateglacial isolation basin sediments, northwest Scotland. *Journal of Quaternary Science* 22, 579–591.

Mangerud, J., Svendsen, J.I., 2017. The Holocene Thermal Maximum around Svalbard, Arctic North Atlantic; molluscs show early and exceptional warmth. *The Holocene* 95968361771570.

Marshall, M.H., Lamb, H.F., Huws, D., Davies, S.J., Bates, R., Bloemendal, J., Boyle, J., Leng, M.J., Umer, M., Bryant, C., 2011. Late Pleistocene and Holocene drought events at Lake Tana, the source of the Blue Nile. *Global and Planetary Change* 78, 147–161.

Massa, C., Bichet, V., Gauthier, E., Perren, B.B., Mathieu, O., Petit, C., Monna, F., Giraudeau, J., Losno, R., Richard, H., 2012. A 2500 year record of natural and anthropogenic soil erosion in South Greenland. *Quaternary Science Reviews* 32, 119–130.

Mather, A., 2011. Interpreting Quaternary environments. In: Gregory, K.J., Goudie, A.S. (eds.): The SAGE Handbook of Geomorphology. SAGE Publications, London, 513–534.

McConnaughey, T.A., Whelan, J.F., 1997. Calcification generates protons for nutrient and bicarbonate uptake. *Earth-Science Reviews* 42, 95–117.

McGowan, S., Juhler, R.K., Anderson, N.J., 2008. Autotrophic response to lake age, conductivity and temperature in two West Greenland lakes. *Journal of Paleolimnology* 39, 301–317.

Melles, M., Brigham-Grette, J., Minyuk, P.S., Nowaczyk, N.R., Wennrich, V., DeConto, R.M., Anderson, P.M., Andreev, A.A., Coletti, A., Cook, T.L., Haltia-Hovi, E., Kukkonen, M., Lozhkin, A. V, Rosen, P., Tarasov, P., Vogel, H., Wagner, B., 2012. 2.8 Million Years of Arctic Climate Change from Lake El'gygytgyn, NE Russia. *Science* 337, 315–320.

Meyers, P.A., Lallier-Vergès, E., 1999. Lacustrine sedimentary organic matter of Late Quaternary paleoclimates. *Journal of Paleolimnology* 21, 345–372.

Miller, G.H., Alley, R.B., Brigham-grette, J., Fitzpatrick, J.J., Polyak, L., Serreze, M.C., White, J.W.C.C., 2010. Arctic amplification: can the past constrain the future? *Quaternary Science Reviews* 29, 1779–1790.

Miller, G.H., Brigham-Grette, J., Alley, R.B., Anderson, L., Bauch, H.A., Douglas, M.S. V, Edwards, M.E., Elias, S.A., Finney, B.P., Fitzpatrick, J.J., Funder, S. V, Herbert, T.D., Hinzman, L.D., Kaufman, D.S., Macdonald, G.M., Polyak, L., Robock, A., Serreze, M.C., Smol, J.P., Spielhagen, R., White, J.W.C., Wolfe, A.P., Wolff, E.W., 2010. Temperature and precipitation history of the Arctic. *Quaternary Science*

Reviews 29, 1679–1715.

Miller, G.H., Landvik, J.Y., Lehman, S.J., Southon, J.R., 2017. Episodic Neoglacial snowline descent and glacier expansion on Svalbard reconstructed from the 14C ages of ice-entombed plants. *Quaternary Science Reviews* 155, 67–78.

Millet, L., Massa, C., Bichet, V., Frossard, V., Belle, S., Gauthier, E., 2014. Anthropogenic versus climatic control in a high-resolution 1500-year chironomid stratigraphy from a southwestern Greenland lake. *Quaternary Research* 81, 193–202.

Møller, H.S., Jensen, K.G., Kuijpers, A., Aagaard-Sørensen, S., Seidenkrantz, M.-S., Prins, M., Endler, R., Mikkelsen, N., 2006. Late-Holocene environment and climatic changes in Ameralik Fjord, southwest Greenland: evidence from the sedimentary record. *The Holocene* 16, 685–695.

Motyka, R.J., Truffer, M., Fahnestock, M., Mortensen, J., Rysgaard, S., Howat, I., 2011. Submarine melting of the 1985 Jakobshavn Isbrae floating tongue and the triggering of the current retreat. *Journal of Geophysical Research: Earth Surface* 116, F01007.

Müller, J., Werner, K., Stein, R., Fahl, K., Moros, M., Jansen, E., 2012. Holocene cooling culminates in sea ice oscillations in Fram Strait. *Quaternary Science Reviews* 47, 1–14.

Myking, T., Aarrestad, P.A., Derome, J., Bakkestuen, V., Bjerke, J.W., Gytarsky, M., Isaeva, L., Karaban, R., Korotkov, V., Lindgren, M., Lindroos, A.J., Røsberg, I., Salemaa, M., Tømmervik, H., Vassilieva, N., 2009. Effects of air pollution from a nickel-copper industrial complex on boreal forest vegetation in the joint Russian-Norwegian-Finnish border area. *Boreal Environment Research* 14, 279–296.

Nehyba, S., Nývlt, D., Schkade, U., Kirchner, G., Franců, E., 2011. Depositional rates and dating techniques of modern deposits in the Brno reservoir (Czech Republic) during the last 70 years. *Journal of Paleolimnology* 45, 41–55.

Nesje, A., Jansen, E., Birks, H.J.B., Bjune, A.E., Bakke, J., Andersson, C., Dahl, S.O., Kristensen, D.K., Lauritzen, S.-E., Lie, Ø., Risebrobakken, B., Svendsen, J.-I., 2005. Holocene climate variability in the northern North Atlantic region: A review of terrestrial and marine evidence. In: Drange, H., Dokken, T., Furevik, T., Gredes, R., Berger, W. (eds.): The Nordic Seas: An Integrated Perspective. AGU Geophysical Monograph, 289–322.

Oldfield, F., Wake, R., Boyle, J., Jones, R., Nolan, S., Gibbs, Z., Appleby, P., Fisher, E., Wolff, G., 2003. The late-Holocene history of Gormire Lake (NE England) and its catchment: a multiproxy reconstruction of past human impact. *The Holocene* 13, 677–690.

Olsen, J., Anderson, N.J., Knudsen, M.F., 2012. Variability of the North Atlantic Oscillation over the past 5,200 years. *Nature Geoscience* 5, 808–812.

Olsen, J., Anderson, N.J., Leng, M.J., 2013. Limnological controls on stable isotope records of late-Holocene palaeoenvironment change in SW Greenland: a paired lake study. *Quaternary Science Reviews* 66, 85–95.

Opitz, S., Wünnemann, B., Aichner, B., Dietze, E., Hartmann, K., Herzschuh, U., IJmker, J., Lehmkuhl, F., Li, S., Mischke, S., Plotzki, A., Stauch, G., Diekmann, B., 2012. Late Glacial and Holocene development of Lake Donggi Cona, north-eastern Tibetan Plateau, inferred from sedimentological analysis. *Palaeogeography, Palaeoclimatology, Palaeoecology* 337–338, 159–176.

Ortega, P., Lehner, F., Swingedouw, D., Masson-Delmotte, V., Raible, C.C., Casado, M., Yiou, P., 2015. A model-tested North Atlantic Oscillation reconstruction for the past millennium. *Nature* 523, 71–74.

Overland, J.E., Francis, J. a., Hanna, E., Wang, M., 2012. The recent shift in early summer Arctic atmospheric circulation. *Geophysical Research Letters* 39, L19804.

Overland, J.E., Wood, K.R., Wang, M., 2011. Warm Arctic—cold continents: climate impacts of the newly open Arctic Sea. *Polar Research* 30, 1–14.

Paasche, Ø., Løvlie, R., Dahl, S.O., Bakke, J., Nesje, A., 2004. Bacterial magnetite in lake sediments: Late glacial to Holocene climate and sedimentary changes in northern Norway. *Earth and Planetary Science Letters* 223, 319–333.

Pearce, D., Mair, D., Rea, B., Schofield, E., Lea, J., Barr, I., Kamenos, N., Schoenrock, K., 2017.: A millennial-scale record of tidewater glacier advance and retreat, SW Greenland. *Geophysical Research Abstracts* Vol. 19, EGU2017-1403.

Petrovský, E., Ellwood, B.B., 1999. Magnetic monitoring of air-, land- and water-pollution. In: Maher, B.A., Thompson, R. (eds.): Quaternary Climates, Environments and Magnetism. Cambridge University Press, Cambridge, 279–322.

Pinseel, E., 2014. Environmental Changes in a High Arctic Ecosystem. Master thesis. Department of Biology, Faculty of Science, University of Antwerpen, 160 s.

Plikk, A., Helmens, K.F., Fernández-Fernández, M., Kylander, M., Löwemark, L., Risberg, J., Salonen, J.S., Väliranta, M., Weckström, J., 2016. Development of an Eemian (MIS 5e) Interglacial palaeolake at Sokli (N Finland) inferred using multiple proxies. *Palaeogeography, Palaeoclimatology, Palaeoecology* 463, 11–26.

Polická, P., 2014. Soil properties in the Kobbefjord (Greenland) in relation to vegetation cover and exposition. Master thesis, Czech University of Life Sciences, Prague, 64 p.

Rahmstorf, S., Box, J.E., Feulner, G., Mann, M.E., Robinson, A., Rutherford, S., Schaffernicht, E.J., 2015. Exceptional twentieth-century slowdown in Atlantic Ocean overturning circulation. *Nature Climate Change* 5, 475–480.

Rachlewicz, G., Szczucínski, W., Ewertowski, M., 2007. Post-"Little Ice Age" retreat rates of glaciers around Billefjorden in central Spitsbergen, Svalbard. *Polish Polar Research* 28, 159–186.

Rantala, M. V., Luoto, T.P., Weckström, J., Perga, M.E., Rautio, M., Nevalainen, L., 2015. Climate controls on the Holocene development of a subarctic lake in northern Fennoscandia. *Quaternary Science Reviews* 126, 175–185.

Rasmussen, T.L., Forwick, M., Mackensen, A., 2013. Reconstruction of inflow of Atlantic Water to Isfjorden, Svalbard during the Holocene: Correlation to climate and seasonality. *Marine Micropaleontology* 99, 18–28.

Rasmussen, T.L., Thomsen, E., Skirbekk, K., Ślubowska-Woldengen, M., Klitgaard Kristensen, D., Koç, N., 2014. Spatial and temporal distribution of Holocene temperature maxima in the northern Nordic seas: interplay of Atlantic-, Arctic- and polar water masses. *Quaternary Science Reviews* 92, 280–291.

Reimer, P.J., Bard, E., Bayliss, A., Beck, J.W., Blackwell, P.G., Bronk, M., Grootes, P.M., Guilderson, T.P., Haflidason, H., Hajdas, Hatte, C., Heaton, T.J., Hoffman, D.L., Hogg, A.G., Hughhen, K.A., Kaiser, J.F., Kromer, B., Manning, S.W., Niu, M., Reimer, R.W., Richards, D.A., Scott, E.M., Southon, J.R., Staff, R.A., Turney, C.S.M., van der Plicht, J., 2013. IntCal 13 and Marine 13 radiocarbon age calibration curves 0–50,000 years cal BP. *Radiocarbon* 55, 1869–1887.

Reusche, M., Winsor, K., Carlson, A.E., Marcott, S.A., Rood, D.H., Novak, A., Roof, S., Retelle, M., Werner, A., Caffee, M., Clark, P.U., 2014. 10Be surface exposure ages on the late-Pleistocene and Holocene history of Linnébreen on Svalbard. *Quaternary Science Reviews* 89, 5–12.

Reuss, N.S., Hammarlund, D., Rundgren, M., Segerström, U., Eriksson, L., Rosén, P., 2010. Lake ecosystem responses to Holocene climate change at the subarctic tree-line in Northern Sweden. *Ecosystems* 13, 393–409.

Ribeiro, S., Moros, M., Ellegaard, M., Kuijpers, A., 2012. Climate variability in West Greenland during the past 1500 years: Evidence from a high-resolution marine palynological record from Disko Bay. *Boreas* 41, 68–83.

Rignot, E., Koppes, M., Velicogna, I., 2010. Rapid submarine melting of the calving faces of West Greenland glaciers. *Nature Geoscience* 3, 187–191.

Robock, A., 2000. Volcanic eruptions and climate. *Reviews of Geophysics* 38, 191–219.

Rognerud, S., Dauvalter, V.A., Fjeld, E., Skjelkvåle, B.L., Christensen, G., Kashulin, N., 2013. Spatial trends of trace-element contamination in recently deposited lake sediment around the Ni-Cu Smelter at Nikel, Kola Peninsula, Russian Arctic. *Ambio* 42, 724–736.

Røthe, T.O., Bakke, J., Vasskog, K., Gjerde, M., D'Andrea, W.J., Bradley, R.S., 2015. Arctic Holocene glacier fluctuations reconstructed from lake sediments at Mitrahalvøya, Spitsbergen. *Quaternary Science Reviews* 109, 111–125.

Ruddiman, W.F., McIntyre, A., 1981. The North Atlantic Ocean during the last deglaciation. *Palaeogeography, Palaeoclimatology, Palaeoceanography* 35, 145–214.

Rydberg, J., Lindborg, T., Sohlenius, G., Reuss, N., Olsen, J., 2016. The importance of eolian input on lake-sediment geochemical composition in the dry proglacial landscape of western Greenland. *Arctic, Antarctic, and Alpine* Research 48, 93–109.

Sandgren, P., Snowball, I., 2001. Application of mineral magnetic techniques to paleolimnology. In: Last. W.M., Smol, J.P. (eds.): Tracking Environmental Change Using Lake Sediments, Volume 2: Physical and Geochemical Methods. Kluwer Academic Publisher, Dordrecht, 217–238.

Sarmaja-Korjonen, K., Nyman, M., Kultti, S., Väliranta, M., 2006. Palaeolimnological development of Lake Njargajavri, northern Finnish Lapland, in a changing Holocene climate and environment. *Journal of Paleolimnology* 35, 65–81.

Seidenkrantz, M.-S., Aagaard-Sorensen, S., Sulsbruck, H., Kuijpers, A., Jensen, K.G., Kunzendorf, H., 2007. Hydrography and climate of the last 4400 years in a SW Greenland fjord: implications for Labrador Sea palaeoceanography. *The Holocene* 17, 387–401.

Sejrup, H.P., Seppä, H., McKay, N.P., Kaufman, D.S., Geirsdóttir, Á., de Vernal, A., Renssen, H., Husum, K., Jennings, A., Andrews, J.T., 2016. North Atlantic-Fennoscandian Holocene climate trends and mechanisms. *Quaternary Science Reviews* 147, 365–378.

Sha, L., Jiang, H., Knudsen, K.L., 2011. Diatom evidence of climatic change in Holsteinsborg Dyb, west of Greenland, during the last 1200 years. *The Holocene* 22, 347–358.

Shala, S., Helmens, K.F., Luoto, T.P., Salonen, J.S., Väliranta, M., Weckström, J., 2017. Comparison of quantitative Holocene temperature reconstructions using multiple proxies from a northern boreal lake. *The Holocene* 95968361770844.

Skandfer, M., Høeg, H.I., 2012. Bacheveaj/Pasvikdalens eldre historie belyst ved pollenanalyser og arkeologisk materiale. *Viking* LXXV, 27–52.

Smol, J.P., 1985. The ratio of diatom frustules to chrysophycean statospores: A useful paleolimnological index. *Hydrobiologia* 123:199–208.

Snowball, I.F., Sandgren, P., Petterson, G., 1999. The mineral magnetic properties of an annually laminated Holocene lake-sediment sequence in northern Sweden. *The Holocene* 9, 353–362.

Snowball, I.F.., Thompson, R., 1990. A mineral magnetic study of Holocene sedimentation in Lough Catherine, Northern Ireland. *Boreas* 19, 127–146.

Snowball, I.F., 1993. Geochemical control of magnetite dissolution in subarctic lake sediments and the implications for environmental magnetism. *Journal of Quaternary Science* 8, 339–346.

Solomina, O.N., Bradley, R.S., Hodgson, D.A., Ivy-Ochs, S., Jomelli, V., Mackintosh, A.N., Nesje, A., Owen, L.A., Wanner, H., Wiles, G.C., Young, N.E., 2015. Holocene glacier fluctuations. *Quaternary Science Reviews* 111, 9–34.

Solomina, O.N., Bradley, R.S., Jomelli, V., Geirsdottir, A., Kaufman, D.S., Koch, J., Mckay, N.P., Masiokas, M., Miller, G., Nesje, A., Nicolussi, K., Owen, L.A., Putnam, A.E., Wanner, H., Wiles, G., Yang, B., 2016. Glacier fluctuations during the past 2000 years. *Quaternary Science Reviews* 149, 61–90.

Solovieva, N., Tarasov, P.E., MacDonald, G., 2005. Quantitative reconstruction of Holocene climate from the Chuna Lake pollen record, Kola Peninsula, northwest Russia. *Holocene* 15, 141–148.

Sørensen, L., 2014. From Hunter To Farmer in Northern Europe: Migration and adaptation during the Neoltihic and Bronze Age. PhD Dissertation, University of Copenhage. *Acta Archaeologica* II.

Stober, J.C., Thompson, R., 1979. An investigation into the source of magnetic minerals in some Finnish lake sediments. *Earth and Planetary Science Letters* 45, 464–474.

Straneo, F., Heimbach, P., 2013. North Atlantic warming and the retreat of Greenland's outlet glaciers. *Nature* 504, 36–43.

Straneo, F., Sutherland, D. a., Holland, D., Gladish, C., Hamilton, G.S., Johnson, H.L., Rignot, E., Xu, Y., Koppes, M., 2012. Characteristics of ocean waters reaching Greenland's glaciers. *Annals of Glaciology* 53, 202–210.

Svendsen, J.I., Mangerud, J., 1997. Holocene glacial and climatic variations on Spitsbergen, Svalbard. *The Holocene* 7, 45–57.

Swarzenski, P.W., 2015. ^{210}Pb dating. In: Rink, W.S., Thompson, J.W. (eds.): Encyclopedia of Scientific Dating Methods. Springer, Dordrecht, 626–632.

Tejnecký, V., Šamonil, P., Grygar, T.M., Vašát, R., Ash, C., Drahota, P., Šebek, O., Němeček, K., Drábek O., 2015. Transformation of iron forms during pedogenesis after tree uprooting in a natural beech-dominated forest. *CATENA* 132:12–20.

Teller, J., Leverington, D., Mann, J., 2002. Freshwater outbursts to the oceans from glacial Lake Agassiz and their role in climate change during the last deglaciation. *Quaternary Science Reviews* 21, 879–887.

Thomas, R., Frederick, E., Krabill, W., Manizade, S., Martin, C., 2009. Recent changes on Greenland outlet glaciers. *Journal of Glaciology* 55, 147–162.

Thompson, R., Battarbee, R. W., O'Sullivan, P. E. & Oldfield, F., 1975. Magnetic susceptibility of lake sediments. Limnology and Oceanography, 20, 687–98.

Thompson, R., Clark, R.M., Boulton, G.S., 2012. Core Correlation. In: Birks, H.J.B. et al. (eds.): Tracking Environmental Change Using Lake Sediments. Vol 5: Data Handling and Numerical Techniques. Springer, Dordrecht. 415–430.

Thompson, R., Morton, D.J., 1979. Magnetic susceptibility and particle size distribution in recent sediments of the Loch Lomond drainage basin. *Sedimentary petrology* 49, 801–812.

Thompson, R., Oldfield, F., 1986. Environmental Magnetism. Springer Netherlands, Dordrecht, 227 p.

Uxa, T., Mida, P., Křížek, M., 2017. Effect of Climate on Morphology and Development of Sorted Circles and Polygons. *Permafrost and Periglacial Processes*,10.1002/ppp.1949.

Väliranta, M., Salonen, J.S., Heikkilä, M., Amon, L., Helmens, K., Klimaschewski, A., Kuhry, P., Kultti, S., Poska, A., Shala, S., Veski, S., Birks, H.H., 2015. Plant macrofossil evidence for an early onset of the Holocene summer thermal maximum in northernmost Europe. *Nature Communications* 6, 6809.

Van Daele, M., Moernaut, J., Silversmit, G., Schmidt, S., Fontijn, K., Heirman, K., Vandoorne, W., De Clercq, M., Van Acker, J., Wolff, C., Pino, M., Urrutia, R., Roberts, S.J., Vincze, L., De Batist, M., 2014. The 600 yr eruptive history of Villarrica Volcano (Chile) revealed by annually laminated lake sediments. *Bulletin of the Geological Society of America* 126, 481–498.

Van de Vijver, B., Beyens, L., Vincke, S., Gremmen. N.J.M., 2004. Moss-inhabiting diatom communities from Heard Island, sub-Antarctic. *Polar Biology* 27:532–543.

van der Bilt, W.G.M., Bakke, J., Vasskog, K., D'Andrea, W.J., Bradley, R.S., Ólafsdóttir, S., 2015. Reconstruction of glacier variability from lake sediments reveals dynamic Holocene climate in Svalbard. *Quaternary Science Reviews* 126, 201–218.

van der Bilt, W.G.M., D'Andrea, W.J., Bakke, J., Balascio, N.L., Werner, J.P., Gjerde, M., Bradley, R.S., 2016. Alkenone-based reconstructions reveal four-phase Holocene temperature evolution for High Arctic Svalbard. *Quaternary Science Reviews*, in press.

Van Hove, P., Belzile, C., Gibson, J.A., Vincent, W.F., 2006. Coupled landscape-lake evolution in High Arctic Canada. *Canadian Journal of Earth Sciences* 43, 533–546.

Vinther, B.M., Clausen, H.B., Johnsen, S.J., Rasmussen, S.O., Andersen, K.K., Buchardt, S.L., Seierstad, I.K., Steffensen, J.P., Svensson, A., Olsen, J., Heinemeier, J., 2006. A synchronized dating of three Greenland ice cores throughout the Holocene. *Journal of Geophysical Research* 111, 1–11.

Vinther, B.M., Johnsen, S.J., Andersen, K.K., Clausen, H.B., Hansen, A.W., 2003. NAO signal recorded in the stable isotopes of Greenland ice cores. *Geophysical Research Letters* 30, 1387.

Virkanen, J., 2000. The effects of natural environmental changes on sedimentation in Lake Kuttanen, a small closed lake in Finnish Lapland. *The Holocene* 10, 377–386.

Walker, M., 2005. Quaternary Dating Methods. John Wiley & Sons Ltd., Chichester, 286 p.

Walker, M.J.C., Berkelhammer, M., Björck, S., Cwynar, L.C., Fisher, D.A., Long, A.J., Lowe, J.J., Newnham, R.M., Rasmussen, S.O., Weiss, H., 2012. Formal subdivision of the Holocene Series/Epoch: a Discussion Paper by a Working Group of INTIMATE (Integration of ice-core, marine and terrestrial records) and the Subcommission on Quaternary Stratigraphy (International Commission on Stratigraphy). *Journal of Quaternary Science* 27, 649–659.

Weidick, A., Bennike, O., Citterio, M., Nørgaard-Pedersen, N., 2012. Neoglacial and historical glacier changes around Kangersuneq fjord in southern West Greenland, Geological Survey of Denmark and Greenland Bulletin.

Werner, K., Müller, J., Husum, K., Spielhagen, R.F., Kandiano, E.S., Polyak, L., 2016. Holocene sea subsurface and surface water masses in the Fram Strait – Comparisons of temperature and sea-ice reconstructions. *Quaternary Science Reviews* 147, 194–209.

Werner, K., Spielhagen, R.F., Bauch, D., Hass, H.C., Kandiano, E., 2013. Atlantic Water advection versus sea-ice advances in the eastern Fram Strait during the last 9 ka: Multiproxy evidence for a two-phase Holocene. *Paleoceanography* 28, 283–295.

Wetzel, R.G., 2001. Limnology - Lake and River Ecosystems. Academic Press, 3rd edition, 1006 p.

White, J.W.C., Alley, R.B., Brigham-grette, J., Fitzpatrick, J.J., Jennings, A.E., Johnsen, S.J., Miller, G.H., Nerem, R.S., Polyak, L., 2010. Past rates of climate change in the Arctic. *Quaternary Science Reviews* 29, 1716–1727.

Wilhelm, B., Arnaud, F., Sabatier, P., Magand, O., Chapron, E., Courp, T., Tachikawa, K., Fanget, B., Malet, E., Pignol, C., Bard, E., Delannoy, J.J., 2013. Palaeoflood activity and climate change over the last 1400 years recorded by lake sediments in the north-west European Alps. *Journal of Quaternary Science* 28, 189–199.

Winsor, K., Carlson, A.E., Caffee, M.W., Rood, D.H., 2015. Rapid last-deglacial thinning and retreat of the marine-terminating southwestern Greenland ice sheet. *Earth and Planetary Science Letters* 426, 1–12.

Wittmeier, H.E., Bakke, J., Vasskog, K., Trachsel, M., 2015. Reconstructing Holocene glacier activity at Langfjordjøkelen, Arctic Norway, using multi-proxy fingerprinting of distal glacier-fed lake sediments. *Quaternary Science Reviews* 114, 78–99.

Wolfe, A. P., Miller, G. H., Olsen, C. A., Forman, S. L., Doran, P. T., 2004. Geochronology of high latitude lake sediments. In: Pienitz, R., Douglas, M. S. V., Smol, J. P. (eds.): Long-Term Environmental Change in Arctic and Antarctic Lakes. Kluwer Academic Publishers, Dordrecht, Netherlands, 19–52.

Wolfe, B.B., Edwards, T.W.D., Jiang, H., MacDonald, G.M., Gervais, B.R., Snyder, J.A., 2003. Effect of varying oceanicity on early- to mid-Holocene palaeohydrology, Kola Peninsula, Russia: Isotopic evidence from treeline lakes. *Holocene* 13, 153–160.

Woo, M., 2012. Permafrost Hydrology. Springer, Dordrecht, 572 p.

Wyatt Oswald, W., Anderson, P.M., Brown, T. a., Brubaker, L.B., Hu, F.S., Lozhkin, A. V., Tinner, W., Kaltenrieder, P., 2005. Effects of sample mass and macrofossil type on radiocarbon dating of arctic and boreal lake sediments. *The Holocene* 15, 758–767.

Xu, H., Liu, B., Wu, F., 2010. Spatial and temporal variations of Rb/Sr ratios of the bulk surface sediments in Lake Qinghai. *Geochemical Transactions* 11, 3.

Zachos, J., Pagani, M., Sloan, L., Thomas, E., Billups, K., 2001. Trends, rhythms, and aberrations in global climate 65 Ma to present. *Science* 292, 686–93.

Zwoliński, Z., Mazurek, M., Paluszkiewicz, R., Rachlewicz, G., 2008. The matter fluxes in the geoecosystem of small tundra lakes, Petuniabukta coast, Billefjorden, Central Spitsbergen. *Zeitschrift Fur Geomorphologie* 52, 79–101.

IX. Appendix

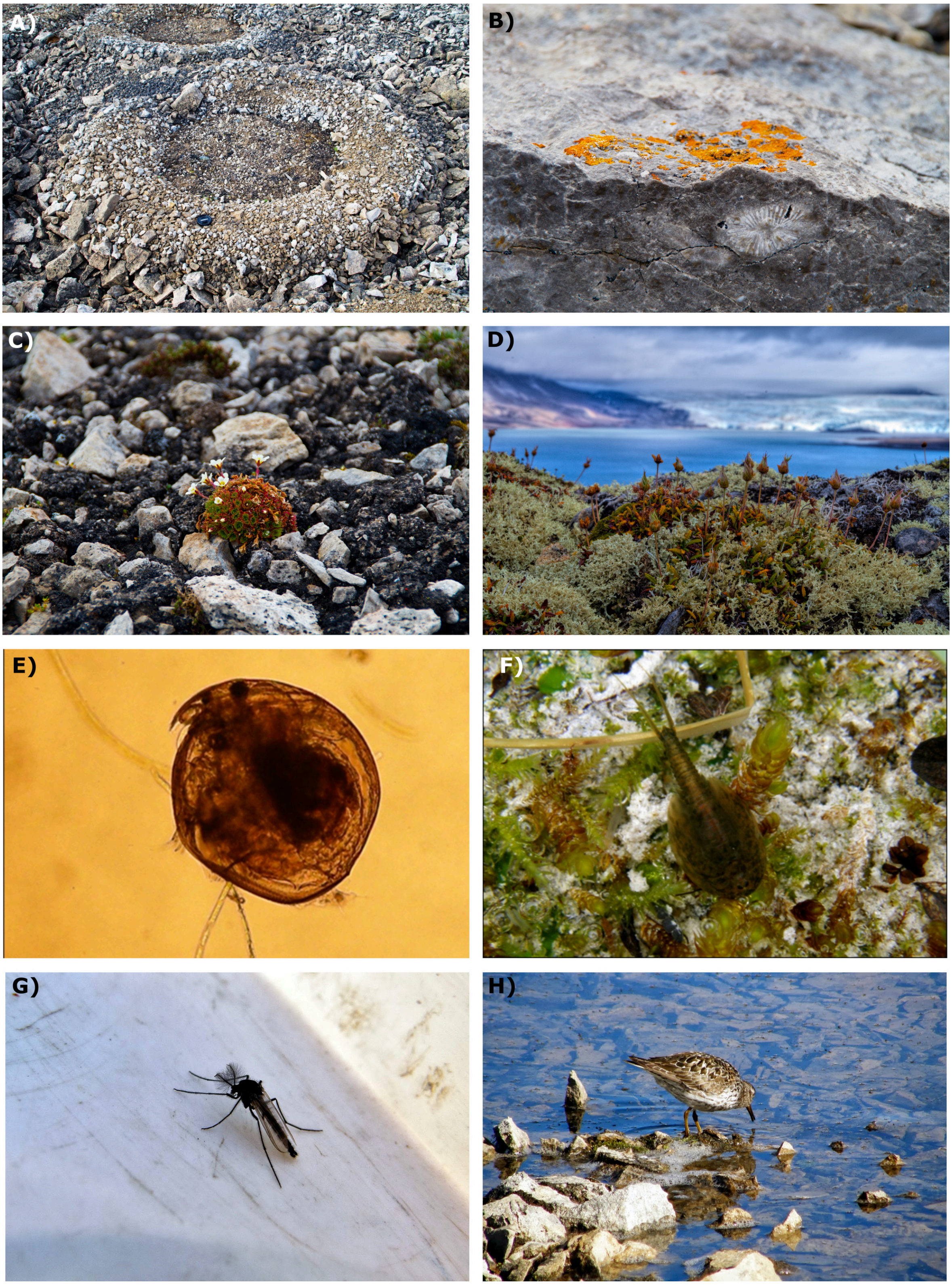

Figure 9.1 Geoforms, flora and fauna in Garmaksla lake and catchment. A) Well-developed sorted circle of ~1 m diameter. B) Carboniferous calcareous sandstone with a fossilised rugose coral and covered with a lichen of genus *Xanthoria* or *Calopaca*. C) *Saxifraga cespitosa* growing in regolith. D) Vascular plants growing among lichen *Usnea*. E) Cladocera species *Chydorus sphaericus*. F) *Lepidurus arcticus* ('tadpole shrimp'). G) Adult chironomid (Diptera). G) Wading *Calidris maritima* (purple sandpiper). Photos A–D taken by the author, the remainder (E–H) kindly provided by Dan Vondrák.

Figure 9.2 Coring Garmaksla sediments using Kajak gravity corer and rubber boat (A); cutting the profile in 1cm steps (B); bottom of the lake (top of the core) with green algae and plant macroremains (C); the upper part of core G13/1 with distinct lamination (D). Coring and subsampling was performed analogously in northeastern Norway. Photos A, B, D taken by the author, C by Dan Vondrák.

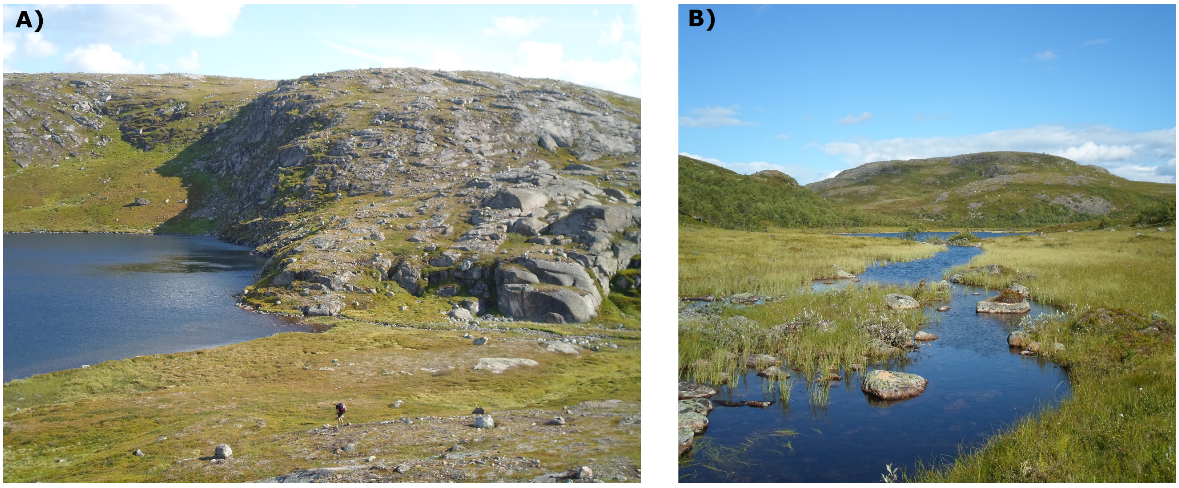

Figure 9.3 Typical tundra landscape of Jarfjorden area beyond the Arctic treeline. A) Oligotrophic lake Forste Hogfjellvatn is impounded by a topographic step in glacially scoured bedrock, covered with sparse glacial drift. B) Stream with rich littoral vegetation flowing into the lake; dwarf birch cover in the background.

Table 9.1 Correlation matrix of geochemical data together with accumulation rate, χ and diatom productivity from Garmaksla core **G13/1**. Correlations significant at the 0.05 level are denoted by one asterisks, correlations significant at the 0.01 level by two asterisks in **bold**. Negative correlations are presented in *italics*.

Acc. rate (mm/yr)	TOC [%]	TIC [%]	TS [%]	Al	Si	Ca	Fe	Al/Si	Zr/Rb	Si/Zr	Diatom productivity	
,102	***-,534*****	**,577****	***-,397*****	***-,412*****	***-,496*****	,023	-,200	,042	***-,309*****	,112	***-,606*****	MS (χ)
	-,354**	**,341****	-,218	-,025	-,199	,025	-,111	,173	***-,310*****	,150	***-,366*****	Acc Rate
		-,933**	**,808****	**,477****	**,494****	-,140	,244*	,035	**,379****	-,102	**,575****	TOC [%]
			-,711**	***-,522*****	***-,489*****	,203	-,209	-,079	***-,389*****	,089	***-,595*****	TIC [%]
				,378**	,145	***-,331*****	,016	,242*	,296*	-,067	**,409****	TS [%]
					,484**	-,082	,252*	**,559****	**,427****	-,218	**,568****	Al
						,568**	**,738****	***-,410*****	**,358****	-,001	**,560****	Si
							,800**	**-,573****	,066	-,013	,032	Ca
								-,425**	**,313****	-,111	**,418****	Fe
									,120	-,270*	,083	Al/Si
										-,244*	**,617****	Zr/Rb
											-,298*	Si/Zr

Table 9.2 Correlation matrix of geochemical and granulometric data from **G13/2.**

TOC [%]	TIC [%]	TS [%]	TC [%]	MGS (µm)	Clay (%)	Silt (%)	Sand (%)	Sorting	Skewness	Kurtosis	
-,410**	,308*	***-,392*****	***-,459*****	-,159	-,028	,146	-,118	-,291*	-,040	,319*	MS (χ)
	-,940**	**,810****	**,951****	**,548****	***-,439*****	***-,486*****	**,492****	,017	**,445****	***-,456*****	TOC [%]
		-,703**	***-,788*****	***-,648*****	**,573****	**,590****	**-,605****	,035	***-,544*****	**,610****	TIC [%]
			,822**	**,369****	-,132	-,289*	,268*	,162	,170	***-,351*****	TS [%]
				,375**	-,250	-,318*	,314*	,064	,287*	-,246	TC [%]
					-,861**	***-,963*****	**,973****	-,254*	**,647****	***-,705*****	MGS (µm)
						,806**	***-,868*****	**,541****	***-,668*****	**,491****	Clay (%)
							-,994**	,130	***-,710*****	**,689****	Silt (%)
								-,213	**,724****	***-,672*****	Sand (%)
									,085	-,157	Sorting
										-,571**	Skewness

Table 9.3 Correlation matrix of geochemical data plus χ of core **G13/3**. Note that XRF data were measured for only 40–45 samples out of total 70, resulting in relatively fewer significant correlations.

TOC [%]	TIC [%]	TS [%]	Al	Si	S	Ca	Fe	Al/Si	Zr/Rb	Si/Zr	
-,405**	**,436****	***-,334*****	***-,458*****	-,252	-,152	,260	-,261	-,370*	-,156	,111	MS (χ)
	-,917**	**,564****	-,027	-,157	,031	***-,344****	-,004	,312*	-,072	-,072	TOC [%]
		-,568**	-,167	-,096	,098	**,451****	-,017	-,147	-,151	,043	TIC [%]
			,011	,020	,159	-,159	,293	-,050	,017	,001	TS [%]
				,874**	-,118	-,099	,364*	,079	**,661****	-,226	Al
					-,175	-,028	,262	***-,399*****	**,749****	-,236	Si
						,351*	**,414****	,145	-,010	***-,430*****	S
							,591**	-,148	,125	***-,486*****	Ca
								,142	,333*	***-,552*****	Fe
									-,332*	,082	Al/Si
										-,555**	Zr/Rb

Table 9.4 Correlation matrix of geochemical and granulometric data from **KH2**.

MGS (µm)	Clay (%)	Silt (%)	Sand (%)	Al	Si	K	Ca	Mn	Fe	Rb	Sr	Zr	Al/Si	Ca/Si	Fe/Mn	Rb/Sr	
-,027	-,102	-,057	,082	,064	***-,428*****	-,257*	-,269*	**,692****	**,549****	,233*	***-,369*****	-,179	**,647****	**,306****	,002	,201	MS (χ)
	-,275*	***-,807*****	**,838****	-,115	-,056	-,092	-,068	-,029	-,068	-,013	-,045	,015	-,076	-,042	,039	,057	MGS (µm)
		,064	***-,339*****	**,340****	,261*	,128	,224*	-,056	**,416****	,076	**,320****	,066	,260*	,004	-,052	***-,629*****	Clay (%)
			-,960**	-,088	-,029	-,019	-,037	-,130	-,072	-,085	-,041	-,125	-,068	,000	,157	,020	Silt (%)
				-,012	-,046	-,018	-,027	,138	-,048	,061	-,050	,099	-,008	-,001	-,133	,157	Sand (%)
					,736**	**,663****	**,686****	**,312****	**,336****	**,639****	**,629****	**,645****	,236*	-,183	-,157	-,266*	Al
						,716**	**,787****	-,017	-,238*	**,522****	**,819****	**,740****	***-,435*****	***-,475*****	-,211	-,207	Si
							,900**	,008	-,173	**,445****	**,644****	**,704****	-,206	,132	-,239*	-,127	K
								,023	-,133	**,537****	**,741****	**,750****	-,230*	,134	-,219	-,163	Ca
									,306**	**,576****	,056	**,288****	**,310****	,033	-,268*	**,316****	Mn
										,175	-,169	-,192	**,910****	,251*	,203	***-,462*****	Fe
											,684**	**,783****	,103	-,064	***-,298*****	,179	Rb
												,827**	***-,332*****	-,219	-,069	***-,314*****	Sr
													-,276*	-,114	-,246*	-,010	Zr
														,434**	,142	-,271*	Al/Si
															,039	-,013	Ca/Si
																-,368**	Fe/Mn

Table 9.5 Correlation matrix of geochemical and granulometric data from **KL1**.

MGS (µm)	Clay (%)	Silt (%)	Sand (%)	Al	Si	Ca	Mn	Fe	K	Rb	Sr	Zr	Al/Si	Ca/Si	Fe/Mn	Rb/Sr	
-,093	**,437****	-,103	,022	**,731****	**,362****	,269*	**,784****	**,528****	**,400****	**,521****	,144	,138	**,518****	-,082	***-,334*****	,268*	MS (χ)
	-,383**	***-,965*****	**,979****	-,056	-,039	-,048	-,114	-,082	-,053	-,074	-,083	-,062	-,058	-,023	,051	-,005	MGS (µm)
		,232*	**-,392****	,102	-,289*	***-,347*****	**,511****	**,756****	-,261*	-,256*	-,251*	***-,394*****	**,680****	,046	-,159	***-,390*****	Clay (%)
			-,986**	-,067	-,004	,026	-,055	-,044	,005	-,031	,058	,050	-,066	,038	,044	-,045	Silt (%)
				,046	,054	,036	-,036	-,089	,041	,071	-,011	,021	-,055	-,044	-,014	,110	Sand (%)
					,759**	**,535****	**,518****	,270*	**,529****	**,547****	**,333****	**,442****	**,305****	-,248*	-,190	,273*	Al
						,662**	,197	***-,308*****	**,649****	**,677****	**,492****	**,694****	***-,361*****	***-,490*****	-,196	**,532****	Si
							,006	-,298*	**,871****	**,733****	**,825****	**,798****	-,250*	,282*	,023	,299*	Ca
								,607**	,062	**,356****	,033	,014	**,509****	-,141	***-,403*****	,047	Mn
									-,289*	-,288*	-,278*	***-,413*****	**,918****	,130	-,070	***-,531*****	Fe
										,766**	**,672****	**,669****	-,218	,128	-,107	**,478****	K
											,762**	**,783****	-,240*	-,056	-,309*	**,735****	Rb
												,883**	-,250*	,292*	-,022	,213	Sr
													-,394**	,004	-,057	**,395****	Zr
														,288*	-,005	***-,462*****	Al/Si
															,287*	***-,392*****	Ca/Si
																-,331**	Fe/Mn

Table 9.4 Correlation matrix of geochemical and granulometric data from **KH2** (top right) and **KL1** (bottom left).

	MS (χ)	MGS	Clay (%)	Silt (%)	Sand (%)	Al	Si	K	Ca	Mn	Fe	Rb	Sr	Zr	Al/Si	Ca/Si	Fe/Mn	Rb/Sr	**KH2**
MS (χ)		-,093	**,437****	-,103	,022	**,731****	**,362****	**,400****	,269*	**,784****	**,528****	**,521****	,144	,138	**,518****	-,082	***-,334*****	,268*	MS (χ)
MGS (μm)	**,373****		***-,383*****	***-,965*****	**,979****	-,056	-,039	-,053	-,048	-,114	-,082	-,074	-,083	-,062	-,058	-,023	,051	-,005	MGS (μm)
Clay (%)	**,469****	-,265*		,232*	**-,392****	,102	-,289*	-,261*	***-,347*****	**,511****	**,756****	-,256*	-,251*	***-,394*****	**,680****	,046	-,159	***-,390*****	Clay (%)
Silt (%)	-,214	-,254*	-,232*		**-,986****	-,067	-,004	,005	,026	-,055	-,044	-,031	,058	,050	-,066	,038	,044	-,045	Silt (%)
Sand (%)	**,308****	**,780****	-,101	***-,789*****		,046	,054	,041	,036	-,036	-,089	,071	-,011	,021	-,055	-,044	-,014	,110	Sand (%)
Al	,064	-,064	,186	***-,378*****	,181		**,759****	**,529****	**,535****	**,518****	,270*	**,547****	**,333****	**,442****	**,305****	-,248*	-,190	,273*	Al
Si	***-,428*****	-,242*	-,269*	-,128	-,041	**,736****		**,649****	**,662****	,197	***-,308*****	**,677****	**,492****	**,694****	***-,361*****	***-,490*****	-,196	**,532****	Si
K	-,257*	,038	-,263*	-,243*	,189	**,663****	**,716****		**,871****	,062	-,289*	**,766****	**,672****	**,669****	-,218	,128	-,107	**,478****	K
Ca	-,269*	-,087	-,207	-,207	,076	**,686****	**,787****	**,900****		,006	-,298*	**,733****	**,825****	**,798****	-,250*	,282*	,023	,299*	Ca
Mn	***,692*****	,377**	,167	***-,367*****	,439**	**,312****	-,017	,008	,023		**,607****	**,356****	,033	,014	**,509****	-,141	***-,403*****	,047	Mn
Fe	***,549*****	-,162	**,865****	-,254*	-,012	**,336****	-,238*	-,173	-,133	**,306****		-,288*	-,278*	***-,413*****	**,918****	,130	-,070	***-,531*****	Fe
Rb	,233*	,134	-,017	-,253*	,223	**,639****	**,522****	**,445****	**,537****	**,576****	,175		**,762****	**,783****	-,240*	-,056	-,309*	**,735****	Rb
Sr	***-,369*****	***-,353*****	-,248*	-,084	-,137	**,629****	**,819****	**,644****	**,741****	,056	-,169	**,684****		**,883****	-,250*	,292*	-,022	,213	Sr
Zr	-,179	,060	***-,305*****	-,245*	,213	**,645****	**,740****	**,704****	**,750****	**,288****	-,192	**,783****	**,827****		***-,394*****	,004	-,057	**,395****	Zr
Al/Si	**,647****	,061	**,791****	-,301**	,153	,236*	***-,435*****	-,206	-,230*	**,310****	**,910****	,103	***-,332*****	-,276*		,288*	-,005	***-,462*****	Al/Si
Ca/Si	**,306****	,182	,178	-,139	,160	-,183	***-,475*****	,132	,134	,033	,251*	-,064	-,219	-,114	**,434****		,287*	***-,392*****	Ca/Si
Fe/Mn	,002	-,218	,088	,374**	-,365**	-,157	-,211	-,239*	-,219	-,268*	,203	***-,298*****	-,069	-,246*	,142	,039		***-,331*****	Fe/Mn
Rb/Sr	,201	**,701****	***-,379*****	,010	**,437****	-,266*	-,207	-,127	-,163	**,316****	***-,462*****	,179	***-,314*****	-,010	-,271*	-,013	***-,368*****		Rb/Sr
KL1	MS (χ)	MGS	Clay (%)	Silt (%)	Sand (%)	Al	Si	K	Ca	Mn	Fe	Rb	Sr	Zr	Al/Si	Ca/Si	Fe/Mn	Rb/Sr	

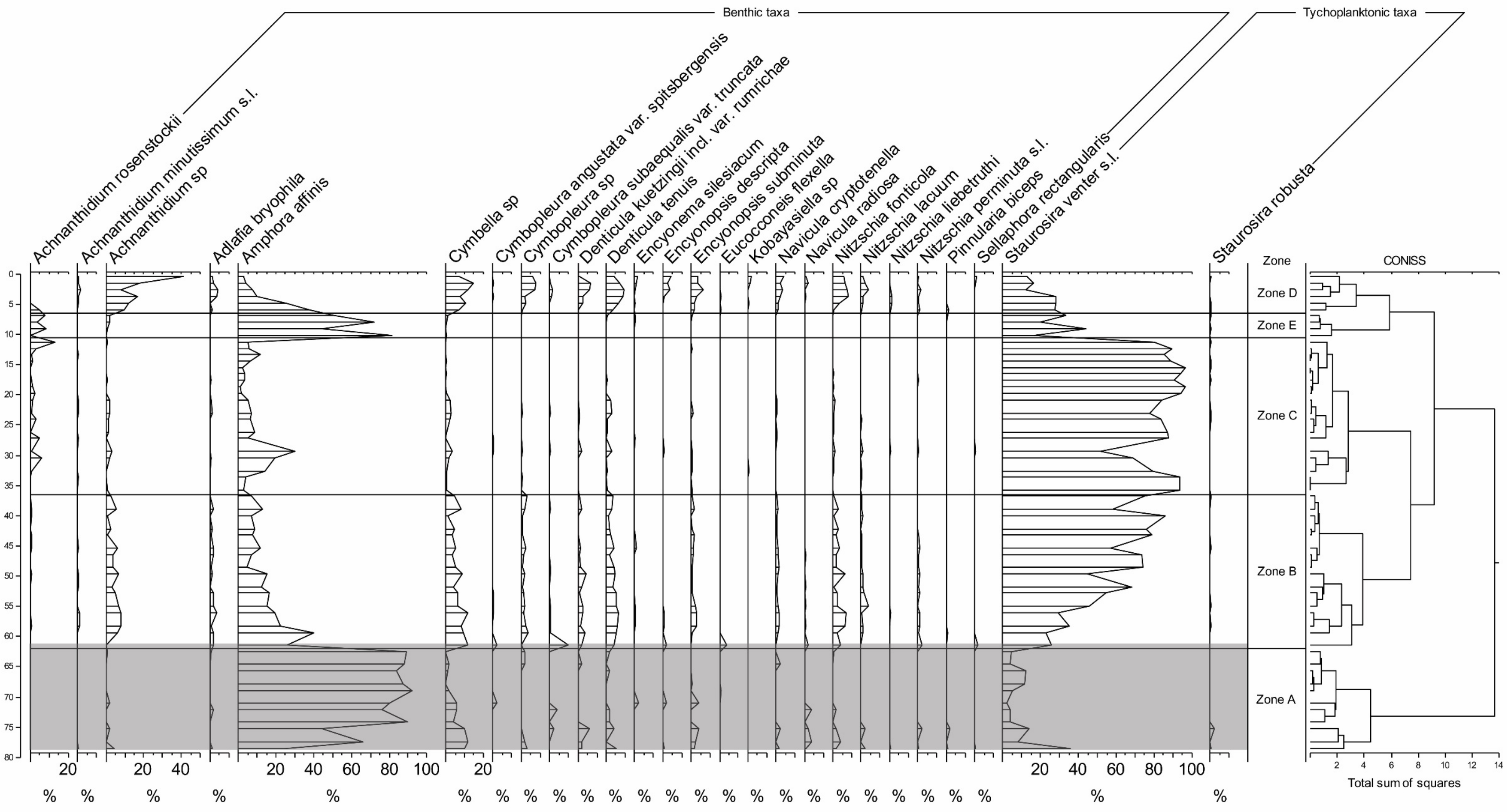

Figure 9.4 Stratigraphy of diatom assemblages in Garmaksla core G13/1. Analysis and design Pinseel (2014).

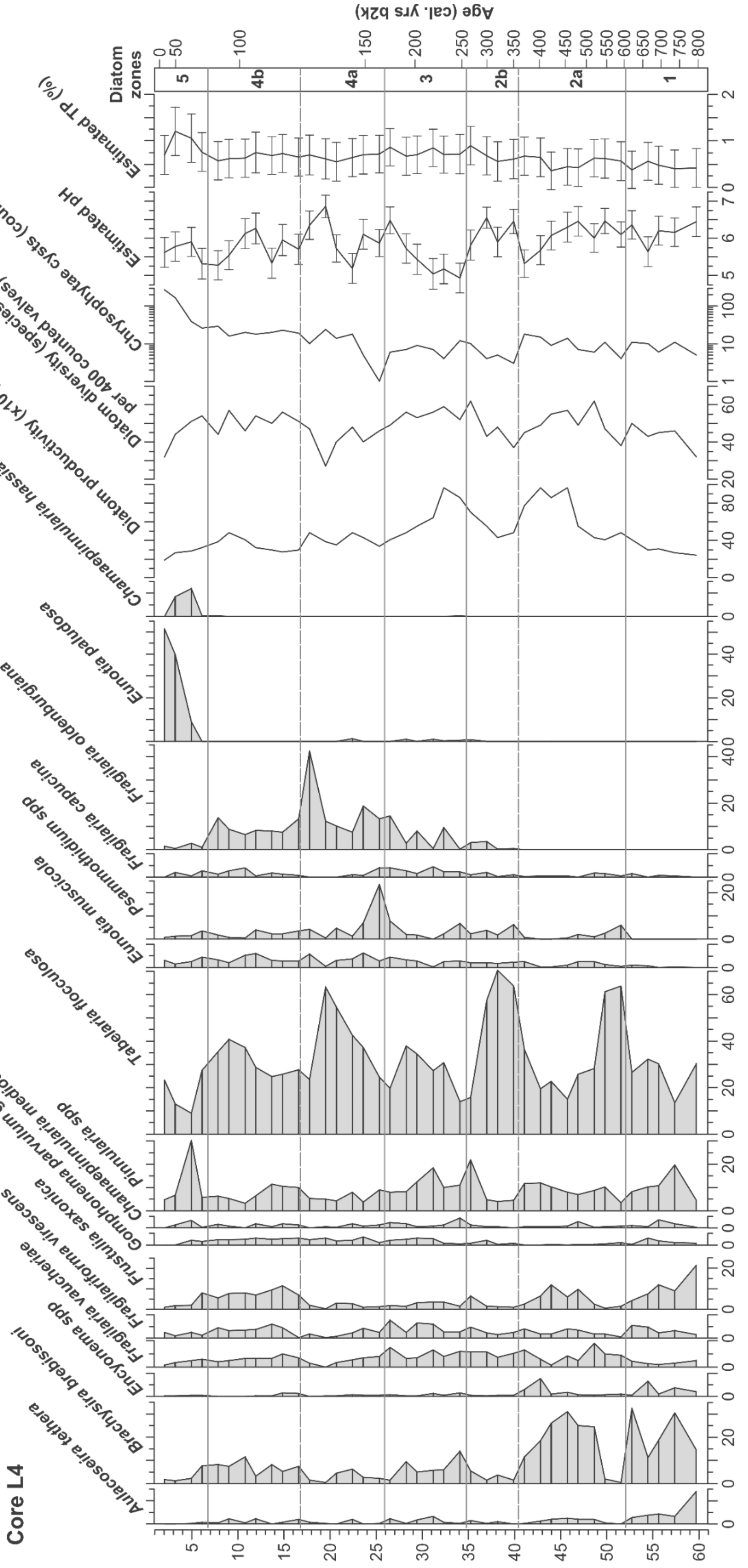

Figure 9.5 Stratigraphic diagram of diatom assemblages in Kobbefjord core L4. The most abundant taxa mentioned in the text are displayed. Diatom analysis performed by Bára Chattová, the chart design by the author.